Analysis of the ions and electrons emitted by hypoxanthine in the gas phase upon irradiation : from the isolated molecule to hydrated clusters

Chiara Nicolafrancesco

Normandie Université

UNIVERSITÉ CAEN NORMANDIE

THÈSE

Pour obtenir le diplôme de doctorat

Spécialité **CHIMIE**

Préparée au sein de l'**Université de Caen Normandie**

Analysis of the ions and electrons emitted by hypoxanthine in the gas phase upon irradiation: from the isolated molecule to hydrated clusters

Présentée et soutenue par

CHIARA NICOLAFRANCESCO

Thèse soutenue le 29/09/2022

devant le jury composé de :

MME EMILY LAMOUR	Professeur des universités - UNIVERSITE PARIS 4 PARIS-SORBONNE	Rapporteur du jury
M. NICOLAS NIEUWJAER	Maître de conférences HDR - UNIVERSITE PARIS 4 PARIS-SORBONNE	Rapporteur du jury
MME SÉVERINE BOYE-PERONNE	Professeur des universités - Université Paris-Saclay	Membre du jury
MME ISABELLE MONNET	Directeur de recherche - CEA	Membre du jury
M. LUCAS SCHWOB	Docteur - Deutsches Elektronen-Synchrotron (DESY)	Membre du jury
M. XAVIER FLECHARD	Directeur de recherche - Université de Caen Normandie	Président du jury

Thèse dirigée par **JEAN-YVES CHESNEL** (Centre de recherche sur les ions, les matériaux et la photonique (Caen))

ED 591 PSIME

CIMAP

ACKNOWLEDGEMENTS

The present thesis work started on November 5, 2018 and was defended on September 29, 2022.

During a first period from November 2018 to mid-January 2022, this work was performed under the supervision of Patrick Rousseau (CIMAP, Caen, France) and Aleksandar Milosavljević (Synchrotron SOLEIL, Saint-Aubin, France). Their role was to supervise the instrumental development and the experiments presently reported, the analysis and interpretation of the data, and the writing of papers in international journals with refereeing process. At the end of this first period, from July 2021 to November 2021, Philippe Boduch (CIMAP, Caen) devoted significant efforts to facilitate the supervision of this thesis, although he was not involved in this work.

Then, during the last period, from mid-January 2022 to September 2022, Jean-Yves Chesnel (CIMAP, Caen) took the full responsibility of the supervision of this PhD work, without having been involved in the present instrumental development and experiments, nor in the data analysis and interpretation. His role was focused on the supervision of the writing of this thesis and the preparation of its defense. Although he was also not involved in the acquisition and interpretation of these data, Lucas Schwob (DESY, Hamburg, Germany) provided valuable suggestions and comments on the initial drafts of this dissertation. Aleksandar Milosavljević checked the subchapter dedicated to the results obtained using X-ray photoelectron spectrometry, thus answering a pending question.

This work was co-financed by the Normandy Region (50%) and by the SOLEIL Synchrotron (50%).

Now, the next lines are devoted to personal thanks:

First, I would like to thank Lucas and Jean-Yves for having accepted reading and revising this manuscript, their amazing keen eye, patience, and skill in giving it a decent form. Thank you, sincerely.

I would also like to thank the members of the committee, for accepting reading this work. Thank you to Mme Lamour and M Nieuwjaer for accepting being the thesis protractors, to Mme Boyé-Péronne, Mme Monnet, and M Fléchard for accepting being members of the jury.

A great thank you also goes to the CIMAP laboratory, I feel too embarrassed to thank each one of you, but I'll try naming a few of you. Amine, Isabelle, and Jimmy, of the two laboratory-direction that I have met, thank you for your listening and advice. To the AMA group, and, again, to Jean-Yves. Thank you to Pierre and his little family, Philippe, Violaine, François, Jean-Marc, Claire, Mathieu, Hermann, Alain, Thierry, Clara, Brigitte and her crutches, Julie, Éric, Stephan, Benoit, Yvette, Cédric, Quentin, and Hervé.

Thank you to the PhD students with whom I had the honour of sharing this experience the most: Suvasthika, Marwa, and Nicolas, thank you, we really nailed the real sense of life: having good food from different parts of the world. Thank you to Prudence and her determination, and for showing that having a baby and finishing a PhD is not impossible. Thank you to Cesare and Francesca for making me feel less homesick and for the polenta, mostly for the polenta.

Thank you to the unionists from SUD éducation, especially to Bruno, and his lovely family.

A heartfelt thank you to Marie and Vincent from the Doctoral School, and to Melissa from the CoMUE.

Thank you to the healthcare team that followed me during these years, it might seem silly, but they had a very important role in this. Dr. Leclerc, Dr. Guillouet, Sebastien, all the interns, nurses, midwives at the Pole Femme-Enfant-Hématologie (especially the ones I met at the UGO and SIG) du CHU, Dr. Vardon and Dr. Dreyfuss. Actually, I should be thanking the French national healthcare system in general. And in this healthcare mess, how could I not thank Luisa?

Thank you to the family I was born into and the one I have built here. Thank you to Jean-Christophe, you why, don't make it embarrassing.

Finally, I need to thank Domitilla, without whom I would not have made it: it is thanks to you if these pages are here.

TABLE OF CONTENTS

1 INTRODUCTION

As the English band Motörhead said in their song "Line in the Sand", "Evolution is a mystery", the process by which the differentiation of the life forms could happen has been for a long time one of the most intriguing enigmas eluding scientists for centuries. Some educated guesses were made by Gregor Mendel while trying to explain how the pea's Mendelian traits could be passed on to subsequent generations through invisible "factors" contained inside the organism's cells. What Mendel called "factors", later were identified to be the genes contained in the DNA double helix.

With this small introduction, we will see that understanding the actors of the conservation and transmission of the genetic information has required the efforts of several researchers from very different fields, from medicine to physics; of whom only a few are cited here.

Although DNA was discovered as early as 1869 thanks to the Swiss medical doctor Johannes Friedrich Miescher, the fact that such an inert substance could contain the building blocks for developing living beings was considered inacceptable, thus many believed that its only function was to store phosphorus for energetic purposes. The first experiments that began to disprove this idea arrived in 1944 thanks to the efforts performed by Oswald Avery, Colin MacLeod, and Maclyn McCarty, three geneticists from the Rockefeller Institute for Medical Research. They were able to demonstrate that it was actually the strands of DNA that caused the genetic transformation in bacteria[1]. Further evidence was brought in 1952 by the experiment carried out by Martha Chase and Alfred Hershey when

[1] Bacterial transformation is one of the three ways by which bacteria can transmit their genetic material horizontally, namely by not reproducing itself. In this case, the bacterium uptakes genetic material directly from its surroundings. The other two methods are the conjugation, in which the information is given through a plasmid from a donor to a recipient in cell-to-cell contact; and transduction, where a virus (phage) moves DNA from a bacterium to another one.

they observed that DNA was the genetic material transmitted by the enterobacteria phage T2 to infect and reproduce itself in *E. coli* cells.

The apex of this understanding came during the fifties, thanks to the work of several scientists. Rosalind Franklin and her student Raymond Gosling produced X-ray diffraction images of hydrated DNA. Their images, especially the famous image 51, led to the discovery of the double helix structure of the DNA molecule, with two antiparallel strands linked via hydrogen bounds between one purine (adenine or cytosine, respectively) and one pyrimidine (thymine or guanine, respectively). Namely, adenine binds thymine with two hydrogen bonds, and cytosine binds guanine with three hydrogen bonds. What was not discovered yet is that, along with these four canonical bases, there are also some non-canonical bases, which can be formed upon the damage of the nitrogenous bases with various effects on the molecular stability and the ability to carry information. Hypoxanthine is one of the non-canonical bases.

Similarly to the others purines, hypoxanthine plays multiple roles, both at a cellular and at a systemic level, ranging from mRNA component to a neurotransmitter. In fact, one fascinating aspect of life as a biological process is its ability to use the same molecules, structures, and even whole organs in a multitude of ways to adapt itself to the environment in which it exists. This, with a hint of anthropocentrism, could be defined as Nature's imagination and creativity.

In this perspective, trying to unveil some of the hypoxanthine properties appears as an interesting way of adding one small piece more to the mosaic of knowledge acquired regarding the ability of biomolecules to interact with each other and with their environment.

During the course of this doctoral project, aiming at unravelling some aspects of hypoxanthine's intrinsic structure and stability, I joined two research groups in France. The first one is the AMA ("Atoms, Molecules, et Agregats", or "atoms, molecules, and clusters") team, from the CIMAP laboratory ("Centre de recherche sur les Ions, les MAtériaux et la

Photonique", or "centre for the research on the ions, materials and photonics"). This research team is focussed on studying diluted matter, at different aggregation states from isolated molecules to mixed clusters, by probing them essentially with ions but also with photons. The second team is the one of the PLEIADES beamline (short for "Polarized Light source for Electron and Ion Analysis from Diluted Excited Species") of the SOLEIL synchrotron, which studies condensed and diluted matter from isolated molecules to clusters, in particular by probing them by means of soft X-ray photons. In both groups, I had the opportunity to study hypoxanthine in molecular environments of increasing complexity, thus providing with a bottom-up picture of the changes in the physical and chemical properties of this molecule as a function of the number of hydrogen bonds in which it is involved.

In addition to this short introduction, this manuscript is composed of five chapters. The next one, called "object of study and motivations", provides a description of the context in which this work takes place. It also describes what the present work proposes to study. The chapter entitled "scientific context", describes the state of the art concerning the purine derivatives, most notably hypoxanthine. It further describes the principles behind the experimental techniques employed during this doctoral project. Then, the chapter called "experimental methods" is dedicated to the description of the setups employed in order to perform the experiments, whose results are presented in the subsequent chapter 5 entitled "results and discussion". The last chapter, "conclusions and perspectives", provides a review of what has been observed in the previous chapters, providing a more complete vision of this PhD work, while also discussing some ideas to further develop it.

2 OBJECT OF THE STUDY AND MOTIVATION

The characterisation of biomolecules is essential for the better understanding of the different and complex properties that define them and in particular, their biological activity. On the one hand, shedding light on the molecule itself, i.e. when isolated in the gas phase, can provide a precise knowledge of its intrinsic chemical and physical properties. On the other hand, when searching for how biomolecules interact with their environment, the study of the isolated/pure molecule is not sufficient[1]. Indeed, in nature, a solvent, usually water, embeds the biomolecules, forming hydrogen bonds with them and thus modifying their properties[2,3]. Moreover, in a living cell, biomolecules interact with each other; thus modifying each other characteristics upon their interaction via the so-called weak bonds (hydrogen bonds, van der Waals interactions).

To illustrate these extensive interactions and their consequences, it is enough to consider the way the human serum albumin modifies its shape in order to accommodate the load of bioactive molecules, such as thyroid and sexual hormones, to transport them in the blood stream[4,5] (Figure 1). This is why, when investigating the properties of a given biomolecule in the gas phase, the negligence of the molecular environment surrounding the object of investigation may lead to results that do not necessarily explain what happens in reality, i.e. when that object is in interaction with an environment.

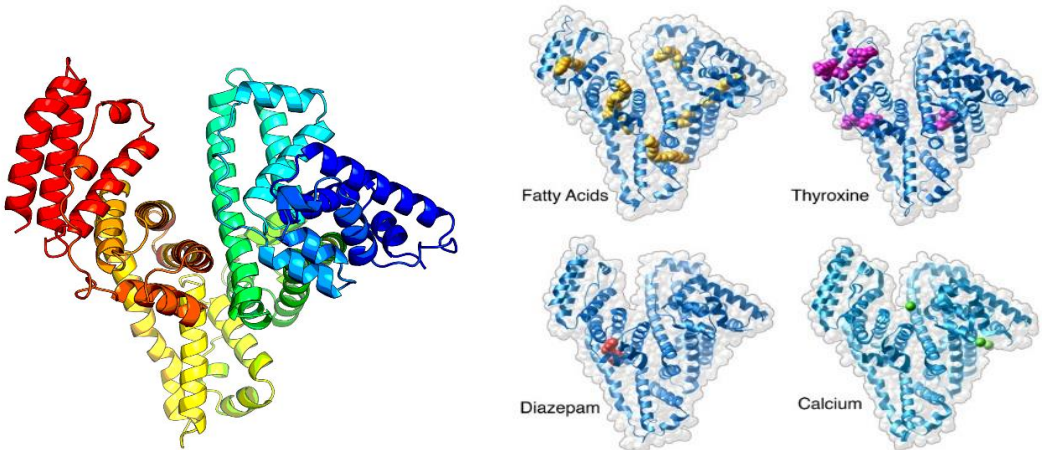

FIGURE 1: HUMAN SERUM ALBUMIN. ON THE LEFT WITHOUT ANY LIGAND. ON THE RIGHT THE DIFFERENT BINDING SITES, ACCORDING TO THE MOLECULAR CLASS BEING LOADED. (SOURCES: LEFT, RESEARCHGATE; RIGHT, PDB101 DATA BASE)

In order to obtain a study system presenting both the cited characteristics – a solvated environment and a cluster-like group of molecules, in which the molecules can form non-covalent bonds – there are two principal and most reliable methods. The two methods consist primarily of soft ionisation techniques (such as electrospray ionisation sources[6]) for bigger molecules, and ovens connected to a hydration system for the smaller ones[7]. By controlling the molecular environment, it is possible to perform the investigation in a highly simplified representation of *in vivo* conditions, still presenting the basic characteristics of the biological milieu.

In this context, there have been numerous studies concerning the characterisation of various categories of biomolecules in the gas phase. For example, numerous studies have been dedicated to the characterisation of small molecules such as uracil[8], adenine and glycine[9], just to cite small molecules.

In this work, we are considering the molecule of hypoxanthine (Figure 2) as our model for a biomolecule. Hypoxanthine is a purine derivative, along with many other well-known molecules, from adenine and guanine, to caffeine and theobromine. This molecule plays various roles in several

biological pathways[4]. Compared to adenine, it is characterised by the presence of only one substituent in position six (see Figure 2). Since it is one of the lesser-studied purine derivative, and given its versatility, it is important to perform a systematic bottom-up study of this molecule's characteristics. Specifically, on a structural side, the intent of this work is to understand if its fragmentation pattern somehow resembles the one of the DNA and RNA-forming purines, if it can form hydrogen-bound pure clusters, and eventually to get an insight on which atoms are involved into their formation, if these clusters can be solvated, and how. Considering the molecular chemistry, the aim is to understand how an increasing complexity of the molecular environment affects each atom forming the hypoxanthine molecule.

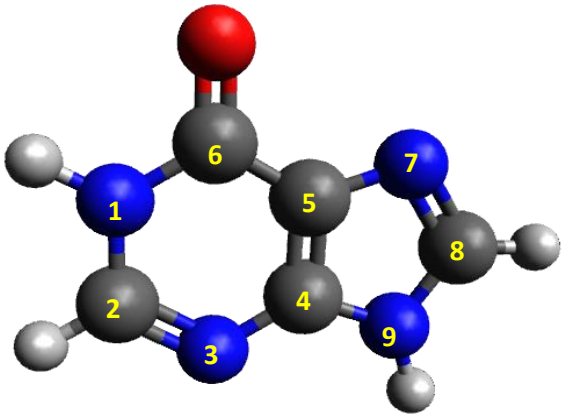

FIGURE 2: THE HYPOXANTHINE MOLECULE, A PURINE DERIVATIVE.

Nevertheless, why and how investigating the properties of these molecules? As said before, studying a molecule in a representation of its usual environment can give a more realistic image of what happens in a living organism, especially when considering the effects of radiation damage on a cell, since the presence of molecular environments could mitigate the effects of it[1]. In fact, cells are continuously exposed to ionising radiations from natural causes (for example the photo damage due to solar exposition)[10] or need to be exposed to them for therapeutic reasons (for example ionising radiation-based therapy for cancer treatment)[11].

Regarding the means by which obtaining this kind of information, it starts to appear clear that employing just one technique would not give a satisfactory answer. There is the need of analysing the situation from different points of view, in order to obtain a complete picture of the processes that take place. In fact, from one side, we need to understand if the weak bonds formed between interacting biomolecules and with a water solvent can stabilise the whole system upon irradiation. To retrieve this kind of information, the most suited technique (and the one employed in this work) is based on mass spectrometry. First, this technique allows for obtaining information about the biomolecule stability by analysing eventual ion- or photon-induced fragmentation, as well as the formation of eventual clusters, pure and hydrated. The method of having an increasing complexity of the studied sample helps better understanding and pinpointing how each modification of the molecular environment can actually change the characteristics of the molecule under investigation. Second, when coupled with activation methods such as ion impact or photon absorption, mass spectrometry can be used to analyse fragmentation patterns, providing us with information regarding different interactions processes, such as the electron capture or atom knockout phenomena with ions, or resonant excitation and ionization with photons. On the other hand, if we want to obtain information about the chemical state of the molecule, how the solvation and the presence of other molecules linked via hydrogen bonds affects it, we need to investigate the state of the core electrons forming it. To do so, a most appropriate technique is X-ray photoelectron spectrometry. By the interpretation of the variation in the spectral features, we can observe how the environment affects the chemical properties of our sample.

By employing these techniques, we expect to be able to obtain a quite complete picture of the events surrounding the effects of the environment on a biomolecule upon the interaction of ionising radiation, from both a molecular stability point of view, and from a chemical alteration one.

3 SCIENTIFIC CONTEXT

3.1 BIOMOLECULES

With the term biomolecule, we generally intend any carbon-based molecule with an active role in the cellular metabolism. Broadly speaking, they are divided into four categories: polysaccharides, proteins, lipids, and nucleic acids. Each of them is composed of subgroups with extremely various roles. For example, some polysaccharides behave as an energy provider for the metabolic cellular reactions, such as sucrose; others have a structural function, such as cellulose. Most of these complex molecules can be dissected into simpler building blocks, or monomers, with the lipids presenting the highest structural variety, and often not presenting monomers. In particular, the nucleic acids represent the category of biomolecules that are in the interest of this study. The structure of a nucleic acid is composed of nitrogenous bases (purines and pyrimidines), which are linked via a glycosidic bond to a pentose sugar, deoxyribose for DNA, ribose for RNA; thus forming a nucleoside. The sugar is bound in position 5' to a phosphate group to form a nucleotide (Figure 3). The addition of a second phosphate group produces a nucleoside diphosphate, while the addition of a third one leads to a nucleoside triphosphate, such as ATP (which is the triphosphate form of adenosine). In particular, this study focusses on the examination of the nitrogenous base composing the nucleotide. The nitrogenous base considered here is the purine derivative called hypoxanthine.

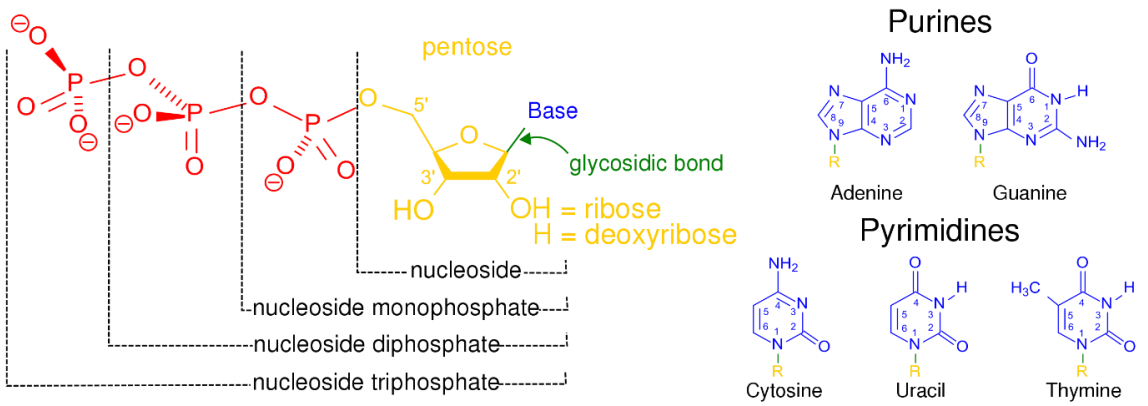

FIGURE 3: THE STRUCTURE OF NUCLEOSIDES. IN RED THE PHOSPHATE GROUPS, IN YELLOW THE PENTOSE SUGAR (EITHER RIBOSE OF DEOXYRIBOSE), WITH THE CANONICAL NITROGENOUS BASES SHOWN IN BLUE.

3.1.1 PURINE DERIVATIVES

Structurally, purines share a basic structure of a pyrimidine ring conjugated to an imidazole ring in position 4 and 5 (Figure 4). The presence of multiple double bonds, with the subsequent possibilities of multiple resonance forms, provides the molecule with a certain thermal stability (for example hypoxanthine has thermal decomposition peak at 412 °C, adenine at 355 °C, and guanine at 512 °C[12]). There can be a variety of substituents in different positions on both rings, giving the final molecules different properties, and a variable number of tautomeric forms[13].

Even though purine itself does not occur in nature, purine derivatives play key and diverse roles in several biological pathways. They are the nitrogenous component of DNA and the different forms of RNA, thus being fundamental for the genetic information preservation, transcription, and transmission. In the form of nucleoside triphosphates (Figure 3), their production is the aim of cellular respiration, lactic and alcoholic fermentation, and photosynthesis; they are widely considered in the exchange currency of the biological processes[4]. Moreover, nucleosides can be neurotransmitters: adenosine is as an antagonist of dopamine and glutamate receptor, thus having an inhibitory effect on the Central Neuro-System[14]. In addition, being the by-product of adenosine triphosphate (ATP) hydrolysis, high adenosine concentrations in the basal forebrain promotes sleepiness[15].

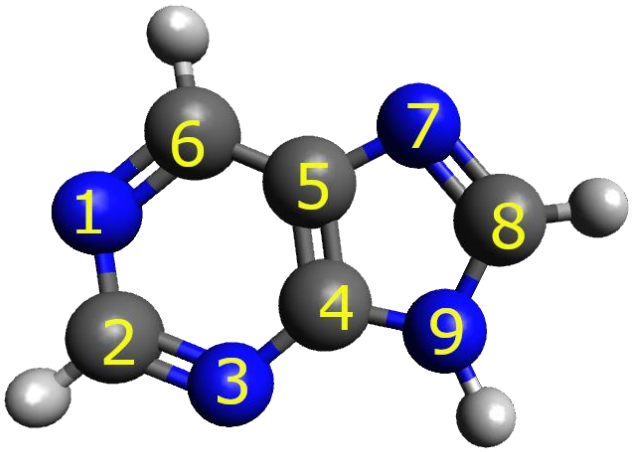

FIGURE 4 : SCHEMATIC REPRESENTATION OF THE PURINE MOLECULE.

3.1.2 HYPOXANTHINE

In this context, where the understanding of the fate of DNA and RNA forming purines is the object of such an intense study, the hypoxanthine molecule appears as an interesting object of investigation. Hypoxanthine, while not being a canonical DNA and RNA forming base, can be found in both acids for different reasons. When found in DNA, it is the product of adenine deamination, and given its similarity to guanine, it can pair with cytosine[16] (Figure 5). This produces a wobble DNA pair that needs to be

repaired[16]. On the other hand, hypoxanthine ability of binding both cytosine and thymine/uracil is useful in the context of mRNA translation with tRNA carrying the correspondent amino acid. There, it is quite frequently found in the last position (called 5'), where it can bind with either cytosine or uracil and give the signal to produce the same amino acid[17].

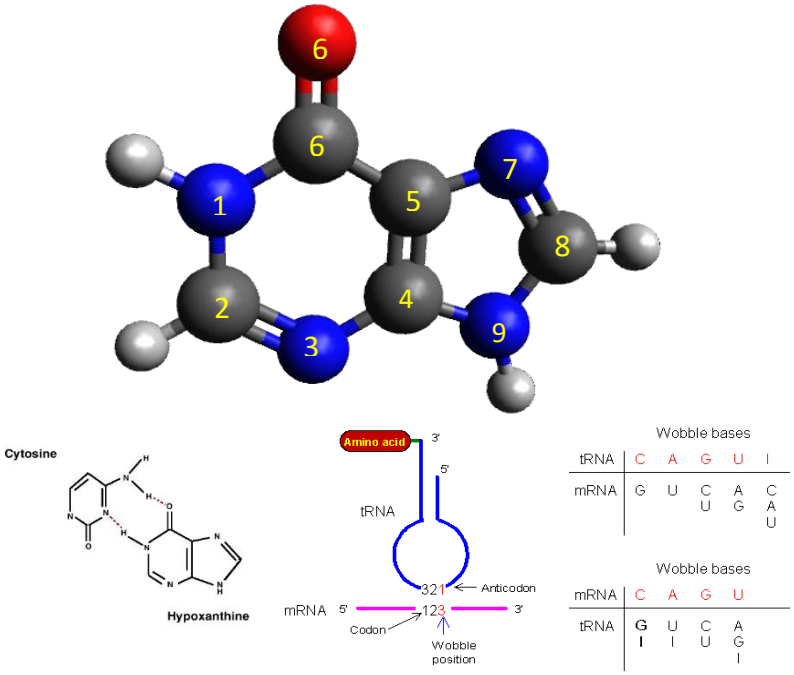

FIGURE 5: TOP: SCHEMATIC REPRESENTATION OF HYPOXANTHINE, WITH THE NUMERATION OF ITS COMPONENT ATOMS. BOTTOM LEFT: THE WOBBLE DNA PAIR OF HYPOXANTHINE AND CYTOSINE. BOTTOM RIGHT: INOSINE (HYPOXANTHINE) WOBBLY PAIRS IN TRNA.

Structurally, hypoxanthine is a purine derivative, much like adenine and guanine, with the preferred IUPAC name being 1,9-Dihydro-6H-purin-6-one[18], with a formula of $C_5H_4N_4O$, and a molar mass of 136.1115 g/mol. As seen from the name, it presents one substituent in position 6, which is an oxygen atom. In this aspect, it is similar to guanine, which additionally presents an amine group in position 2. Similarly to adenine, it presents only one substituent in the same position. It is also worth noticing that hypoxanthine is the product of the catabolism of both adenine and guanine[5]. Therefore, it could be argued that hypoxanthine can present characteristics common to both molecules. Given its characteristics, with

the presence of only one substituent in the sixth position, as in adenine, and the fact that this substituent is an oxygen atom, as in guanine, the hypoxanthine molecule presents characteristics hybrid to both adenine and guanine. Moreover, hypoxanthine plays some important roles itself in the form of inosine (its nucleoside form): for example, it is the endogenic ligand of the $GABA_a$ receptor, binding in the benzodiazepine site[19]. Moreover, its presence is linked to both neural cord repair[20] and after-stroke healing[21]. Thus, it can be a useful indicator of both hypertensions and hypoxia.

3.1.3 WHAT HAS BEEN STUDIED ALREADY

Given the various and essential roles played by purine derivatives, they have been extensively studied in a variety of scientific fields ranging from neurosciences, metabolic studies, biochemistry, to molecular physics investigations. In particular, studying this molecular category in a bottom-up approach in the gas phase through spectrometric and spectroscopic techniques allows investigating intrinsic properties while increasing the molecular environment complexity in a controlled manner. In the next subparagraphs, we will consider what has been observed in previous experiments concerning purines, focusing on adenine, guanine, and, especially, hypoxanthine. More specifically, understanding what happens to these molecules upon the interaction with photons or highly charged ions in an increasingly more complex environment, could give us access to the events that might occur when biological matter is exposed to ionising radiations[22].

3.1.3.1 PREVIOUS STUDIES ON ADENINE AND GUANINE

As previously mentioned, nucleobases have been the object of intense spectrometric and spectroscopic studies under various molecular environmental conditions, both experimentally and theoretically[9,23,24]. One of the most thoroughly studied purines is adenine. In this subsection, we will consider some of the previous experiments that aimed at characterising this molecule.

In fact, there have been several studies on adenine fragmentation and adenine cluster formation conducted using projectiles such as photons and a variety of ions in different energy ranges. Some of these studies include the ones conducted by Domaracka et al.[9] and Schlathölter et al.[24] for the ion-induced experiments, while the works by Jochims et al.[22] is an example of studies conducted by photon irradiation. These articles were generally in accordance regarding the molecular stability and the main dissociation channels. The dominant peaks in mass-over-charge ratio (m/z) spectra are represented by the intact ionised molecule at m/z= 135 (where m refers to the number of nucleons and z refers to the ionization degree), the loss of HCN at m/z= 108, the $HCNH^+$ fragment at m/z = 28, and in some cases the presence of the doubly ionized adenine at m/z= 67.5[9,22,24]. Moreover, Domaracka et al. observed an increase in the molecular stability guaranteed by the hydrogen bonding in adenine dimers[9]. While analysing the clusters formation it was observed that the spectra showed a monotone decrease of the peak intensities with increasing clusters size[24].

Compared to the amount of data available for adenine, as literature reports, the investigation on guanine has been considered particularly complex due to its low solubility, its tendency to pyrolysis when vaporised, and the large number of tautomers this molecule can present[10,25]. Though, some studies on the molecular fragmentation of protonated guanine could be conducted, thanks to Collision-Induced Dissociation (CID) and the use of an electrospray ionization source, showing that also in this case the loss of the HCN group takes place[23].

Beside from obtaining information on the molecular fragmentation pathways, synchrotron radiation can provide useful insight on the chemical-oxidative state of the atoms composing the molecule. As seen from the work of Plekan *et al.*[26], isolated adenine in the gas phase has been the subject of studies by both X-ray Photoelectron Spectroscopy (XPS) and Near-Edge X-ray Absorption Fine Structure (NEXAFS) investigation[26]. Here, it was observed that in the C 1s photoemission spectrum, two peaks

appeared. The one at the lowest binding energy (291.0 eV) was attributed to the C atom in position 5 (Figure 6), given the fact that it is the least substituted one, having just one N atom bound to it. The other peak at 292.5 eV, presenting the main contribution, was attributed to the sum of the other four C atoms, always bound to two N atoms[26]. While observing the N 1s spectrum, three peaks were observed. The first one was at 404.4 eV and was attributed to the atoms $N_{1,3,7}$ (see Figure 6), the second one was found at 405.7 eV, which resulted from the photoionization of N_6, while the last one corresponding to N_9 had a peak at 406.7 eV[26]. On the other hand, given guanine's above-mentioned characteristics, obtaining oven-produced gas-phase XPS spectra is indeed difficult for that molecule. However, some studies have been conducted in the solid phase. One example is the work by Furukawa et al[27]. Here, they obtained XPS data for the O 1s and N 1s signals. The O 1s signal consists in a single peak at 530.6 eV, while a more complex signal for the N 1s spectrum leads to three peaks: one at 398.4 eV, representing the imine –N=; one at 400.0 eV representing the amine -NH; and one at 401.1 eV for the dehydrogenated amine N_1 next to the C=O group[27]. As it can be seen, the difference in the binding energy between the N 1s signals from the gaseous adenine and the solid-state guanine is significant; this could be attributed partially to the aggregation state of the samples. In their published work, Furukawa et al.[27] also obtained XPS lines for adenine from a solid substrate, in which two peaks were identified: the imine one at 399.3 eV, and the amine one at 400.6 eV. One of the possible reasons for the difference could be attributed to different methods in energy calibration. If it is assumed that both calibrations are correct, the explanation would reside in the fact that the adenine lines collected for nitrogen by Plekan et al.[26] are representative for the gaseous isolated molecule, with no interactions reducing the binding energy; while the level of aggregation for the spectra by Furukawa et al.[27] is significantly higher, being a bulk powder set on a copper substrate.

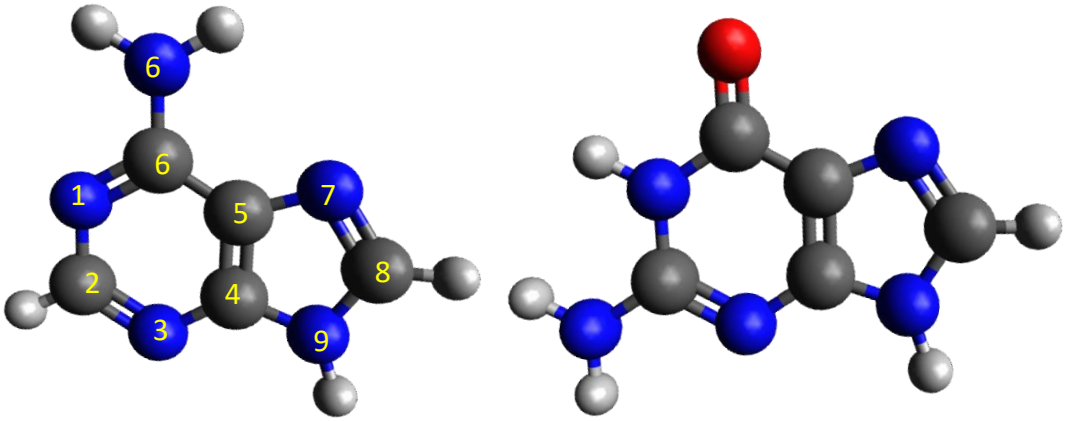

FIGURE 6: SCHEMATIC REPRESENTATION OF ADENINE, ON THE LEFT; AND OF GUANINE, ON THE RIGHT.

As illustrated from the results obtained for adenine, with both, heavy charged ions and photons, one obtains some signature fragments, which are an indication of the weakest bonds, as seen from the results obtained by Domaracka et al.[9], Schlathölter et al.[24] and Jochims et al.[22]. In particular, the bonds between the N_1 and C_2, and N_3 and C_4 or C_5 and N_7, and C_8 and N_9, can be considered the most favourable cleavage sites of the molecule, with processes sometimes involving a hydrogen transfer.

Since the general structure of adenine closely resembles the one of hypoxanthine, this could mean that also hypoxanthine presents these weak bonds as the favourable cleavage sites.

The experiment conducted by Barc et al.[28] showed that, when hydrated, the adenine molecule presents only the rise of a fragment at $m/z = 18$ (attributed to the NH_4^+ in position 6 group dissociation) and an increased intensity of the peak at $m/z = 136$, attributed either to the protonated adenine or the formation of hypoxanthine. They also observed that the hydration, namely the formation of adenine+$(H_2O)_n$ clusters had a stabilising effect on the adenine molecule. While we did not perform any experiment involving the isolated hydrated hypoxanthine, the fact that hydrogen bonds could stabilise the isolated molecule, thus reducing its fragmentation, could be an appreciable effect even on the fragmentation pattern of hydrated hypoxanthine clusters.

Observing the coincidence islands of adenine from the work of Alvarado et al.[29] and Moretto-Capelle et al.[30], we could determine which fragments are complementary and result from a same fragmentation pathway, thus giving a more complete picture regarding the process adenine undergoes after being ionised. Moreover, the theoretical study performed on adenine by Sadr-Arani et al.[23] showed that there is a similarity in the fragmentation patterns of adenine and hypoxanthine, which could be confirmed by the present study.

3.1.3.2 PRE-EXISTING STUDIES ON HYPOXANTHINE AND ITS DERIVATIVES

Given the fact that hypoxanthine presents characteristics similar to both DNA-forming purines, the study of the isolated hypoxanthine molecule in the gas phase is an ongoing research field. In particular, we will focus on what has been obtained already in the context of its cation stability upon interaction with either ions or photons, and its photoemission spectra (PES).

We will discuss briefly two previous studies performed by Dawley *et al.*[31] and by Feyer *et al.*[32]. In the first work, the photofragmentation spectrum was obtained at 70 eV[31]. On their side, Feyer *et al.* recorded multiple mass spectra at the energies corresponding to hypoxanthine valence levels[32]. The two studies presented some common features, as for example the parent ion peak at m/z = 136, the fragment ion after the loss of HCNH at m/z = 108 (or the fragment $C_4H_4N_4^+$), the complementary fragment $HCNH^+$ at m/z = 28, and the fragments at m/z = 54 and 53 representing $C_2H_2N_2^+$ (or the fragment C_2NO^+) and $C_2HN_2^+$, respectively[31,32].

When considering the photoemission spectra of the molecule, we can take into account the work performed by Feyer *et al.*[32] for PES data, and the one by Plekan *et al.*[33] for XPS data. The results of these works will be discussed more deeply in the results section of this work (see Chapter 5).

3.1.4 AIM OF THE PRESENT WORK

As we have seen, hypoxanthine can be a useful tool to investigate guanine-similar properties in an oven-induced gas phase, while remaining a vastly versatile and interesting molecule on its own, found in different environments. For these reasons, obtaining further information regarding how this molecule behaves in gradually more complex environments, namely in pure clusters and in hydrated ones, could be extremely helpful into better understanding and having a more complete view on the effects of radiation damage in both the cell nucleus and the whole cell itself. In this context, we aim at answering the following pending questions:

-what happens when hypoxanthine clusters are irradiated with heavy charged ions or photons?

-Is there some difference between the pure cluster fragmentation and the one of the hydrated one, both when using photons and ions?

-Does the hydration improve the cluster growth rate?

-Can different levels of hydration affect the growth of the clusters?

As were previously employed for unravelling the properties of adenine, both isolated and in clusters, the work of this thesis relied on mass spectrometric and spectroscopic techniques, in combination with photons and ions. These techniques are described in the following section.

3.2 MASS SPECTROMETRY USING IONS AND PHOTONS

3.2.1 A LITTLE HISTORICAL BACKGROUND

From a historical point of view, we can recognise the forefather of mass spectrometry in Sir Joseph John Thompson, who, in 1913, for the first time channelled a stream of neon through electric and magnetic fields observing the deflection of the stream by placing a photographic plate at the end of it. He observed two patches on the photographic plate, and attributed them to two neon isotopes, ^{20}Ne and ^{22}Ne [34]. We owe the term

"mass spectrometry" to Francis William Aston, Thompson's student, who further developed this technique in 1920 and was able to determine the atomic mass of the two isotopes[34]. Up until the Second World War this technique was strictly associated to the determination of the atomic mass of isotopes; until the rise of the petro-chemical industry and the development of the different plastics, for which an accurate determination and separation of the petroleum components was necessary to produce specific products[34]. During the fifties and sixties, the applications of mass spectrometry further expanded to the determination of even more complex compounds, up to today, where this technique is the most employed in determining the precise chemical composition of unknown substances, employed even as fast kits used by the custom service in airports.

3.2.2 GENERAL CONSIDERATIONS ON THE EXPERIMENTAL METHODS

The principle of mass spectrometry works by ionising the target compound brought in a gaseous phase, which may subsequently fragment or be further activated to dissociate. By analysing the mass-over-charge ratio (m/z) of those products, the chemical composition and structure of an unknown compound can be identified. There are various techniques to produce a sample vapour, if it does not naturally occur as a gas. Some of those are ovens, for sufficiently stable and small molecules. They will be further discussed in the next chapter. The ionisation can be induced by different means, which influences the degree of the fragmentation of the compound. The collision between the ionising beam and the sample takes place in the interaction zone; after activation and fragmentation of the produced ions, the charged particles are separated into an analyser according to their mass-over-charge ratio or ion mobility and then detected. The obtained signals are transformed into interpretable informatics data. The schematic representation of the main components of a mass spectrometer are shown in Figure 7. In the next paragraphs, we will discuss more into detail the way two types of mass spectrometry work. Lastly, there exist other methods described as soft-ionisation techniques,

such as electrospray ionisation (ESI) or matrix-assisted laser desorption ionisation (MALDI), which allow to produce ionised species in the gas-phase and that are especially used for complex and delicate biomolecules.

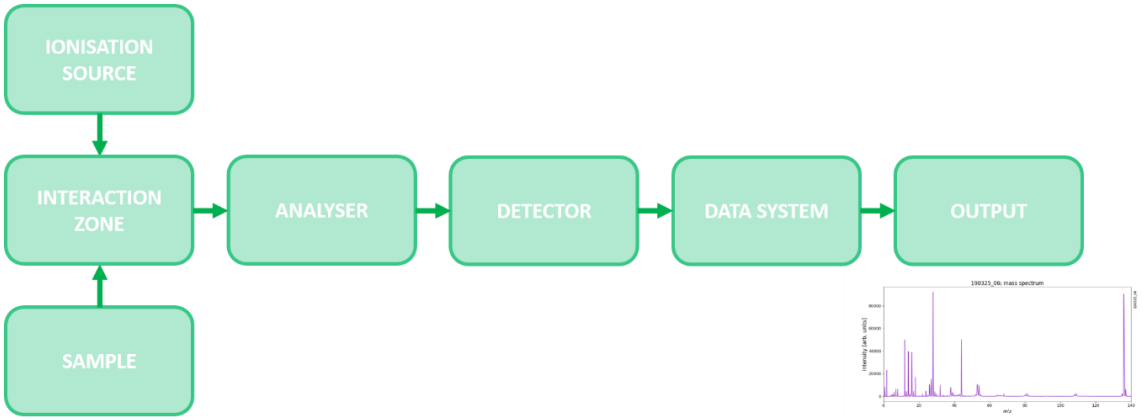

FIGURE 7: BLOC DIAGRAM REPRESENTATION OF A MASS SPECTROMETER.

3.2.3 MASS SPECTROMETRY WHEN USING IONS

3.2.3.1 ION-INDUCED DISSOCIATION

An important part of the experiments conducted in this work has been obtained thanks to the collision of hypoxanthine, into different aggregation states, with multiply charged ions. In the following, the principle of ion-induced dissociation is presented for the case of neutral gas-phase hypoxanthine (HYP) in collision with a multiply charged ion, A^{z+}, where z is the ionization degree[35]. Upon interaction, depending on the relative velocity between the projectile ion and the target electrons involved in the interaction, one of the following three processes can take place: excitation, electron capture, or ionisation. To determine which process is the most favourable one, a parameter, called K, has been introduced. K is expressed by the following formula and given by the ratio of the velocity of the projectile, v_A, compared to the one of the active target electron, v_e, multiplied by the ratio of the number Z_A of protons present in the projectile, divided by the number Z of protons present in the active target atom[36,37]:

$$K = \frac{Z_A}{Z} * \frac{v_e}{v_A}$$

The process of excitation can be either electronic or vibrational excitation. The first implies that, after the collision, the target molecule ends with one,

or more, electrons in an excited state, namely in one unoccupied molecular orbital, while the later involves an excited ro-vibrational state of the molecule. The excitation phenomenon can be described as follows:

$$A^{z+} + HYP \rightarrow A^{*z+} + HYP^{*}$$

Most molecules undergoing a collision will experience excitation, but this phenomenon is more pronounced in perturbative and intermediate state, when the K value is slightly smaller than one. This means that the velocity of the projectile is high and/or the collision is very asymmetric. This regime of collision may result in the fragmentation of the target molecule.

In the case of the electron capture, the velocity of the projectile is slower than the one of the electrons of the target molecule. In this case, the interaction between the target and the projectile is very marked in a quasi-molecular regime, where the K value is much bigger than one. In this case, there is the transfer of one or more electrons from the target molecule to the projectile ion (Figure 8):

$$A^{z+} + HYP \rightarrow A^{*(z-r)+} + HYP^{*r+}$$

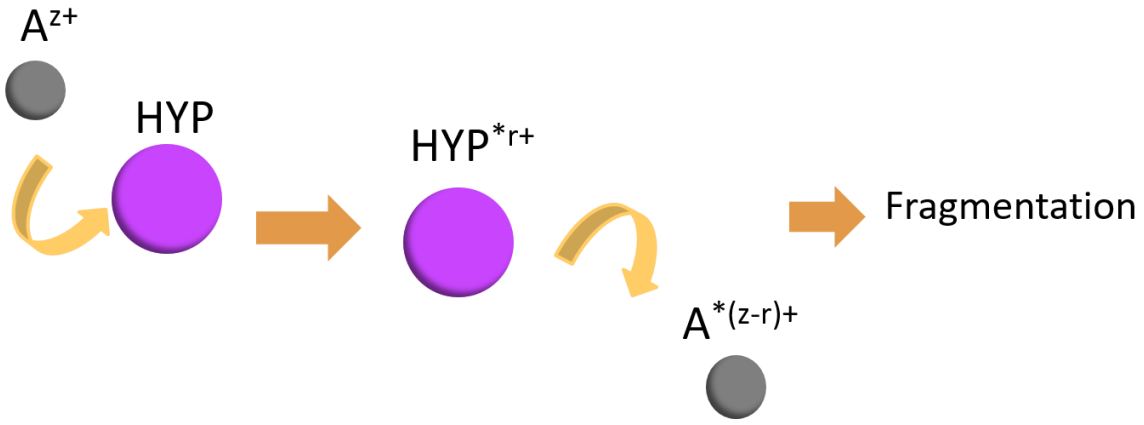

FIGURE 8: SCHEMATIC REPRESENTATION OF THE ELECTRON CAPTURE PROCESS.

The last process to be taken into account is ionisation. This process takes place when the value of K is significantly smaller than one, namely during perturbative processes. In this case, the target loses one or more electrons that are ejected in the continuum, as shown in the following formula:

$$A^{z+} + HYP \rightarrow A^{*z+} + HYP^{*s+} + se^{-}$$

In various cases, these processes can overlap, forming intermediate situations. For example, in a regime in which K is close to one, the electron capture, excitation and ionisation processes are combined.

The facility at which we performed experiments employing multiply charged ions, delivers low energy ions (< 20 keV/nucleon). Thus, the dominant process that is taking place is the electron capture. It has to be mentioned, nonetheless, that also the phenomena of ionisation and excitation take place, though less likely.

After the collision, the target molecule becomes charged and excited. In the time lapse of our detection, multiple outcomes are foreseeable. Either the molecule can stabilise itself and avoid dissociation by dissipating the internal energy in its vibrational and rotational modes, thus producing an intact ionised molecule; or the molecule undergoes fragmentation into neutral and/or charged fragments because of the excess of internal energy and/or because of the Coulombic repulsion between charges.

3.2.3.1.1 FRAGMENTATION

The fragmentation takes place when the molecule cannot stabilise itself after receiving a too high amount of energy and charge after the interaction with the ions. In this case, the molecule can dissipate the excess of energy (and/or charge) by fragmenting, i.e. by breaking some of its bonds. The effects can include the production of a various number of neutral and charged fragments with different kinetic energies. In the case of the production of charged fragments of the same sign, the Coulomb repulsion between them increases the kinetic energy received by each fragment.

In the case of the electron capture, the fragmentation takes place according to the following equation:

$$A^{z+} + HYP \rightarrow A^{*(z-r)+} + HYP^{*r+} \rightarrow A^{*(z-r)+} + HY^{*s+} + P^{*(r-s)+} + E_k$$

with $0 \leq s \leq r$. In the cases were $s = 0$ or $s = r$, we observe the production of what is referred to as neutral fragment “evaporation”.

The kinetic energy released in this kind of processes is not a single value, but rather a distribution (referred to as Kinetic Energy Release Distribution, KERd). Under certain experimental conditions, the KERd can

be measured, thus procuring information regarding the fragmentation dynamics and the excitation energy used to obtain this effect. However, the discussion of this topic is beyond the scope of the present work.
When the target molecule dissociates into one or multiple charged fragments, the study of its fragmentation can be performed by means of coincidence mass spectrometry.

3.2.3.1.2 COINCIDENCE MASS SPECTROMETRY

The study of the fragmentation of doubly-charged molecular ions is performed thanks to the coincidence mass spectrometry. With this technique, it is possible to collect simultaneously all the singly charged products obtained by the dissociation of a specific dication. This method helps also in the reconstruction of the dissociation mechanisms that gave rise to the charged fragments. The principle of the acquisition of a coincidence mass spectrum consists in the recording of two charged particles originating from the same molecule. Visually, the correlation between two fragments coming from the same molecule is represented by a coincidence island on the so-called coincidence map, relating the time-of-flight (TOF) of the two charged fragments (TOF1 and TOF2), putting the heaviest charged fragment in relation to the lightest charged one coming from the same molecule. The coincidence islands can provide information regarding the way the different fragmentation channels take place and, quite interestingly, the shape of each island gives information about the specific process involved in the production of the detected fragments, as it will be discussed further ahead.
However, there are some cases in which the identification of the obtained fragments is not unambiguous. In the case of hypoxanthine, for example, as we will see in the discussion of the obtained results (section 5.3.3), the identification of the fragments of $m/z = 28$ can be attributed to three atomic groups composing hypoxanthine, as it is highlighted in the Figure 9. As it can be seen, there are two equivalent potential fragments, namely the two HCHN groups in position 1-2 or 8-9; the other fragment that can

be recorded as m/z = 28 is the CO in position 6. Obviously, here, a limit in the interpretation of the coincidence maps is clear, since in many cases it is not possible to distinguish which of the three fragments is/are the one(s) contributing to the coincidence island. To solve this problem, theoretical calculations are needed.

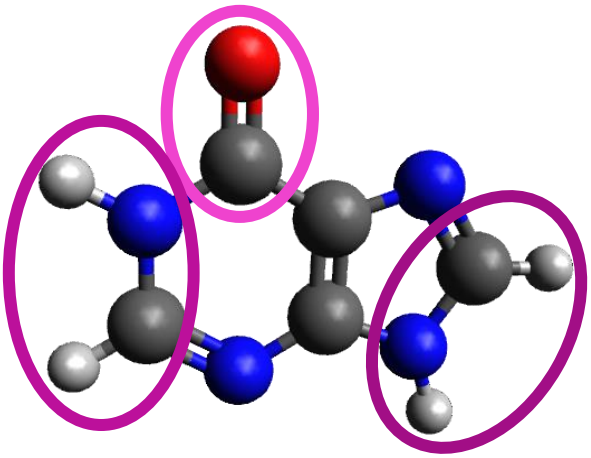

FIGURE 9: HYPOXANTHINE MODEL, WITH THE THREE M/Z = 28 FRAGMENTS SHOWN.

As previously mentioned, the shape of a coincidence island provides information regarding the fragmentation mechanisms underlying its own formation[38]. The average TOF of a fragment of mass m and charge q is proportional to $\sqrt{m/q}$, while the width Δt in TOF depends on the velocity v at which the fragment is emitted, as it is proportional to mv/q. Hence, considering the mass of the whole molecule (*HYP*) as m_{hyp}, presenting a charge q=$z.e$, dissociating into two charged fragments according to $HYP^{z+} \rightarrow H^{z_1+} + YP^{z_2+}$, with H of mass m_1, charge q_1=$z_1.e$, velocity v_1, and YP of mass $m_2 \geq m_1$, charge q_2=$z_2.e$, velocity v_2, with $m_{HYP} = m_1 + m_2$, the slope of the island can be determined by the following formula:

$$slope = -\frac{\Delta t_2}{\Delta t_1} = -\frac{m_2 v_2}{m_1 v_1} * \frac{q_1}{q_2}$$

where Δt_1 and Δt_2 are the width of the considered coincidence island along the TOF1 and TOF2 axes of the coincidence map, respectively. For the dication, the charge z is equal to +2. This means that z_1 and z_2 have both a charge of +1. Given the conservation of the momentum, the ratio of

m_2v_2/m_1v_1 is equal to one, too. This means that if the fragmentation produces only two singly charged fragments, the slope of the coincidence island has a value of -1 (Figure 10).

In other scenarios, the dissociation of the dication can produce two charged fragments and a neutral loss. The molecule can dissociate according to three different pathways, as shown below:

$HYP^{2+} \rightarrow HY^{2+} + P_3^0 \rightarrow H_1^+ + Y_2^+ + P_3^0$ (1)

$HYP^{2+} \rightarrow HP^+ + Y_2^+ \rightarrow H_1^+ + Y_2^+ + P_3^0$ (2)

$HYP^{2+} \rightarrow YP^+ + H_1^+ \rightarrow H_1^+ + Y_2^+ + P_3^0$ (3)

where the masses of the singly charged fragments H_1^+ and Y_2^+ appearing in the last step are m_1 and m_2, respectively, with $m_1 < m_2$.

According to the process of eq. (1), the evaporation of the neutral fragment happens in the first step of the process. Since the remaining dication HY^{2+} dissociates into two charged fragments, the slope is -1.

The determination of the slopes for the processes of eq. (2) and (3) is more complex, since the neutral loss takes place in the second and last step. In this case, the mass m_3 and the velocity v_3 of the neutral fragment has to be taken into account. In the case of the process of eq. (2), for which the mass (m_1) of the singly charged fragment formed in the last step is smaller than that of the other singly charged fragment (m_2), the island slope is:

$$slope = \frac{m_{HP}}{m_1}$$

On the other hand, in the case of the process of eq. (3), for which the mass (m_2) of the singly charged fragment formed in the last step is larger than that of the other singly charged fragment (m_1), the island slope is given by:

$$slope = \frac{m_2}{m_{YP}}$$

As it will be observed in one of the coincidence islands of the experimental results, sometimes the shape of the island can be circular. In this case the cause can be that multiple fragmentation processes give rise to the island, thus annulling the slope. Some other times, when multiple processes have the same fragments as a result, but one of them is predominant, the slope can be of an intermediate value.

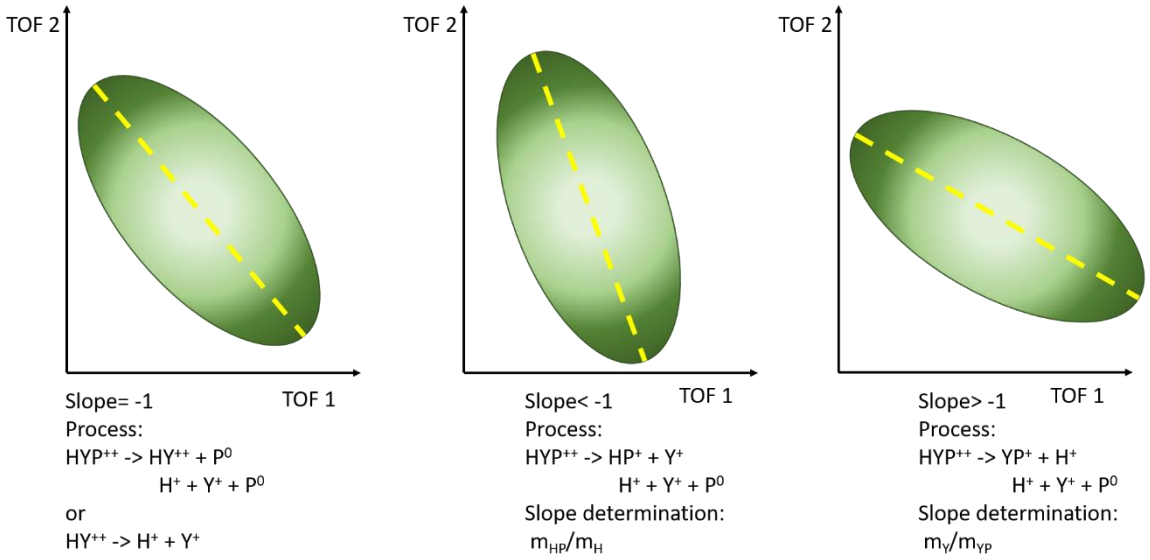

FIGURE 10: SCHEMATIC REPRESENTATION OF THE THREE MOST COMMON SHAPES OF THE COINCIDENCE ISLANDS, WITH THE CALCULATION OF THEIR SLOPES.

3.2.4 SPECTROMETRY METHODS WHEN USING PHOTONS

In the case of photoionisation, the "projectile" employed is an energetic photon, for example a Vacuum Ultra-Violet (VUV) or a soft X-ray photon. Depending of the photon energy range, upon photon absorption, the target molecule that has been ionised can also fragment[39,40]. The advantage of employing photons for performing mass spectrometry resides in the fact that the energy deposited on the target molecule can be controlled and measured with precision[40,41]. Different types of photon sources can be employed for different energy ranges. For example table-top lasers give access to energy in the infrared to ultraviolet range while a synchrotron radiation source, where the photon energy is selected using a monochromator, can typically provide light in the VUV to hard X-ray range[40].

3.2.4.1 VUV PHOTOIONISATION MASS SPECTROMETRY

The other activation method employed in combination to mass spectrometry in this work was the VUV photoionization. In this case, the probing projectile is a photon within the VUV range (6 – 120 eV).

With this technique, the photoionization can be direct or indirect, as shown below:

$$HYP + h\nu \rightarrow HYP^{*+} + e^{-}$$

or:

$$HYP + h\nu \rightarrow HYP^{*} \rightarrow HYP^{*+} + e^{-}$$

In the first process, the molecule is directly ionised, while in the second process, also referred to as auto-ionization, the electronically excited molecule decays by emitting an electron from its outer-shell[40]. Eventually, like in the case of the ion projectile, the ionized molecule may dissociate such that the charged products can be analysed by mass spectrometry.

In order to determine the internal energy of the molecular ion (E_{ion}) produced upon ionization with a photon in the VUV range at an energy $h\nu$ above the ionisation energy (IE), one has to consider the binding energy (E_B) and kinetic energy ($0 \leq E_{el} \leq h\nu\text{-}E_B$) of the electron ejected from the neutral molecule. This can be described as follows:

$$E_{ion} = h\nu - E_B - E_{el} + E_{thermal}$$

where $E_{thermal}$ is the thermal energy of the molecule before the ionisation process[40]. Hence, in so-called Photo-Ion Photoelectron Coincidence (PEPICO) experiments, it is possible to collect ions with an internal energy between 0 and $h\nu\text{-}E_B$, in coincidence with the energy selected electrons. To obtain this, it is possible to keep the photon energy fixed and scan the energy of the collected electrons, or to keep the kinetic energy of the electrons fixed and vary the photon energy. The use of a variable photon energy coupled to the collection of near zero electron energy has proven to be more advantageous, providing higher signal intensity, ion internal energy resolution, and minimisation of false coincidence.

It is important to point out that in this work; only the mass spectra at a fixed photon energy, above the ionisation edge, have been considered.

3.2.4.2 X-RAY PHOTOELECTRON SPECTROMETRY

The principle behind X-ray Photoelectron Spectroscopy (XPS) consists of shining X-ray photons on the sample, in order to eject an electron from the core level of the atoms. By analysing the number and yield of emitted electrons as well as their energy, it is possible to obtain information about the composition of the sample, its chemical state, molecular environment and electronic structure[40].

The photoemission spectroscopy, and XPS in this specific case, has the ability of providing information concerning the energy, momentum and spin number of a selected electron attached to a specific atom species forming a molecule[42]. This technique is based on the photoelectric effect, which can be approximatively described as follows, when considering that the electron is bound to an atom:

$$E_{el} = h\nu - E_B$$

in which, E_{el} is the kinetic energy of the selected electron, $h\nu$ is the photon energy, and E_B is the binding energy of that ejected electron (Figure 11). Since E_B is atomic species specific, this technique provides useful information regarding the sample chemical state[42].

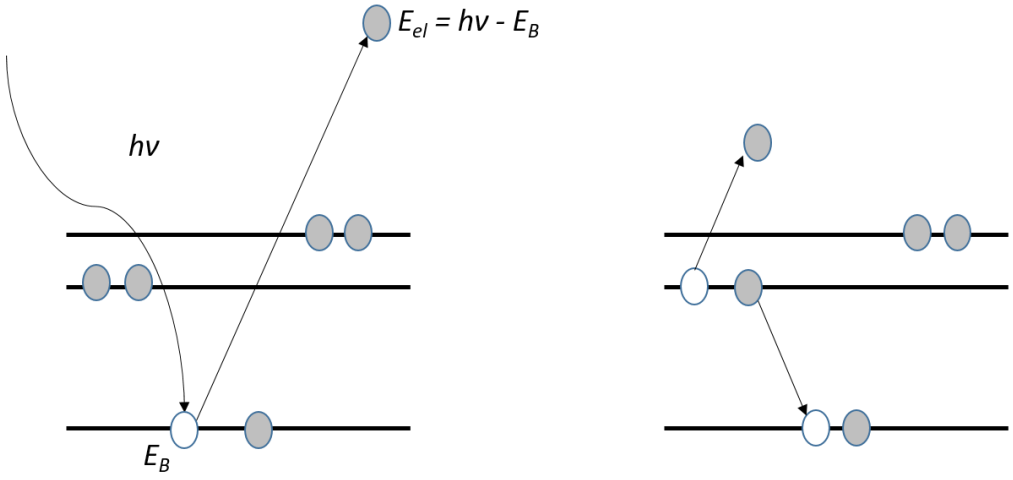

FIGURE 11: ON THE LEFT THE SCHEMATIC DESCRIPTION OF THE PHOTOELECTRON EMISSION. ON THE RIGHT THE SCHEMATIC REPRESENTATION OF THE AUGER ELECTRON DECAY.

Surrounding the phenomenon of the electron ejection, there are other satellite processes taking place which can prove themselves to be useful in the retrieval of information concerning the species considered, but they are beyond the scope of this work and they will be given just a rapid listing. Among them, there are the phenomena of *shake-up* and *shake-off*, due to the excitation of valence electrons; the multiplet splitting due to the presence of unpaired electrons in the core of the atom[42].

One phenomenon that will be briefly discussed in this work concerns the relaxation of the core-hole state. While observing the spectra for a given sample, there are additional lines aside from the photoemission ones, which do not change with the variation of the photon energy, but are specific to the sample taken into account. These lines result from the Auger electron decay (Figure 11). The process taking place in this phenomenon can be briefly described as follows. After the first electron is emitted from the core level, one from a higher energy orbital fills the vacant position, resulting in the emission of energy, which, in this case is transferred to another electron, which is further ejected into the continuum, thus resulting in the emission of an Auger electron.

An important characteristic to which the XPS spectra give access is the chemical shift. Even though the electrons directly involved in the formation of bonds are the valence ones, the core electrons are affected from these variations of the chemical environment, undergoing binding energy variations that are referred to as the chemical shift[42]. For example, when considering the carbon atom, its typical range of *K*-shell binding energy is from 285 to 300 eV: when it is bound to oxygen in forming CO_2, its binding energy is of 298 eV, while when it is involved in the methane molecule, CH_4, it is of 290.7 eV. The explanation resides in the fact that, when bound to elements presenting a higher electronegativity, the binding energy value increases, since the screening charge of the atom is decreased compared to its free form. When the atom is bound to less electronegative elements, there is more screening charge available and the binding energy decreases. As it will be seen in the results, the chemical shift provides important information regarding the electronic state of the studied system. Moreover, the chemical shift is often associated to the variation in the coordination number of a given atom considered in an aggregate. In particular, clusters and bulk materials composed of the same molecules present different chemical shifts due to the fact that the formed bonds are different: in the first case are mostly non-covalent interactions (hydrogen bonds and Van der Waals interactions), while in the second case are mostly covalent ones[42].

As mentioned before, the XPS method requires shining the sample with photons in the soft X- ray range. As these photons are absorbed in air, the experiments need to take place in an ultra-high vacuum chamber. The photon beam, which has to be monochromatic and with a high photon intensity, can be obtained from a synchrotron light source, possessing an X-ray range beamline. The gaseous sample, which is our case, can be injected in the analysing chamber thanks to a pressure gradient between the source chamber and the collision chamber. In the case of our experiment, the sample source is an oven, as it will be discussed in more details in the next chapter. Figure 12 gives a schematic block representation of the XPS setup.

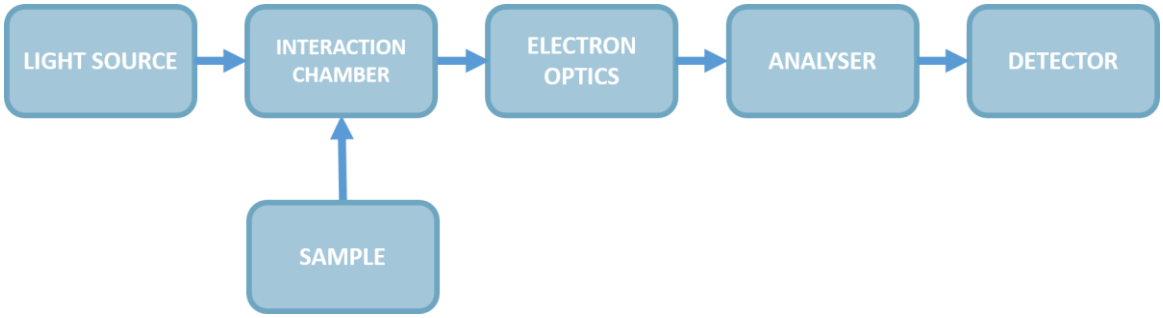

FIGURE 12: SCHEMATIC BLOCK REPRESENTATION OF THE GENERAL XPS APPARATUS.

There are three methods employed to record the kinetic energy of the ejected electrons. The first one consists of analysing the time taken by the electrons to pass through a known distance, similarly to an ion Time-of-Flight spectrometer, which will be discussed in detail in the next chapter. The second one is the retarding-field analyser. Only the electrons that have a kinetic energy sufficiently high to overcome the retarding field can reach the detector. Thus, one is able to select electrons of different energies by adjusting the potential of the grids forming the retarding field. This method makes it relatively difficult to obtain information regarding the low energy electrons and there is the risk of detecting pollution coming from the grids. The last method is the one in which the emitted electrons pass through an electric field. In this way the electrons paths are deviated according to their kinetic energy. There are multiple versions of this kind of analyser; we will discuss only the hemispherical one, sketched in Figure 13, since it is the one present at the PLEIADES beamline. This system has a compact

structure and is the most commonly employed XPS analysing system[40]. The electrons need to be transmitted with an energy equal to $E = e.V$ along a semi-circular pathway with a radius equal to R surrounded by an inner applied electric potential V_1 (with a radius R_1) and an outer one V_2 (with a radius R_2). The two voltages are given by the formulae:

$$V_2 = V[2(R/R_2) - 1]$$

and

$$V_1 = V[2(R/R_1) - 1]$$

The energy resolution of the analyser can be described as the ability to resolve two adjacent peaks separated by a ΔE. It is given by the following formula for a given energy E, where the parameters a, b, and c are constant characteristics specific to the analyser; ω is the width of the entrance slits (S1 on Figure 13); $\Delta\alpha$ and $\Delta\beta$ are the angular deviation of the electrons emitted by the sample in the deflection and perpendicular plane, respectively[40]:

$$\Delta E/E = a\omega + b(\Delta\alpha)^2 + c(\Delta\beta)^2$$

In the case of the hemispherical analyser, the value of c is equal to zero. The maximum focussing is achieved in the plane perpendicular to the deflection one[40].

After having passed through the analyser, the electrons are detected by an electron multiplier. Nowadays, there are two main methods, the channeltron and the Micro-Channel Plates (MCPs). The utilised set-up employs an MCP detector.

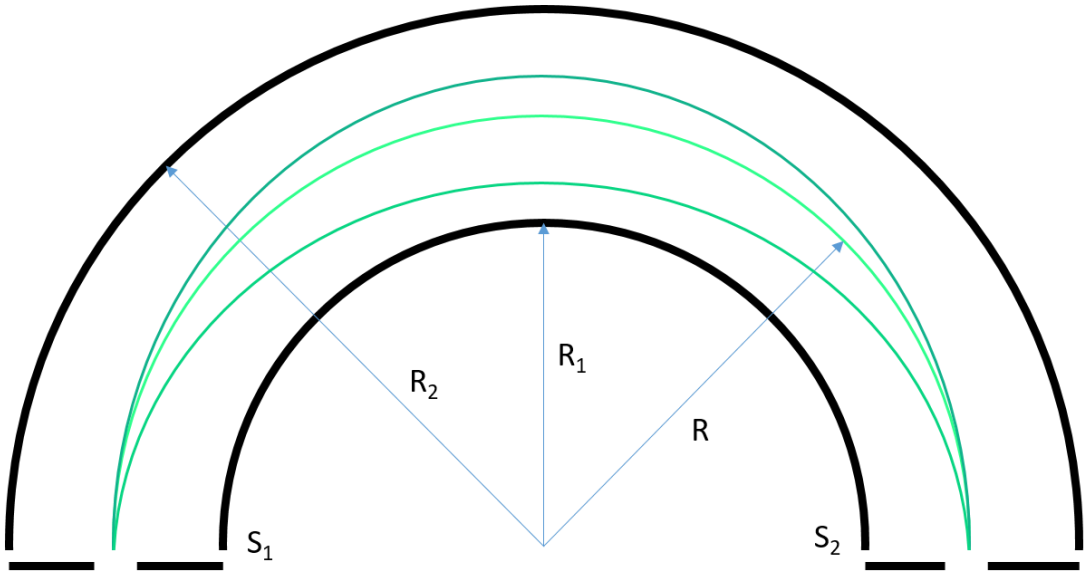

FIGURE 13: SCHEMATIC REPRESENTATION OF A HEMISPHERICAL ANALYSER. S_1 AND S_2 ARE THE ENTRANCE AND EXIT SLITS OF THE ANALYSER, RESPECTIVELY. THE DRAWN TRAJECTORIES HAVE ONLY A DEMONSTRATIVE PURPOSE.

3.3 COMPARISON AND COMPLEMENTARITY OF THE DIFFERENT EXPERIMENTAL APPROACHES

As we have seen from this brief description, the employed methods, namely mass spectrometry, either coupled to ion-induced fragmentation or VUV photoabsorption, and X-ray photoelectron spectroscopy, provide a different set of information each, which together can contribute to a more complete description of the hydration of a hypoxanthine molecular cluster. Using mass spectrometry, we can obtain information, such as the weakest bonds by analysing the isolated molecule fragmentation, the atoms involved in the hydrogen bonds formation by observing the fragmentation of the clusters, and the cluster growth of both pure and hydrated species. Thus, with mass spectrometry, we can obtain information on the molecule geometrical structure and stability. With XPS spectrometry, the obtained information resides in the characterisation of each element composing the molecule, in particular their electronic structure and thus their molecular

environment. By relating the different information obtained from these different experimental approaches, we can obtain a rather complete picture on how the increasing system complexity and the chemical environment affect the hypoxanthine molecular stability, i.e. its ability to withstand ionizing radiation. This kind of information can be useful when examining how molecular fragments act in a normal biological environment, and if the aqueous environment could help quenching the production of reactive species.

4 EXPERIMENTAL METHODS

IN THIS CHAPTER, WE DESCRIBE THE TECHNICAL FEATURES AND THE EXPERIMENTAL METHODS, EXPLAINING HOW, IN PRACTICE, THOSE METHODS ARE IMPLEMENTED AND USED. OUR EXPERIMENTS TOOK PLACE IN TWO FACILITIES WITH THE UTILISATION OF FIVE DIFFERENT EXPERIMENTAL SET-UPS, WITH DIFFERENT OPTIMISATIONS, TO BETTER SUIT EACH EXPERIMENT.

4.1 THE TARGET SOURCES

During the course of this thesis, we employed two kinds of molecular beam sources: one for the production of an isolated neutral molecular beam, and one for neutral molecular clusters. Both sources, described in the following, are based on the oven principle and rely on the difference of pressure between the inside of the oven, filled with the homogenously heated sample, and the vacuum of the rest of the chamber to produce a continuous effusive gaseous jet of neutral molecules[43]. The isolated molecule source was employed only on the COLIMACON set-up, while the cluster source was used for experiments carried out on the COLIMACON set-up at the ARIBE beamline of GANIL and on the DESIRS and PLEAIDES beamlines at the SOLEIL synchrotron.

4.1.1 THE ISOLATED MOLECULE SOURCE

The isolated molecule source consists of an oven made of two superposed hollow molybdenum cylinders. The first is a reservoir part with an inner diameter of the order of centimetres, which is filled with the sample powder prior to the experiment. The second consists of a cavity of a few millimetres wide, and is the channel through which the isolated molecules are ejected (see Figure 14). A heating thermocoax wire, which can efficiently produce a homogenous heat, wraps these two oven components. Since the oven, placed in its support, is kept under vacuum conditions during the experiment, the heated powder expands in the reservoir, sublimates in the gaseous phase and exits through the thin-necked part of the oven. This process leads to the formation of an effusive gas jet of neutral molecules[43]. This process follows the Clausius-Clapeyron formula, which describes the

variation of the pressure dP in relation to the variation of the temperature dT, as a function of the latent heat L (which is the energy absorbed or released by a body in a constant-temperature process), the temperature T and the volume variation Δv occurring during the phase transition. This formula can also be expressed as a function of the variation of the system entropy in the phase change:

$$\frac{dP}{dT} = \frac{L}{T\Delta v} = \frac{\Delta S}{\Delta v}$$

In fact, by being heated up in the constant crucible volume, the powder expands, liquefies, and then boils into gas. In the case of hypoxanthine, and other biomolecules, the temperature to be reached is in the order of 190 °C. The pressure increase forces the gas to exit the oven. Once the vaporised powder exits the oven, it produces a diverging conical jet. In order to obtain a more collimated molecular beam, the jet passes through a diaphragm with a diameter of 0.53 cm, placed 7 cm after the oven, and 10 cm before the interaction zone. This produces a target density of 10^8-10^9 molecules/cm^3.

4.1.2 THE CLUSTER SOURCE

The concept behind the design of an aggregation source based on the ejection of the sample in gaseous form thanks to the crucible heating is similar to the one used for the isolated molecule beam production. Here, as further explained below, the use of a buffer gas is required to favour the aggregation process. For all the experiments presented in the following and involving clusters, we employed two examples of the same model of cluster source. Figure 15 schematically describes the two sources, although it represents specifically the CELENO cluster source used in the experiments taking place at the SOLEIL synchrotron. This kind of source can produce large-sized clusters, forming up to 100-mers, depending of the composition of the studied molecule[44]. Another interesting feature of this type of cluster source relies in its ability to produce clusters characterised by different

non-covalent interactions. Such sources have been used to produce fullerene[45,46] and polycyclic aromatic[47] clusters linked by Van der Waals forces; or H-bonded clusters formed by water[48,49] or hydrated biomolecules[8,50,51], such as the one treated in this work.

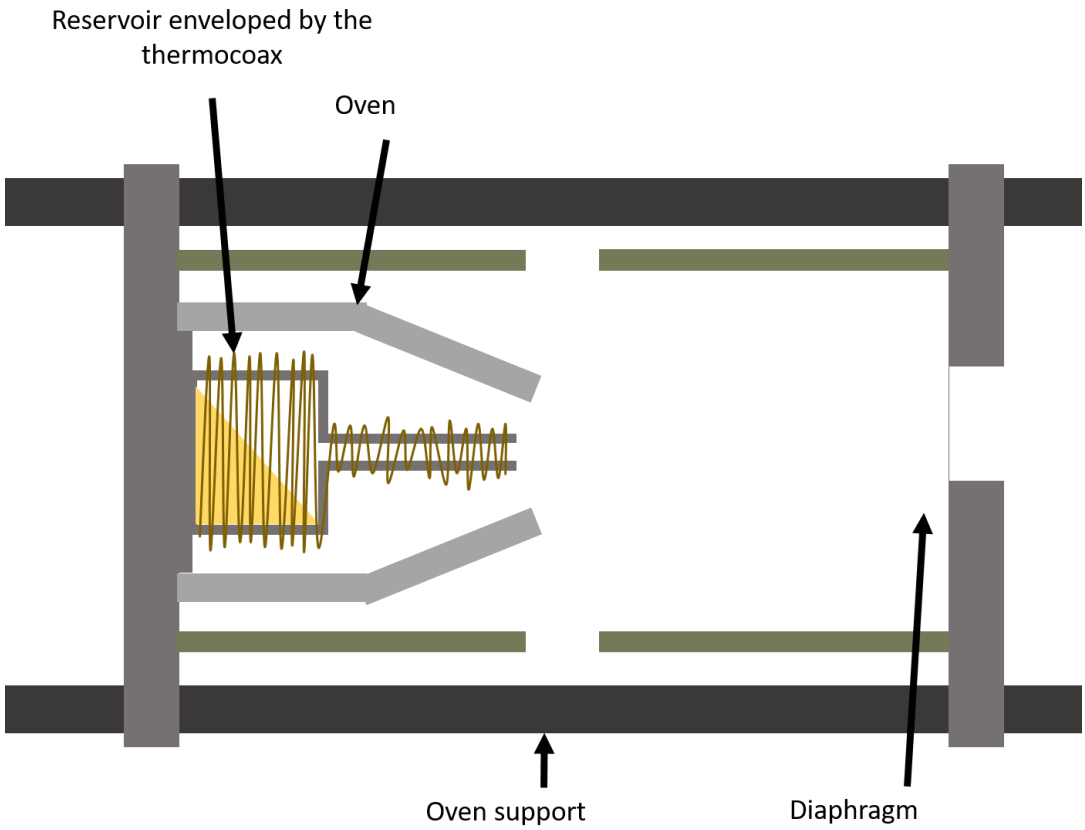

FIGURE 14: SCHEMATIC REPRESENTATION OF THE ISOLATED MOLECULE SOURCE. WE CAN OBSERVE THE RESERVOIR WRAPPED BY THE THERMOCOAX, PLACED INTO THE OVEN. THIS IS THEN PLACED IN THE SUPPORT TO BE MOUNTED ON THE COLIMACON SET-UP.

The process exploited in this kind of cluster source is the attachment of a new molecule to the gaseous monomer thanks to the collision between the two molecules[43,52]. The buffer gas, such as helium or argon, absorbs the excess energy produced by the formation of the non-covalent intermolecular bonds. Thus, this whole process takes the name of three-body collisions. The presence of the buffer gas makes a significant difference between the isolated molecule source and the cluster source as

the latest requires the use of the buffer gas to attenuate the collision energy, which otherwise would favour the detachment rather than the attachment of other molecules. It is noteworthy mentioning that the buffer gas also carries the formed clusters out of the source into the analysing chamber; for this reason, it is also called carrier gas. In order to maintain the cluster formed and prevent its dissociation, the temperature at which the aggregation takes place has to be sufficiently low, by keeping it at around -185 °C. In order to achieve such temperature, the cluster formation occurs in a dedicated part, called the condensation channel, made of a doubly walled duct through which liquid nitrogen (LN_2) circulates, thus refrigerating the system. There, the collisions of the buffer gas with the cold walls of the channel help the formed clusters reaching a thermal equilibrium while exiting the source.

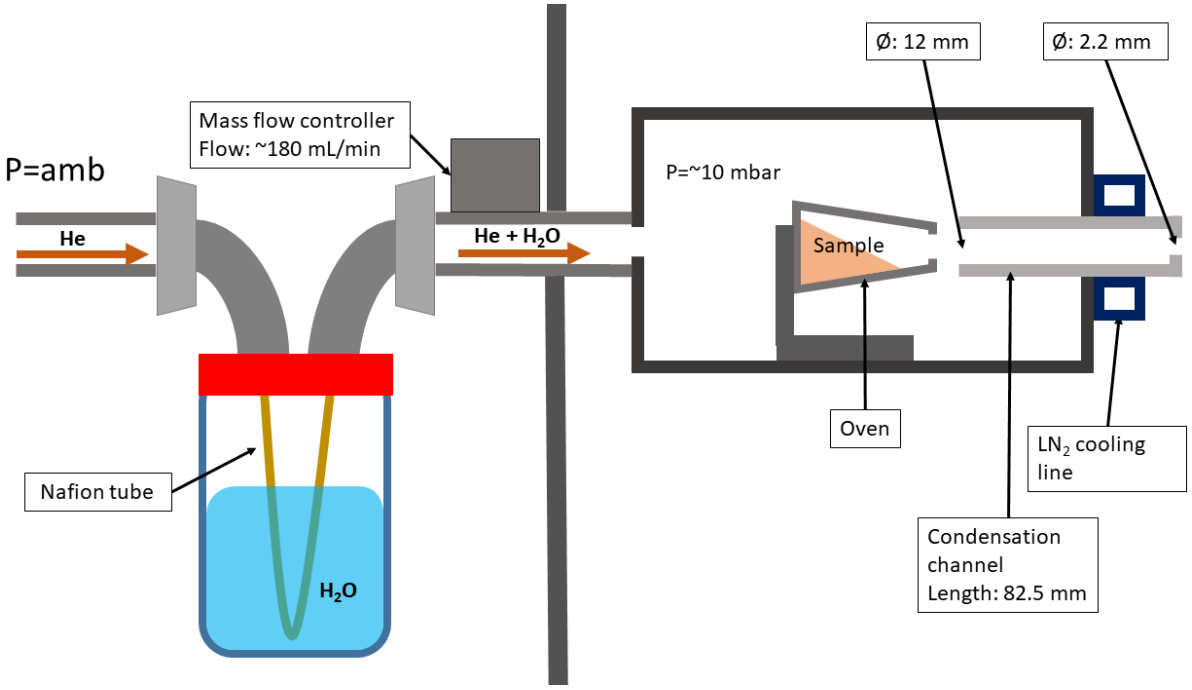

FIGURE 15: SCHEMATIC REPRESENTATION OF THE CELENO GAS AGGREGATION CLUSTER SOURCE, EQUIPPED TO PRODUCE HYDRATED CLUSTERS. THE CLUSTER SOURCE CHAMBER HAS A DIAMETER OF 140 MM AND A HEIGHT OF 90 MM.

The design of the employed cluster sources is based on Bergen's one[53], which is an adaptation from the one designed by Bréchignac[54], and it is represented in Figure 15. It is composed of a stainless steel chamber presenting a diameter of 140 mm for a 90 mm height and a movable lid on top, allowing the positioning of the oven in the middle. The chamber is kept under vacuum conditions. It presents two openings on the opposite sides: one to let the buffer gas line in and the other one to allow installation of the condensation channel, which lets the molecules flow out into the interaction chamber. A Brooks SLA5850 (Brooks instrument, Hatfield, USA) controller regulates the buffer gas flow, helium in the case of our experiments, usually kept at 150-200 mL/min. The helium pressure inside the source chamber is maintained at roughly 10 mbar and is measured by a CERAVAC CTR 100 capacitive gauge, produced by Leybold (Leybold GmbH Cologne, Germany). The oven, in which the sample powder is stored inside the chamber, consists of a stainless-steel cylinder with a 3 cm^3 capacity, wrapped by a resistive heating wire. The oven temperature is recorded and controlled by a thermocouple placed on its back. The oven's reservoir is filled prior to each experiment by opening the chamber, dismounting the oven and refilling it. Thus, each time the reservoir is empty, the experiment has to be stopped and the chamber vented. The reservoir presents an opening facing the inner orifice of the condensation channel, which has an inner diameter of 12 mm. The channel is 82.5 mm long, is double walled, with the LN_2 passing through the interstice of the two walls. The exit aperture of the condensation channel is reduced to 2.2 mm in diameter. In order to control the cluster growth, we can regulate several parameters in the cluster source, from the oven up to the condensation channel[44]. The first parameter that can be adjusted is the oven temperature, regulated by the current passing through the heating element enveloping the steel oven. By increasing the temperature, the sample vapour pressure also increases, hence increasing the flux of molecules ejected from the crucible. The second parameter that can be regulated is the buffer gas properties. Both the element employed as buffer gas and its pressure affect the cluster growth. The pressure controls the

number of collisions in the condensation channel. As described by Zimmermann *et al*[44], the lower the pressure of the gas, the bigger the cluster. The element used for providing the buffer gas also affects the effectiveness of the formation of bigger clusters. The heavier elements, such as argon, guarantee a larger energy transfer during the three-body collisions, thus forming larger clusters than the ones obtained with lighter inert gases, such as helium[44]. The last parameter that can be adjusted in order to variate the size of the cluster, is the length of the condensation channel and its temperature: the longer the channel the higher number of collisions with the LN_2 cooled walls, the larger the clusters; and the colder the walls, the more rapidly the cluster reaches the thermal equilibrium[44]. Unfortunately, the length of this condensation channel cannot be regulated and it is technically difficult to employ more effective cooling systems than liquid nitrogen.

Helium was chosen as the carrier gas in our experiments[77]. Employing this gas, we could obtain clusters containing in the order of tens of molecules. Bigger clusters were not of prime interest in the present work, since the aim of the experiment was to probe whether the production of clusters of both pure and hydrated species was feasible or not. The growth of the clusters was controlled thanks to the variation of two parameters: the oven temperature and the buffer gas flow.

The production of hydrated clusters was performed following the procedure designed by Kocisek[55]. This method relies on the hydration of the buffer gas before entering the cluster chamber. To do so, the carrier gas line is let pass through a closed cup filled with ultra pure water (MilliQ). The gas flow is able to take up water molecules by passing through a porous channel permeable to water (Nafion®). By modifying the area of the tube in contact with water, we were able to obtain different levels of hydration when producing the clusters: for example if the tube was only a few mm above the water surface, we could produce lightly hydrated clusters, containing up to seven water molecules. On the other hand, if it was submerged, the hydration was more important with up to eleven water molecules for a dimer cluster.

4.2 SETUPS

During this project, the experiments took place at two different facilities: at the COLIMACON set-up of the ARIBE facility in the GANIL site in Caen; and at two beamlines, PLEIADES and DESIRS, of the SOLEIL synchrotron in Gif-sur-Yvette. Those two facilities employ two very different means of investigation; while at ARIBE the essay beam is composed of ions; at SOLEIL it is a photon beam.

In this section, we will present a description of those set-ups with a brief description of the beamlines. In the first place, we will define how the different essay beams are produced and transported to the set-up/end-station. Then, we will describe how the target powders and solutions are put into the gas phase and how the target species interact with the essay beam in the set-up. At this point, the focus will go into what happens when the interaction takes place, how the interaction products are detected, and how their detection leads to interpretable data.

4.2.1 SETUPS FOR EXPERIMENTS WITH IONS

The first set-up to be described is COLIMACON (”COLlision entre des Ions et des Molécules ou des Agrégats COmplexes Neutres” which translates to “Collision between ions and complex neutral molecules or clusters”). The set-up is installed at the ARIBE facility (“Accélérateur pour la Recherche sur les Ions de Basse Énergie” which means “Accelerator for the research on low energy ions”) of the GANIL facility (“Grand Accélérateur National d’Ions Lourds” which means “Great national accelerator for heavy ions”). As it can be seen from the acronyms, this set-up focuses on the interaction between low energy, multiply charged ions and neutral molecules (or clusters of molecules) in the gas phase.

4.2.1.1 ARIBE

The ARIBE platform hosts an Electron Cyclotron Resonance (ECR) ion source, which produces multi-charged ions A^{q+} at low energy (5-20 keV per charge unit)[56]. The ion beam is produced by applying a high frequency electromagnetic field at 14.5 GHz with a power that can rise up to 1000 W and a static magnetic field to a gas kept at low pressure (roughly 10^{-5} mbar) in order to obtain a hot plasma, by detaching electrons[57]. An extraction voltage is applied to extract the produced ions from the source. Hence, the ions exit from the source by passing through an extraction tube, and fly towards the measurement set-up. The beam is then selected to the desired mass and charge by a magnetic dipole, and directed to the end station while still being put into shape. Before entering the interaction zone, the ion beam passes first through a deflector, or chopper, which consists of two plane electrodes that allow the pulsing of the beam. After that, the beam goes through an Einzel lens that focuses the beam into the collision zone.

4.2.1.2 COLIMACON

The installation consists of a crossed-beam time-of-flight (TOF) spectrometer device in which the molecular beam, produced as described in the previous sections, crosses the projectile ion beam, as seen in Figure 16. Upon interaction, the products are analysed according to their mass-to-charge ratio *m/z*, either as a simple mass spectrum, or in coincidence, in order to understand the phenomenon leading to the formation of the observed fragments. This technique allows, e.g., the investigation of the fragments formed during the collision, the formation of clusters and their size, and the stoichiometry of the different species involved in the case of mixed clusters.

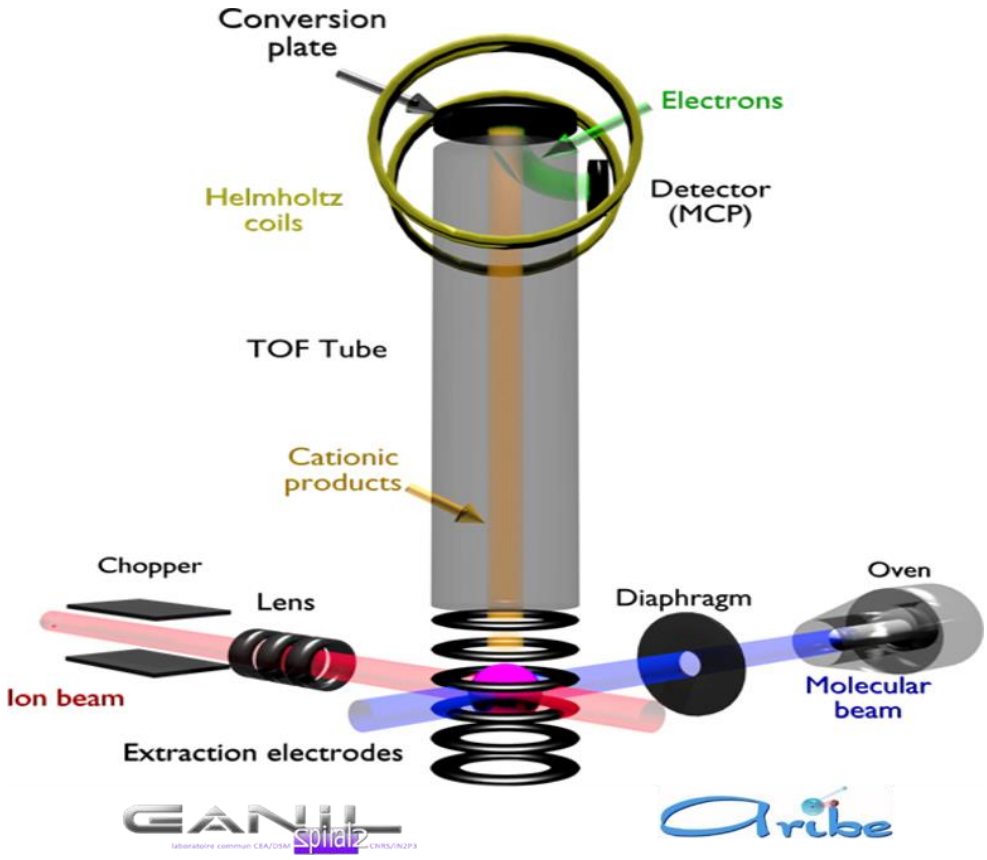

FIGURE 16: SCHEMATIC REPRESENTATION OF THE COLIMACON SET-UP.

Briefly, this mass spectrometer is composed of three parts: an extraction zone, where the abovementioned interaction takes place, the free-flight zone, and the detection zone in the end.

The first zone, the extraction zone, is where the collision between the target and the projectile beams takes place. Here the newly formed charged products are extracted towards the time-of-flight zone. This area is divided into two parts, according the Wiley-McLaren principle in order to time focus the charged fragments into the plane of the detection zone, thus increasing the mass resolution of the spectrometer[58]. The two parts composing the extraction zone are the extraction zone, strictly speaking, and the acceleration zone. The first zone is 110 mm long, composed of a circular electrode plate to which a voltage of 2.681 kV (V_{ext}) is applied, and of eleven parallel rings with an external diameter of 130 mm, an internal

diameter of 90 mm, and a thickness of 1 mm. The electrodes are placed at 10 mm from each other and connected by means of a resistive bridge. The eleventh ring is grounded, thus producing a potential difference of 2.681 kV with the first plate. The last ring disc is covered by a 94% transmission metallic mesh, which guarantees the homogeneity of the electric field that is formed in this zone at the border with the acceleration zone. The electric field is of 244 *V/cm*, and allows the extraction of the charged particles. The acceleration zone is composed of three additional rings, presenting the same characteristics as the other eleven rings. The first ring is grounded, while the last one, equipped with the 94% transmission mesh, is set at a voltage of -5 kV. This allows the formation of a second electric field of 1667 *V/cm* to further accelerate the charged products. The structure of this extraction zone, with the two electric fields, essentially compensates for the energy distribution due to the initial spatial spread of the product ions in the extraction zone. The system is placed under a thermal screen with four holes to allow the passage of the two beams. It is cooled down with liquid nitrogen, down to -196 °C, to trap the residual gas, such as CO_2, O_2, N_2, H_2O, and sensibly reduce the detection of their ionic products.

The free-flight zone is composed of a tube one meter long made of two metal electrodes kept at -5 kV, the same voltage as that of the last ring of the acceleration zone, and several small electrode plates that can apply a transversal electrical field. The metal plates are 99 cm long, 12 cm wide, 0.5 cm thick, and placed at 10.3 cm of distance one from the other, while the small plates measure 98 cm in length, 1.5 cm in width and 0.1 cm thick, and guarantee the homogeneity of the transversal electric field. At the end of the TOF tube, there is a 94% transmission mesh, which ensures a homogenous electric field. A view from the top of the free flight zone is shown in Figure 17.

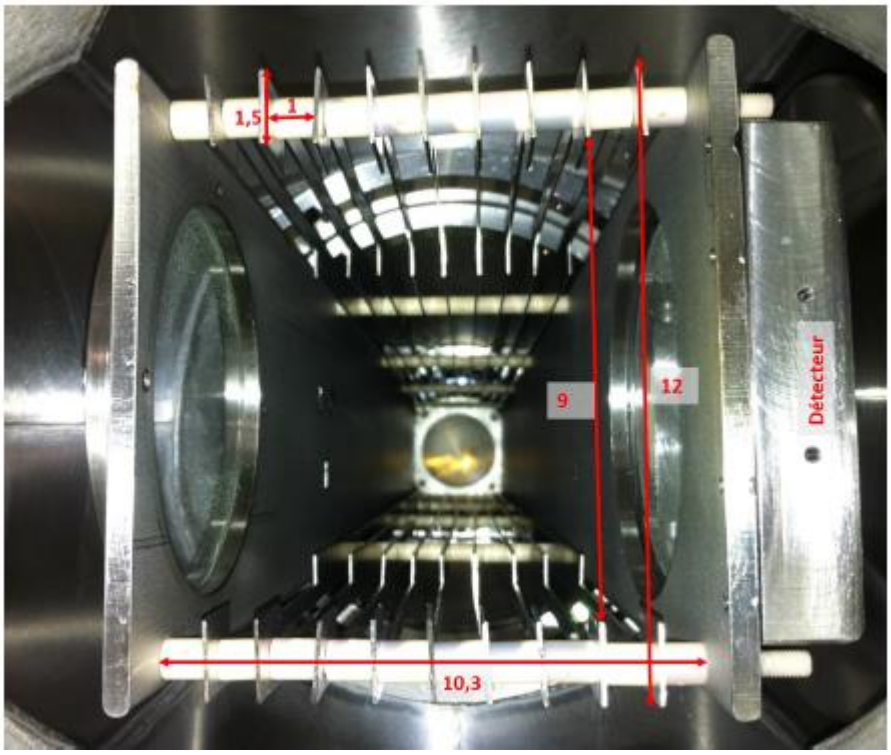

FIGURE 17: THE FREE FLIGHT ZONE, AS SEEN FROM ABOVE. THE LENGTHS ARE EXPRESSED IN CM.

The detection zone is where the charged products arrive, after having travelled through the time of flight tube, where they are treated by a Daly type detector[53,59,60]. This detection system is composed of three parts: a conversion plate, two Helmholtz coils, and a Z-stack of three micro-channel plates (MCPs). The conversion plate is placed 2.8 cm from the time of flight mesh, with a diameter of 15 cm, a thickness of 2.7 cm with rounded brims to avoid clacking. During the experiment, a voltage of -19 kV is applied to it, which with the -5kV potential of the TOF tube, produces another electric field of 5 kV/cm. Here the charged fragments are sufficiently accelerated to emit secondary electrons when they hit the plate, which guarantees a satisfactory detection efficiency, even in the case of heavy cations. The produced electrons go towards the MCPs, guided by the magnetic field produced by Helmholtz coils, which have a diameter of 60 cm. The electrons accelerate towards the MCPs thanks to the potential difference between the latter and the conversion plate. At this point, the three micro-channel plates of a 40 cm diameter increase the number of secondary

electrons by means of an “avalanche” and its conversion into signal is performed by the copper anode, while the electronic chain grounds it. Going into further details, when the electrons emitted from the conversion plate hit the first MCP, they encounter a potential of -17.5 kV; then, the second one set at -16.8 kV, and the third at -15.4 kV. This variation of 700 V per MCP guarantees the amplification of the number of secondary electrons by several orders of magnitude, so that up to 10^7 to 10^8 secondary electrons hit the copper anode for each cation impacting the conversion plate.

For such a geometry of time-of-flight spectrometer, the total flight time, t, of a charged particle of mass m and charge z, formed in the extraction zone, is given by[60]:

$$t = k\sqrt{\frac{m}{z}}$$

where k is a constant only depending on the spectrometer geometry and applied voltages. Thus, the only variable determining the time taken by a charged product to pass through the TOF tube is its mass-to-charge ratio. This guarantees the discrimination of each type of charged products according to their m/z, thanks to the different arrival times on the detector.

The acquisition system of the obtained data works as follows. For each charged particle hitting the conversion plate, an avalanche of electrons is produced by the three MCPs. These electrons create on the anode a negative electric signal, with a varying intensity, depending on the number of the incident electrons hitting the MCPs.

It is noteworthy to mention that this set-up requires the projectile ions, as well as the interaction zone voltages to be pulsed. As mentioned previously, the projectile ion beamline is equipped with a chopper to produce short ion bunches which are injected in the interaction zone. Subsequently to the projectile ion bunch interacting with the target molecular beam and leaving the interaction zone, the voltages on the extraction zone electrodes are applied and all cationic products are pushed forward in the TOF spectrometer. This pulse serves as start-time for the time-of-flight

spectrum. This pulsing scheme also prevents extracting the projectile ion beam in the TOF spectrometer, which would cause important noise signal.

The pulses are put in place thanks to the QUANTUM Composers 9514+ (Quantum Composers Inc., Bozeman, USA) pulse generator, which produces transistor-transistor logic (TTL) integrate circuit-type signals that can be adjusted in the duration frame. The frequency chosen is common to all of the pulsed signals, and it is of a few kHz. In total, four inputs are pulsed on the COLIMACON set-up: the extraction voltage, the projectile ion chopper, and the input giving the time frame for the system to acquire the signal. A fourth pulsed input is sent to be transformed into a NIM signal, in order to provide a temporal reference to the acquisition.
Going more into details, the channel A of the pulse generator provides the signal that controls the pulsing of the projectile ion beam into packages (Figure 18). This signal is used to define the initial starting time T_0. This signal is sent to a Behlke GHT 60 pulser (Behlke, Frankfurt, Germany). This pulser regulates the tension of one of the two plate electrodes of the chopper through which the projectile beam passes before arriving in the interaction zone. While one of them is kept constantly at -1 kV, the one connected to the pulser oscillates between 0 and -1kV: it is set to -1kV during the pulse duration T_{ions}, which in the present work has been set at 0.5 µs for the isolated molecules and 1 µs for the clusters. The adjustable repetition time (T_{rep}) of the pulses was set at 240 µs for the isolated hypoxanthine, and at 320 µs for its clusters. Hence, the projectile ions are allowed to pass through the beam chopper only when the voltage is -1 kV on both of its electrodes. The channel B of the QUANTUM pulse generator works similarly to A: by controlling another Behlke GHT 60 pulser, this channel regulates the voltage in the first part of the extraction zone, which is set at 2.681 kV when extraction is operating. The delay of the extraction time, $T_{delay,}$ depends on the velocity of the employed projectile as we wait until the projectile bunch has left the interaction zone before applying the extraction voltage. In this experiment, T_{delay} was set at 8.8 µs for the isolated molecules and at 9.3 µs for the clusters. The duration T_{ext} of the

extraction pulse depends on the mass of the analysed species in order to extract all of the resulting charged particles out of the extraction zone. In the case of isolated molecules, the employed duration T_{ext} was 4 µs, while it was set at 8 µs in case of clusters. The third channel of the pulse generator, called C, allows the creation of a non-acquisition (veto) time frame on the signal obtained by the discriminator. In this way, the part of the signal corresponding to background pollution can be omitted from the final spectrum in the parts where they are expected to appear. The fourth channel, called D, sends a TTL signal synchronized with B, which is converted into a NIM signal sent to the acquisition card, giving the time reference START for the acquisition time. Later, the acquisition card interprets a STOP signal for each detected charged particle when it is being detected. In this way, the difference of time between a STOP and a START makes the time of flight taken by the particle between its extraction and detection. This obtained spectrum is then calibrated from a TOF one into an m/z one. The calibration is user performed, and it relies on the direct proportionality between the TOF and the $\sqrt{m/z}$ value of a given charged product, as previously mentioned. A summary of the acquisition system is provided in Figure 18.

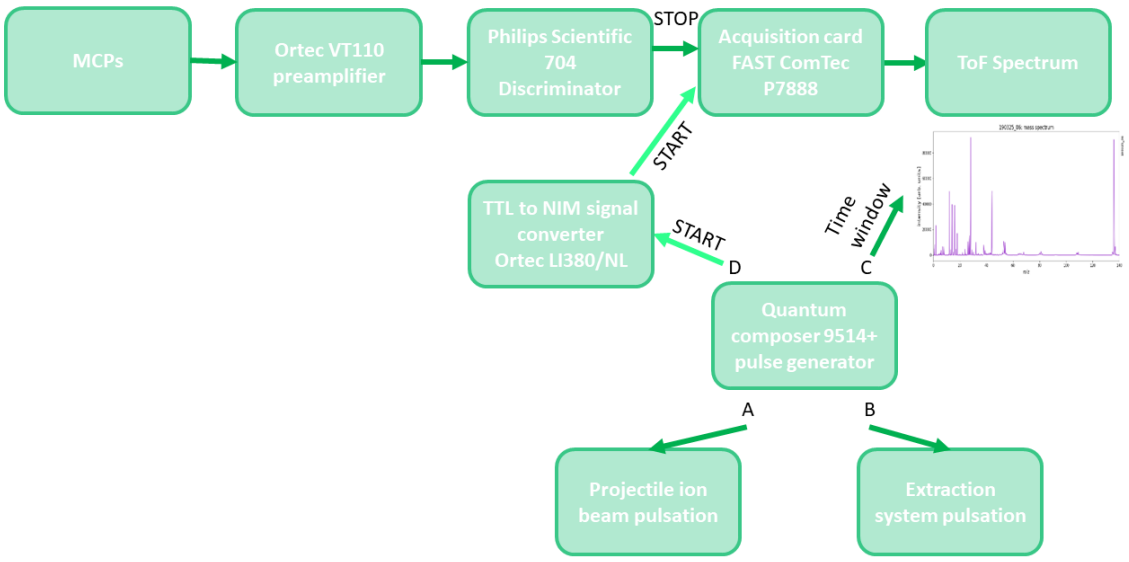

FIGURE 18: SCHEMATIC REPRESENTATION OF THE ACQUISITION SYSTEM.

To achieve the calibration, it is necessary to use some known reference peaks. These points are then put in relation between their TOF and m/z using a fourth-degree polynomial curve. Although second-order polynomial curve should theoretically be enough, in practice, field inhomogeneities induce small deviations and higher order polynomial fit becomes more precise. This gives the calibration of the mass spectrum.

4.2.2 SETUPS FOR EXPERIMENTS WITH PHOTONS

4.2.2.1 SOLEIL

The SOLEIL synchrotron is the facility at which our experiments employing photons took place. SOLEIL ("Source Optimisée de Lumière d'Énergie Intermédiaire du LURE" which translates to "Optimised source for LURE intermediate-energy light from LURE") belongs to the third generation of synchrotrons with an energy of 2.75 GeV, which allows for covering the energy range from the infrared to the hard X-rays[61,62]. It has been inaugurated in late 2006, as an upgraded version of the older, and now dismantled, LURE installation, ("Laboratoire pour l'Utilisation du Rayonnement Electromagnétique" or "Laboratory for the utilisation of electromagnetic radiation"). It presents 29 beamlines; each focus on specific energy ranges, and thus, on specific employed techniques, sample types and aggregation states.

4.2.2.2 PLEIADES

The XPS experiments conducted in the context of this work have taken place at the SOLEIL beamline PLEIADES, which is dedicated to the study of diluted matter, namely gaseous samples by employing photons in the soft X-ray range. The PLEIADES beamline used in the present experiment is based on a permanent magnet APPLE II type undulator, with a period of 80 mm, in combination with a high-flux, 600 lines/mm grating of the modified Petersen plane grating monochromator, covering the energy range between 10 and 1000 eV[63,64]. In order to measure the X-ray photoelectron

spectra of cluster targets, we employed the VG Scienta R4000 hemispherical electron energy analyser end-station coupled to the multi-purpose source chamber (MPSC)[63]. The CELENO cluster source was installed inside the MPSC (Figure 19). This system does not present a differential pumping stage, which is present on the DESIRS beamline, presented below. The pressure in the MPSC is kept at high 10^{-5} mbar. The working pressure in the interaction chamber is typically in the range of high 10^{-6} mbar to low 10^{-5} mbar, with a base pressure in 10^{-8} mbar. The source can be moved close to the interaction zone, through a metallic arm belonging to the MPSC chamber, ended by a skimmer and entering inside the interaction chamber hosting the Scienta high resolution spectrometer, close to the interaction region. In the present experiment, the distance between the cluster source and the skimmer was set to 22 mm. The exit of the cluster source can be moved on the "molecular beam direction", the X axis, and the Y axis, perpendicular to the molecular beam, which can be considered the "photon beam direction", while on the Z axis it can be vertically aligned to the skimmer. The skimmer can be also independently moved on the Z and Y axes, in order to guarantee an alignment between the molecular beam and the photon beam[63]. The distance between the skimmer and the photon beam is of 30 mm. The interaction chamber can be moved perpendicularly to the cluster beam direction, in order to align the interaction region with the Scienta analyser entrance lens.

The Scienta analyser is a commercially available spectrometer, designed specifically for the measurement of the energy of the photoelectrons. The energy range guaranteed for the XPS experiments is between 5 and 1500 eV. As described in the introduction, this kind of setup presents two hemispherical concentric plates, to which a different potential is applied. This spectrometer is composed of three principal parts: the electrostatic lens, the analyser *in stricto sensu*, and the detection system. The lens focalises the electrons before letting them pass through the entrance slits. The size of the opening of the slits largely regulates the resolution of the obtained spectrum, as follows:

$$RP = \frac{2r}{s}$$

where RP is the resolving power (resolution), r is the analyser radius, and s is the slit width.

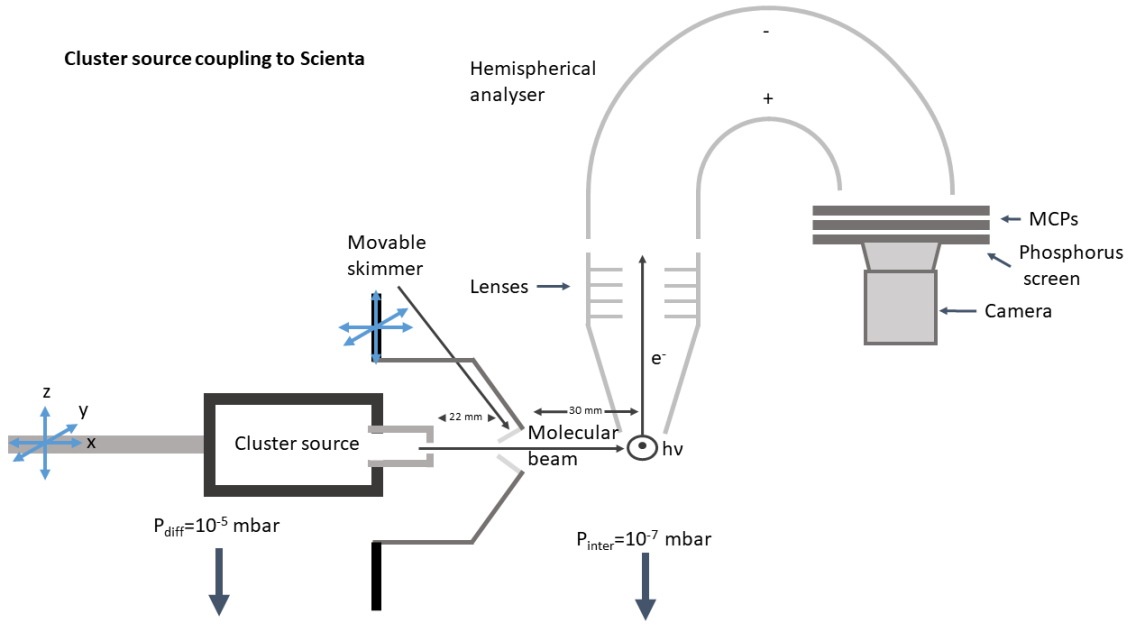

FIGURE 19: SCHEMATIC REPRESENTATION OF THE CELENO CLUSTER SOURCE COUPLING TO THE SCIENTA SPECTROMETER IN PLEIADES.

The analyser has a mean radius of 200 mm, the electric potential applied to the two electrodes forming it depends on the selected pass energy. The obtained electric field deviates the entering electron according to their incident energy. This allows the detection of the electrons at the opposite end of the analyser. Here, there are two microchannel plates (MCPs) that multiply the number of the received electrons, obtaining up to 10^6 secondary electrons per detected electron. The two MCPs are placed right before a phosphorus fluorescent screen, which is placed in front of a CCD camera. In this way, when the electrons hit the screen, they produce a light flash, which is recorded on the camera. This camera, communicating with the Tango system, provides a 2D image; according to the position of the spots on the image, we can extract information regarding the energy and angular distributions of the photoelectrons. The obtained data are

transmitted thanks to the data transfer system Tango, which imports the information to the Igor Pro analysing software.

4.2.2.3 DESIRS

The DESIRS beamline provides intense VUV radiation of fully controllable linear or circular polarisation in the 4-40 eV photon energy range[65]. The photon beam is produced by an electromagnetic undulator (HU64/OPHELIE2) whose high harmonics are efficiently removed by using a gas filter[65] prior to the 6 m long normal incidence monochromator. This monochromator is equipped with various gratings, which ensure a fine-tuning of the beam energy and energy resolution. In the context of this thesis, we chose a moderate resolution of around ~ 10 meV at 10 eV photon energy. This setting ensures a rather high flux in the range of a few 10^{12} photons.sec^{-1}. The CELENO cluster source described in the previous paragraph has been coupled to the permanent molecular beam chamber SAPHIRS[66] equipped with the double imaging photoelectron/photoion coincidence (i2PEPICO) spectrometer DELICIOUS 3[67] (Figure 20), permanently installed on the branch A of the beamline. The DELICIOUS 3 spectrometer allows coincident detection of photoions and photoelectrons produced by each given photoionisation event. Photoelectrons are detected via a velocity map imaging (VMI) spectrometer, allowing the determination of their kinetic energy and angular distributions, after the Abel inversion of the recorded images.

As depicted in Figure 20, the ion side of the spectrometer consists of a modified Wiley–McLaren time-of-flight mass spectrometer, featuring additional lenses to allow for the determination of ion kinetic energy release, called IKER, that had not been used in the scope of this work. The photoions are extracted perpendicularly to the direction of the molecular beam. A deflector electrode in the ion flight tube is used to ascertain that also heavy ions with a large initial momentum in the direction of the molecular beam reach the 40 mm position-sensitive detector (PSD) equipped with MCPs. In the DELICIOUS 3 spectrometer, ions are accelerated to ~ 3800 eV. In this kinetic energy range the microchannel plates detection efficiency decreases between masses of 100 u and

~ 3000 u by about a factor of 2, according to Fraser[68]. The design of the coincidence detector is set to make sure that the Velocity Map Imaging (VMI) data obtained from the electrons coming from the MCPs is distributed/filtered according to the m/z of the relative ion, which originated the electron avalanche, and the position where charged particle hit the ion detector on its the Region of Interest (ROI). The latter allows an additional separation of the background signals, arising from impurities in the 10^{-8} – 10^{-6} mbar working vacuum, from the signals corresponding to the species of interest originating from the molecular beam.

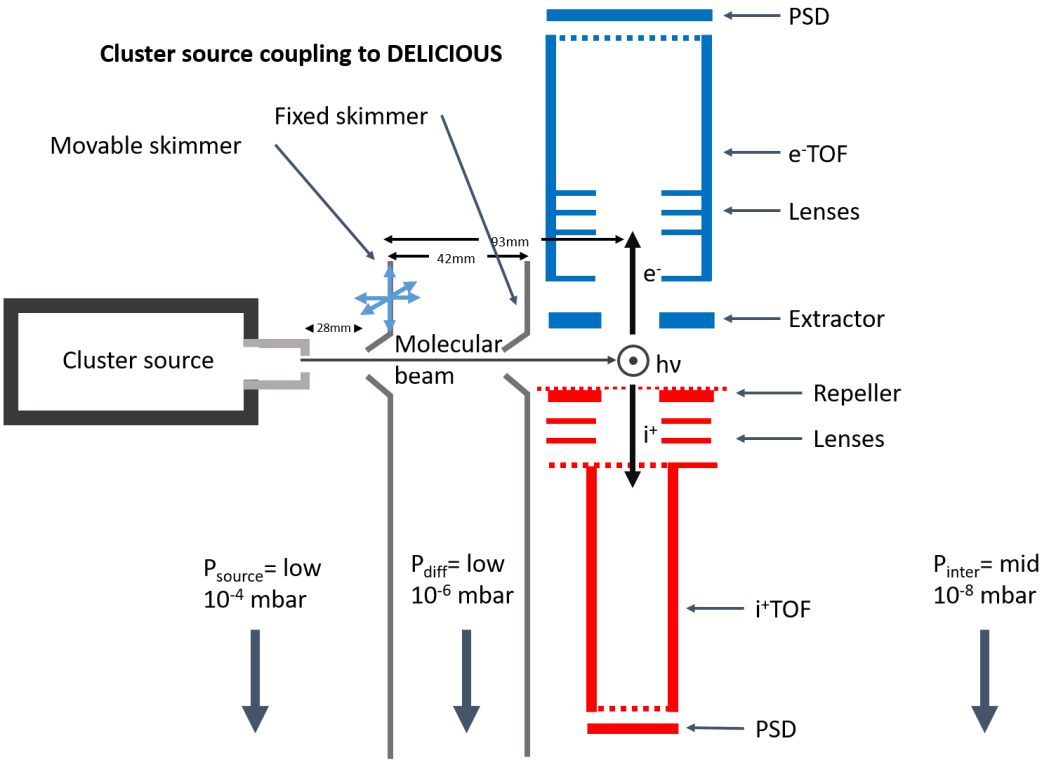

FIGURE 20: SCHEMATIC REPRESENTATION OF THE CELENO CLUSTER SOURCE COUPLED TO THE DELICIOUS 3 SPECTROMETER AT THE DESIRS BEAMLINE.

In our experiment, the CELENO cluster source has been installed in the source chamber for the production of molecular beams, SAPHIRS, which is connected to the DELICIOUS 3 spectrometer chamber of the branch A of the DESIRS beamline. This arrangement implies a two-skimmer differential pumping stage, which separates the source chamber from the

interaction one. The transitional vacuum, of about 10^{-6} mbar, present between the two skimmers, allows keeping the DELICIOUS 3 chamber at a pressure of about 10^{-8} mbar, while the SAPHIRS one is put at ambient pressure when operating on the cluster source (e.g., when refilling the oven with sample powder).

As mentioned, the CELENO cluster source was placed in the SAPHIRS chamber, mounted on a holder, and fixed to the first skimmer at an adaptable distance, which was set at 5 mm during our experiment. At working condition, the SAPHIRS chamber is kept at 10^{-4} mbar. The source-skimmer complex is set upon a translational stage, which moves along the three axes, to align itself to the second skimmer, placed at around 28 mm from the first one. The distance between the cluster source and the first skimmer was chosen as a compromise between the necessity of obtaining a molecular beam dense enough to produce observable clusters, and the one of having the source far enough to avoid clogging the skimmer with some deposited sample molecules. The second skimmer is aligned to the photon beam in the interaction chamber, from which it is placed at about 93 mm distance. The two beams cross each other in the interaction chamber in a perpendicular manner. Finally, the low vacuum present in the source chamber causes only a small pressure rise in the differential pumping stage (10^{-6} mbar), and only a negligible pressure rise in the spectrometer chamber (mid 10^{-8} mbar).

5 RESULTS AND DISCUSSION

ALL THE RESULTS WERE OBTAINED UNDER THE SUPERVISION OF DR. PATRICK ROUSSEAU. MOREOVER, THE DATA OBTAINED AT THE PLEIADES AND DESIRS BEAMLINES SAW ALSO THE SUPERVISION OF DR. ALEKSANDAR MILOSAVLJEVIĆ.

In this chapter, the results of the analysis of the data obtained with the different techniques employed here, namely photon and ion-induced mass spectrometry and XPS spectroscopy, are presented and discussed. As explained earlier, the scope of this work is the investigation of the effects of the hydration on the stability of the hypoxanthine molecule upon irradiation. A bottom-up approach is employed here to vary the number of molecules that are attached to hypoxanthine molecules and to study the resulting variation of their physico-chemical properties. In the case of the ion-induced mass spectrometry, we performed experiments starting from the isolated molecule, following with pure, and eventually hydrated, clusters in order to observe if the formation of non-covalent bonds can affect the stability of the molecular system upon irradiation. In the present XPS experiments, the characteristics of the isolated molecule had not been investigated, since the data obtained from Plekan *et al.*[33] were already available. Hence, the present experiments involved only pure and hydrated clusters, produced by means of the cluster source CELENO, which had been described earlier; the characterisation of how the source parameters affect the cluster size and distribution will be the subject of the first results to be discussed.

5.1 SAMPLES

The sample employed in all of our experiments is the hypoxanthine powder purchased from Sigma Aldrich at 99% purity. No further purification was performed on the sample prior to its utilisation for any of the presented experiments.

5.2 CLUSTER SOURCE CHARACTERISATION

The experiment performed at the DESIRS beamline allowed us to characterize the CELENO cluster source and provided us with information regarding the fine-tuning and regulation of the cluster source in order to produce clusters presenting different characteristics. In this section, we will discuss how the regulation of the oven temperature can affect the distribution of the cluster sizes, and how we managed to variate the hydration level of the hydrated clusters.

As mentioned in the previous chapter, while describing the design of the CELENO source, the parameters controlling the cluster size distribution are the He buffer gas flow (He_{flow}) and the associated pressure (He_p) inside the condensation channel of the cluster source, as well as the vapour pressure of hypoxanthine that is controlled by the oven temperature (T_{oven}), and the condensation channel temperature (T_{cc})[44]. During the experiments, we kept the temperature T_{cc} constant at the LN_2 temperature, while tuning the parameters He_{flow} and T_{oven}. However, it should be noted that these parameters are not independent. Indeed, by increasing the He flow, the number of collisions with the oven walls increases, leading the oven to cool down. Therefore, a variation of the buffer gas flow always induces a variation of the oven temperature, which can be compensated for by adjusting the heating current if a constant T_{oven} is desired. In the context of the present work, only the data concerning the variation of the oven temperature are shown. This choice was made to ensure a certain parameter consistency between the data obtained for the pure clusters and for the hydrated ones. In fact, both sets of data shown in this work have been collected at the same photon energy of 9.5 eV and with the same He_{flow} of 180 mL/min.

For collecting the cluster growth mass spectra at different oven temperatures and at different hydration levels, the photon energy was 9.5 eV. This choice was made because, according to literature, the ionisation energy of the hypoxanthine monomer is 8.85 eV[32], well below 9.5 eV.

5.2.1 REGULATION OF THE CLUSTER GROWTH THANKS TO THE OVEN TEMPERATURE VARIATION

The following discussion on the variations of the cluster size distribution relative to the temperature of the oven is based only on the data collected for pure clusters of hypoxanthine.

The presented results have been obtained at the DESIRS beamline, thanks to the coupling of the cluster source to the SAPHIRS end-station. We collected the mass spectra of the pure and hydrated clusters at the photon energy of 9.5 eV. The spectra were collected by defining the region of interest (ROI) within the data. In the case of the pure cluster spectrum shown in Figure 21, panel a), the data collection was stopped at m/z = 1580, while the acquisition was performed up to m/z = 3000 for the other two spectra (panels b) and c)). The extension of the acquisition region was performed after the acquisition of the first spectrum, where the signal coming from the bigger clusters was intense enough to encourage enlargement of the ROI for the next data acquisitions.

The possibility of having a low noise level in the collection of the mass spectra enables us to finely adjust the cluster source parameters while clearly seeing the effects of these tunings on the obtained mass spectra. For this reason, the data collected during this experiment were chosen for the characterisation of the CELENO cluster source.

The ROI-filtered VUV mass spectra recorded at the photon energy of 9.5 eV for the pure clusters growth are shown in Figure 21 at different cluster source conditions. The general distribution of the cluster sizes follows a log-normal trend, and its maximum and width depend on the cluster source parameters. The observed clusters correspond mostly to ionised cationic species $(Hyp)_n^+$. However, the low contribution from the expected isotopic contribution due to ^{13}C in larger clusters cannot explain the high intensity of $(Hyp_n+1)^+$ peaks in the mass spectra, starting from the dimer, as shown in the Figure 22. This suggests that protonated clusters are also

present. The protonated clusters are products of partial dissociation of larger clusters following photoionisation.

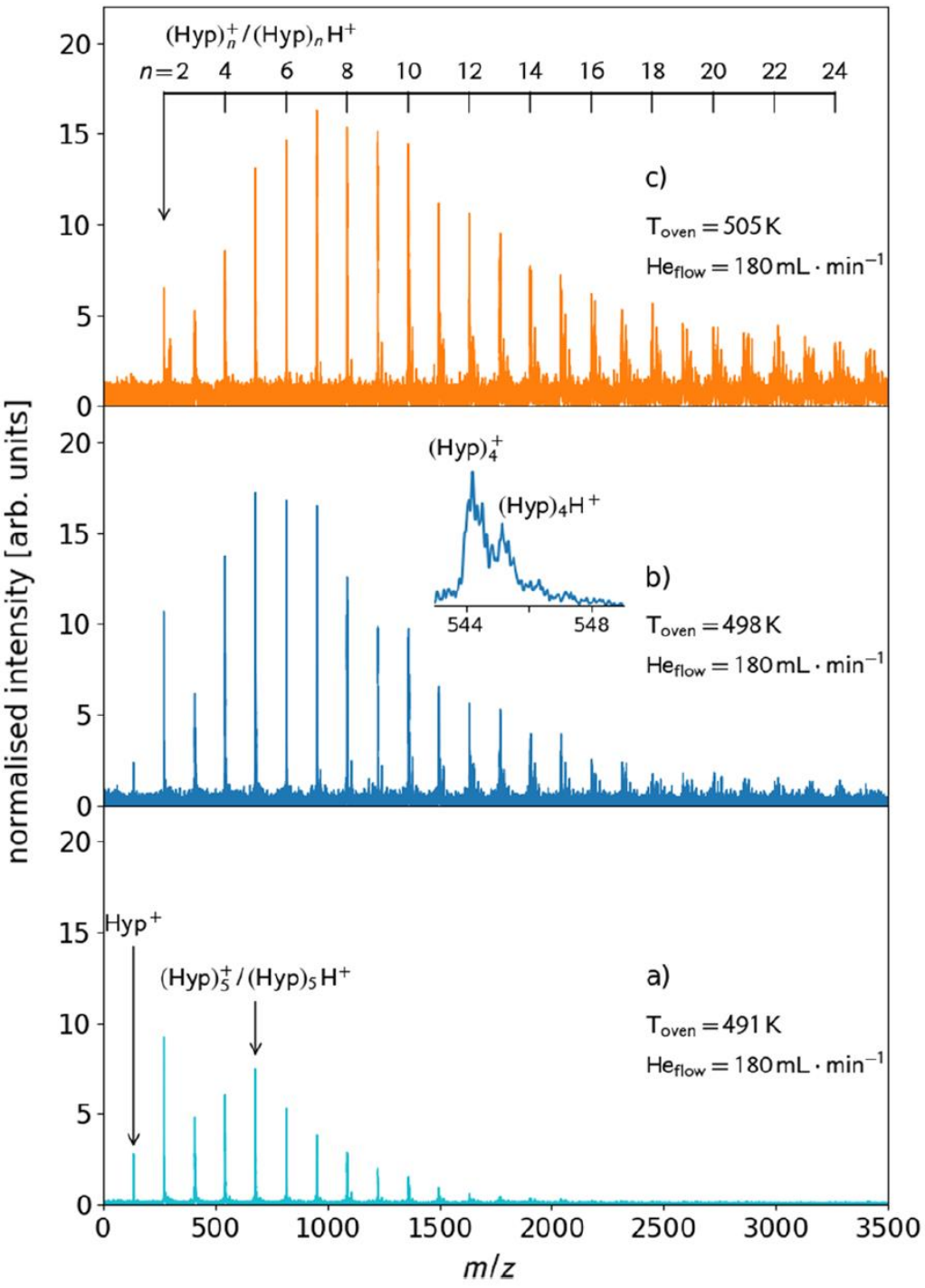

FIGURE 21: COMPARISON OF HYPOXANTHINE CLUSTER MASS SPECTRA OBTAINED AT DIFFERENT OVEN TEMPERATURES OBTAINED AFTER PHOTOIONIZATION AT 9.5 EV. IN PANEL A) THE TEMPERATURE IS THE LOWEST, AT 491 K; IN PANEL B) THE TEMPERATURE IS AT 498 K; AND IN C) IT IS 505 K. ALL THE SPECTRA WERE ACQUIRED WITH THE SAME HE GAS FLOW. (FROM OUR PUBLISHED WORK[77]).

Additional experiments performed with a photon energy of 12.1 eV, i.e. with overall higher internal energy following ionisation, indicated a much more pronounced observation of the protonated species. Unfortunately, due to technical problems, we had not been able to run these spectra for enough long time to obtain data with enough statistics to be presented here. Dissociation of H-bonded clusters via a proton transfer is indeed an efficient way to dissipate energy. In the case of mixed clusters of inert gas and H-bonded water molecules, the release of the inert gas atoms can lead to the formation of radical cationic clusters of water, as well as to the formation of both deprotonated and protonated clusters[69]. Therefore, the observation of protonated species is usually associated with cluster dissociation. Nevertheless, as the protonation signal is rather weak for a photon energy of 9.5 eV and as the observed size distribution follows a log-normal trend, we assume that the fragmentation of the cluster is mostly quenched, and thus, that the observed size distribution reflects quite well the initial size distribution in the current ionisation conditions. It is worth noticing that the detection efficiency of larger clusters is somewhat reduced due the mass dependence of the microchannel plate efficiency in this mass range (see Experimental details); therefore, the real size distribution is slightly shifted towards larger sizes.

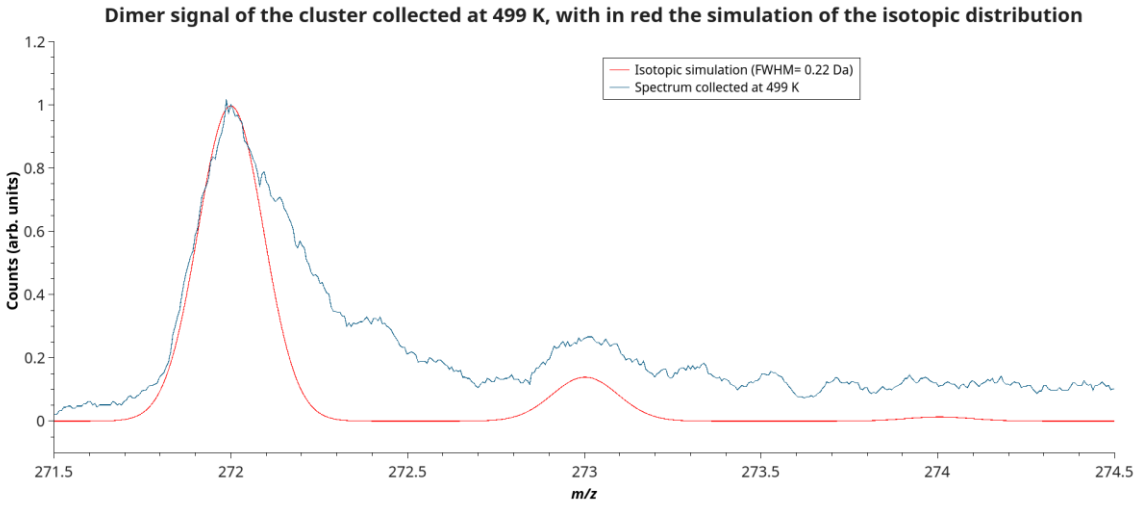

FIGURE 22: ZOOM ON THE DIMER SIGNAL COLLECTED AT 499 K, WITH, IN RED THE SIMULATION OF THE ISOTOPIC DISTRIBUTION (GAUSSIAN CONVOLUTION, FWHM = 0.22 U).

Moreover, Figure 22 shows the presence of a delayed fragmentation of the dimer in case of the mass spectrum collected at 499 K. It is characterised by the existence of an asymmetric tail at the dimer peak, on the higher m/z side. This feature can be attributed to the fact that metastable species are formed in the extraction zone. Moreover, Figure 22 provides a comparison of the expected isotopic distribution of the dimer with the measured one. First, this comparison enlightens the presence of a delayed-fragmentation contribution to the peak at 272 u, as the symmetrical calculated peak superposed on the experimental one makes it clear that this latter peak is asymmetric. The presence of a delayed fragmentation has been observed only for the dimer and trimer of the analysed spectra. Second, this comparison confirms that the isotopic C presence may contribute to the secondary peak at 273 u. Here, we notice that the intensity of the experimental peak at 273 u appears higher than that of the calculated one. However, this could be due to the noise coming from the signal, rather than the intrinsic higher intensity of the m/z = 273 peak. The isotopic calculation has been performed thank to the Xcalibur software, with a FWHM of the peak at 272 u of 0.22 u. Lastly, a general observation of the mass spectra also evidences secondary peaks shifted by 18 u (or multiples). This could be attributed to the attachment of water molecules from the background gas and/or to the thermal reactivity of the hypoxanthine molecule in the oven. In fact, as it can be seen from Figure 21, with the temperature variation the intensity of these secondary peaks variates a little, becoming more intense as the oven reaches higher temperatures.

We now consider the variation of the cluster distribution with the CELENO source parameters. In Figure 21 a), the source parameters were 491 K for the oven temperature and 180 mL/min for the buffer gas flow. The log-normal distribution has a maximum corresponding to the pentamer (m/z = 680), and the observed maximal cluster size corresponds to $n \sim 11$ molecules. The signals associated with the hypoxanthine molecule and with its dimer are rather intense in these source conditions. However, their relative intensities decrease when increasing the oven temperature from

491 K to 498 K (Figure 21 b) and to 505 K (Figure 21 c). The monomer is not visible in the mass spectrum recorded at the latter temperature. In fact, as clusters are growing by addition of monomers and dimers, the free monomers and dimers observed at lower temperature are aggregating with larger species at higher temperature due to an increased density of material to form clusters. Considering the Clausius–Clapeyron equation and thermochemical properties of hypoxanthine[70], the vapour pressures at 491 K and 499 K correspond, respectively, to about 33% and 58% of the one at the temperature of 505 K. Accordingly, by keeping the He_{flow} constant and increasing the oven temperature to 499 K, we can observe that the distribution reaches its plateau between the pentamer and octamer. It then slowly decreases down to the undecamer, after which the cluster signals become too feeble to be really appreciated. In the spectra collected at 491 K and 499 K, the dimer signal represents a strong peak (if not the strongest at 491 K), signifying that the dimer can be considered as highly stable, thus representing a so-called magic number (n = 2). In Figure 21 c) where the oven temperature has been increased to 505 K, we clearly notice a further shift of the cluster size distribution towards higher m/z. The log-normal distribution has now a flat maximum between the hexamer (m/z = 816) and the decamer (m/z = 1360) and presents higher relative intensities for larger cluster sizes, up to m/z ~ 3000.

To conclude, a small variation of the oven temperature drastically affects the cluster size distributions as the vapour pressure strongly depends on the temperature in the range considered in this work[44,53,54]. The size distribution can be controlled by carefully setting the gas aggregation source parameters, as shown previously[44,53,54].

5.2.2 REGULATION OF THE HYDRATION LEVEL OF THE HYDRATED CLUSTERS

We will now briefly discuss how to use the CELENO cluster source to regulate the hydration level of the hydrated hypoxanthine clusters.

As described in the previous chapter, the production of hydrated clusters relies on a Nafion® membrane. The inert gas flowing inside the Nafion®

tube presents a humidification degree depending on the surface of the tube immersed in water. Thus, the regulation of the hydration level of the clusters is possible thanks to the variation of the surface of the Nafion® tube in contact with liquid water. Figure 23 shows two mass spectra recorded with different levels of humidification of the buffer gas. To observe how the level of humidification affects the cluster formation and size distribution, we set the photon energy of the DESIRS beamline at 9.5 eV (the same used for collecting data with the pure clusters at different oven temperatures, see previous paragraph) and we selected a region of interest limited to 1000 u (after calibration). First, we consider the mass spectrum collected with the Nafion® tube submerged in ultra-pure water, as displayed in top panel a) of Figure 23. Here, up to two water molecules are attached to the monomer. Starting from the dimer (m/z = 272), we clearly observe in the mass spectrum that the hydration level goes up to nine added water molecules. We also perceive, although with a very weak intensity, a tenth and eleventh molecule being added, which become more and more evident starting from the trimer. When submerging the Nafion® tube, the relative intensity of the hydrated species compared to the pure clusters increases with the number of hypoxanthine molecules, as does the maximum number of water molecules attached to a given hypoxanthine cluster. From the hexamer, the intensity of the signal of the pure hypoxanthine cluster becomes similar to the one of the hydrated clusters. This makes an accurate description more complex, as mass peaks start to overlap with each other. On the other hand, when the Nafion® tube was just touching the water surface (bottom panel), we could see that only one water molecule could be added to the monomer. The level of hydration is reduced for all cluster sizes, for instance up to seven water molecules can be added to the dimer (compared to the eleven added molecules in the previous hydration conditions).

In conclusion, the hydration of the buffer gas through a Nafion® membrane is an efficient way to produce hydrated clusters. The level of hydration can be controlled by adjusting the surface of the membrane in contact with water.

From these two sets of data collected at DESIRS we can conclude that the CELENO cluster source can be finely tuned in order to produce different cluster distributions, thanks to the variation of a few parameters, namely the oven temperature, and the area of the Nafion in contact with the water. We have been able to observe the rise of big clusters.

In the next paragraph, the ion-induced fragmentation of the isolated hypoxanthine molecule and its clusters will be presented and discussed.

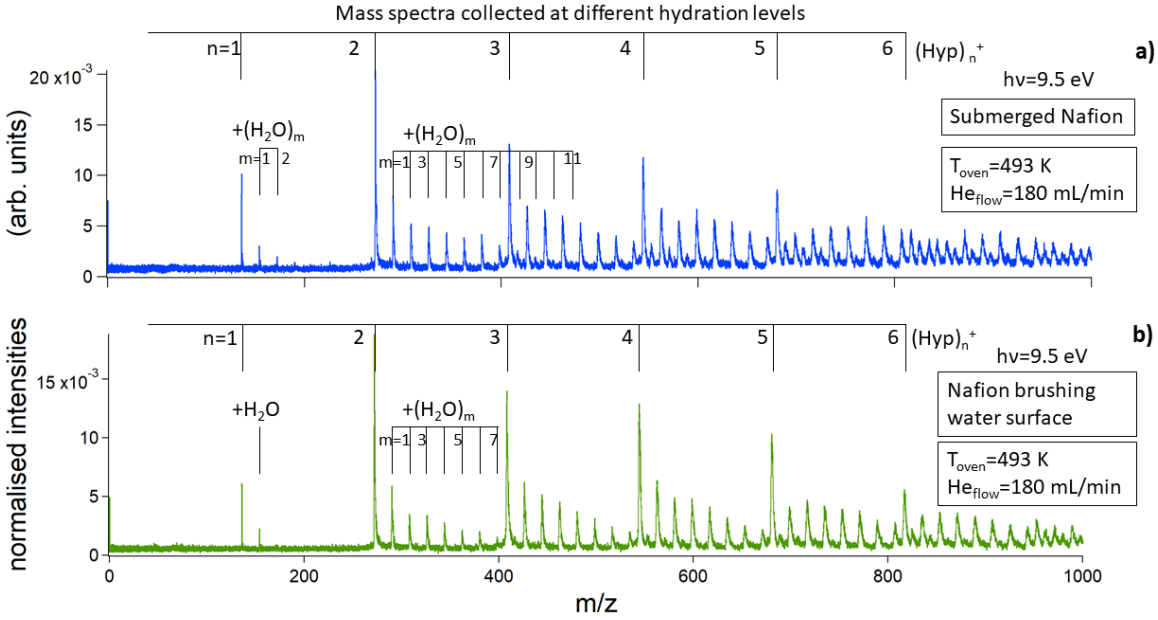

FIGURE 23: COMPARISON OF THE LEVEL OF HYDRATION REGULATED BY THE AREA OF NAFION® IN CONTACT WITH WATER. IN PANEL A) THE NAFION® IS SUBMERGED, B) IT IS JUST BRUSHING THE WATER SURFACE.

5.3 STUDY ON THE STABILITY OF THE HYPOXANTHINE MOLECULE AND ITS CLUSTERS UPON ION COLLISION

The first data sets to be analysed, and consequently interpreted, are the one coming from the ion-induced dissociation experiments performed with the COLIMACON setup. From this analysis, we can understand the molecular stability upon irradiation by oxygen ions. Here, the approach is different to what was performed when analysing the cluster source characteristics, where we employed VUV photons to induce mostly non-

dissociative ionization. By employing different kinds of projectiles, we get different excitation conditions, which can lead to different fragmentation processes.

The ion projectile employed in all the following experiments is O^{6+} at 90 keV. The choice fell on oxygen because of its natural gaseous form and its easy availability. Also, the multiple charge of the oxygen ion guarantees the production of multiply ionised species from the target, while the energy chosen is the best suited for observing, as a main phenomenon, the electron capture.

Following the method of increasing the complexity of the studied system in order to better understand it, we begin with the presentation of the results obtained for the isolated molecule, then going up with the pure clusters and ending with the hydrated ones.

In the next section, we will detail the fragmentation mechanisms of isolated hypoxanthine based on the analysis of the coincidence map.

5.3.1 ION-INDUCED FRAGMENTATION PATHWAYS

5.3.1.1 DISSOCIATION OF THE ISOLATED HYPOXANTHINE MOLECULE

The isolated hypoxanthine mass spectrum was obtained upon the interaction of a molecular beam, produced by heating the hypoxanthine powder in the source oven at 460 K, with O^{6+} at 90 keV. This spectrum presents some interesting characteristics (Figure 24). First, we can notice a strong molecular stability, as the predominant peak at m/z = 136 corresponds to the intact hypoxanthine cation Hyp^+. The second feature concerns the main molecular fragmentation patterns. There are two major consecutive ways in which hypoxanthine can fragment. In the first one, we can recognise an initial loss of CHN, giving the fragment $(Hyp\text{-}CHN)^+$ at m/z = 109, which then evolves into $(Hyp\text{-}C_2H_3N_2)^+$ at m/z = 81 and to $(Hyp\text{-}C_3H_4N_3)^+$ at m/z = 54. This sequential CHN loss behaviour is similar

to the case of adenine under comparable conditions[9]. The other fragmentation pattern is characterised by an initial loss of CO; with a peak at m/z = 108 representing the $(Hyp\text{-}CO)^+$ fragment. This fragmentation progresses further with a loss of CHN, $(Hyp\text{-}C_2HNO)^+$, at m/z = 81, point shared with the other main pattern, and ends with two peaks: one at m/z = 54 representing $(Hyp\text{-}C_3H_2N_2O)^+$, and the second at m/z = 53 $(Hyp\text{-}C_3H_3N_2O)^+$. This last process, involving the oxygen loss, is analogous to the one that the guanine molecules undergo when fragmenting[23].

Moreover, we could compare our results to the ones obtained for the same molecule by Feyer *et al.*[32], using the PEPICO technique, and Dawley *et al.*[31], using electron impact mass spectrometry. Our findings are analogous with those of both of these works. This led us to infer the way in which the fragmentation dynamics takes place, according to their results. The diagram of the Figure 25 summarises the different fragmentation pathways we identified.

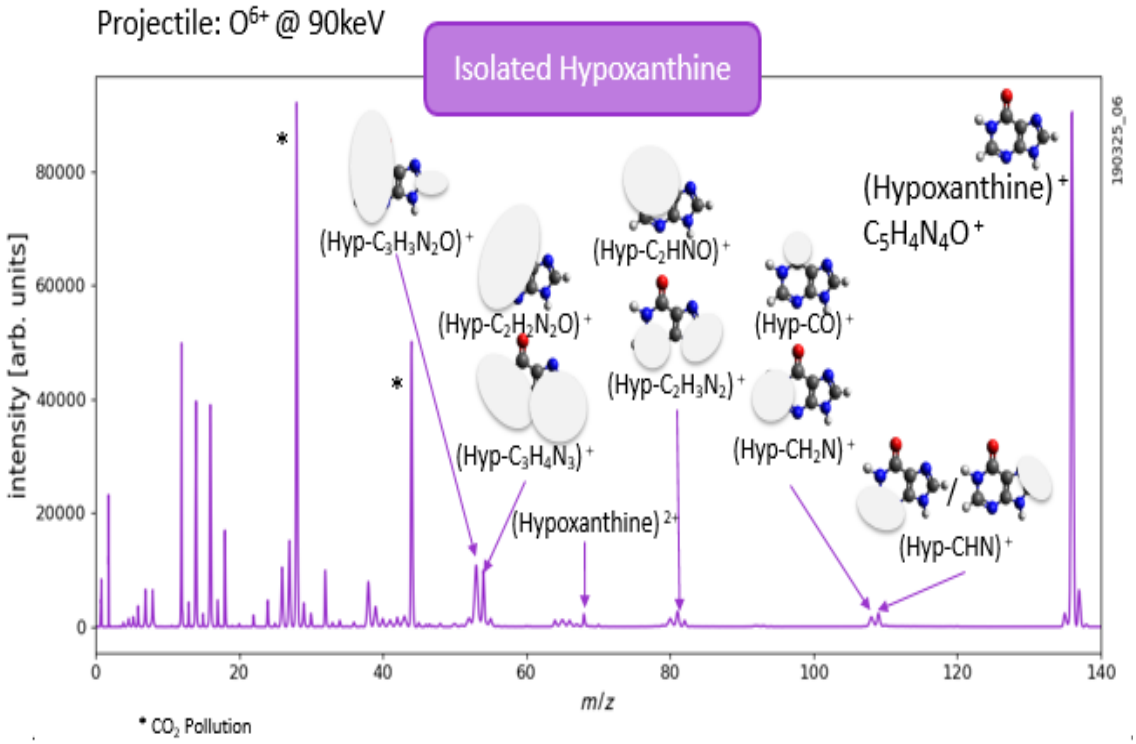

FIGURE 24: MASS SPECTRUM OF ISOLATED HYPOXANTHINE UPON COLLISION WITH AN O^{6+} PROJECTILE AT 90 KEV.

The intensity of the fragment at m/z = 28 (CO^+ or CH_2N^+) is partly due to the fragmentation of hypoxanthine but also to the ionisation and fragmentation of CO_2 from the residual gas in the interaction chamber, as indicated by the presence of CO_2^+ at m/z = 44.

Lastly, unlike what was observed in literature for the isolated adenine in the experiment performed by Domaracka *et al.*[9], which also employed a multiply charged oxygen beam, or the one performed by Alvarado *et al.*[29] involving various ion beams, we observed a peak corresponding to the intact doubly ionized hypoxanthine at m/z = 68. These results encouraged us to explore the coincident map for the hypoxanthine dication fragmentation. These results will be discussed further along this chapter.

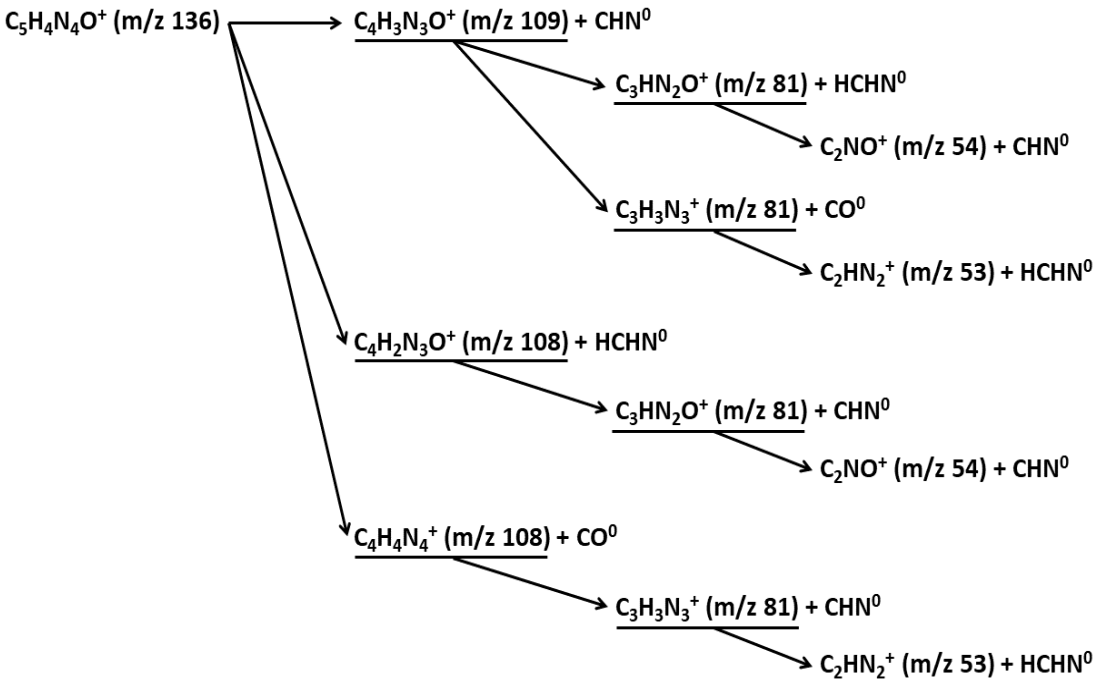

FIGURE 25: ISOLATED HYPOXANTHINE FRAGMENTATION PATHWAYS UPON THE COLLISION WITH AN O^{6+} PROJECTILE 90 KEV.

5.3.1.2 DISSOCIATION OF PURE AND HYDRATED HYPOXANTHINE CLUSTERS

Following the acquisition of the isolated molecule mass spectra, we proceeded on performing the experiments on both pure and hydrated clusters. The parameters for the formation of pure clusters were 516 K for the temperature of the oven, with the flow of He being of 160 mL/min. For the hydrated hypoxanthine clusters, the oven was set at 508 K, with a He_{flow} of 180 mL/min, and the Nafion® tube being submerged by water. From the cluster fragmentation spectra of the pure and hydrated hypoxanthine clusters, depicted in Figure 26 b) and c) respectively, we obtained information about how the H-bonds can influence the molecular fragmentation. The two spectra present the same new significant features, when compared to the isolated molecule. These spectra include fragments originating from the dissociation of the protonated molecule, as illustrated in Figure 27. The first new fragment encountered is of m/z = 119, resulting from the loss of H_2O, referred to as $[Hyp]H^+$-H_2O and corresponding to the formula $C_5H_3N_4^+$. This particular fragmentation channel has already been observed in other nucleobases, such as uracil[71]. The following fragment at m/z = 109 shows the loss of CO from the protonated hypoxanthine molecule and corresponds to the molecular ion $[C_4H_4N_4 + H]^+$. A next fragment is found at m/z = 94 and is described by the formula $C_4H_2N_2O^+$. It is followed by $C_4H_3N_3^+$ at m/z = 93, and by $C_3H_2N_2O^+$ (or $C_3H_4N_3^+$) at m/z = 82 with its complementary fragment $[C_2H_2N_2 + H]^+$ (or C_2HNO^+) at m/z = 55. The identification of these fragments as originating from the protonated hypoxanthine is in accordance with the data retrieved from the Japanese Mass Bank[72].

The fragments ejected from the clusters appear to be the result of different fragmentation channels, as illustrated in Figure 27. The presence of the fragment of m/z = 119 can be interpreted as an indication of the localisation of the protonation taking place most favourably on the oxygen atom, showing also a proton transfer from the close –NH group in

position 1, thus allowing the loss of H_2O from the protonated molecule. A more probable dissociation channel is the loss of the CO molecule from a protonated molecule, i.e. the loss of the C atom in position 6 with the O atom bound to it, forming the fragment of $m/z = 109$. Another fragmentation channel consists in the loss of the atom right adjacent to the oxygen, namely the carbon in position 6, and the loss of the nitrogen in position 1 and of the hydrogen bound to it, thus forming the fragment of $m/z = 93$. The separation of the protonated imidazole leads to the fragment consisting in the pyrimidine ring of $m/z = 94$. In this case, it is probable that the protonation takes place at the nitrogen in position 7. Lastly, cleavage of the double bound between the C atoms in positions 4 and 5 may lead to the formation of fragments of $m/z = 82$ and 55 (Figure 27).

A fragment that would have been interesting to observe would have been the entire hypoxanthine with a fragment coming from the other molecule non-covalently bound to it. But, this kind of fragment is not easy to detect, due to the fact that the weak hydrogen bond would likely be broken after ionisation.

Lastly, when observing the hydrated molecule fragmentation spectrum, we did not observe any hydrated fragment. This indicates that the hydration level of this experiment was low, as it will be further confirmed by the observation of the hydrated cluster growth. The extended mass spectra for the pure and hydrated hypoxanthine are shown and discussed in the next paragraphs.

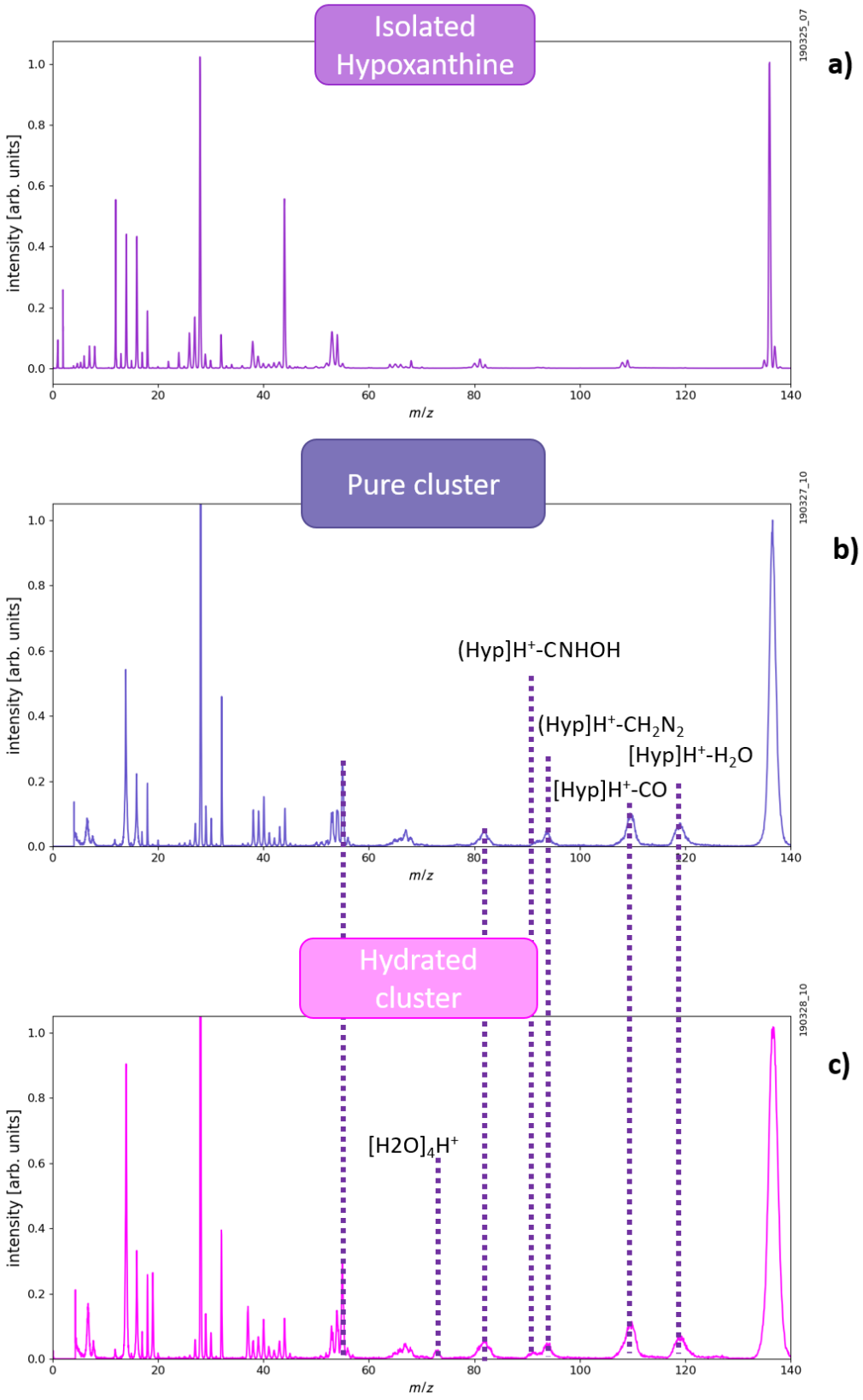

FIGURE 26: COMPARISON OF THE FRAGMENTATION SPECTRA OF A) THE ISOLATED HYPOXANTHINE MOLECULE, B) THE PURE HYPOXANTHINE CLUSTERS, AND C) THE HYDRATED HYPOXANTHINE CLUSTERS UPON COLLISION WITH AN O^{6+} PROJECTILE AT 90 KEV.

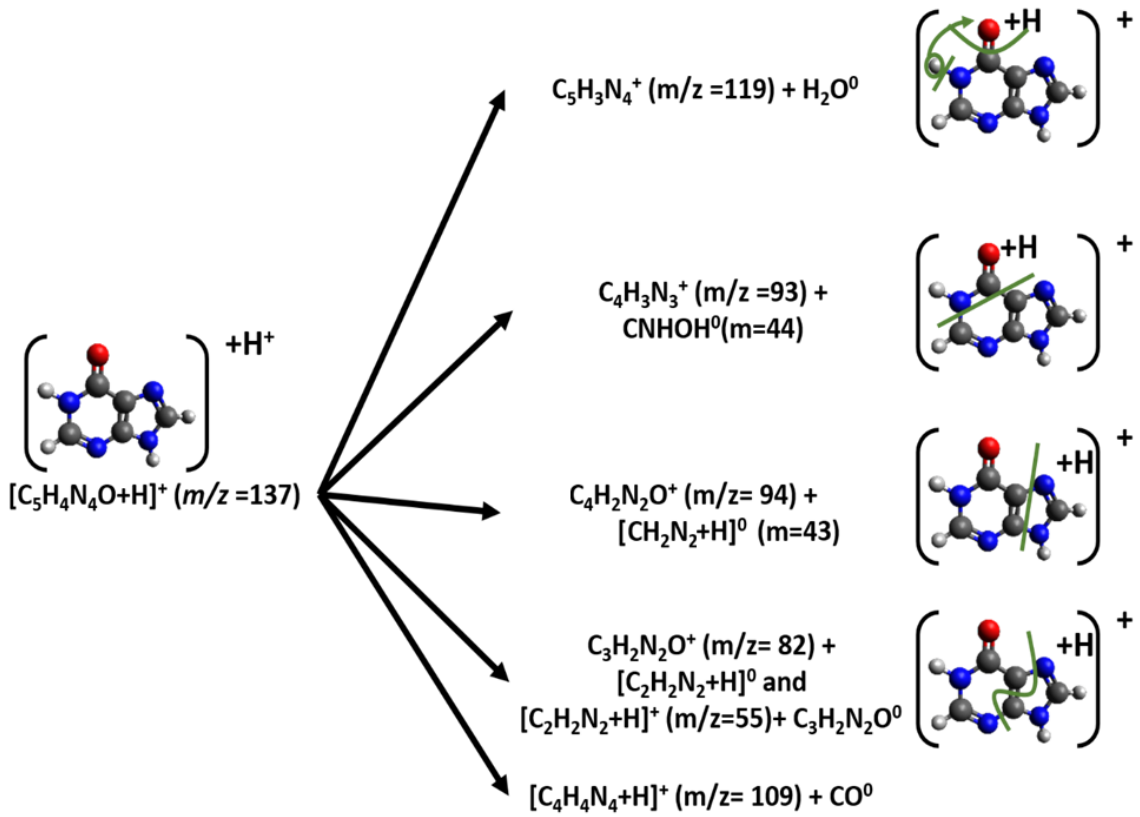

FIGURE 27: THE FRAGMENTATION CHANNELS OBSERVED FOR BOTH THE PURE AND HYDRATED CLUSTERS.

5.3.2 EXTENDED MASS SPECTRA FOR CLUSTERS

5.3.2.1 PURE CLUSTER FORMATION

In the pure hypoxanthine cluster extended mass spectrum, we can observe clusters up to 7 molecules, but up to 5 with good resolution. Moreover, we can observe doubly charged clusters from 11 molecules, as seen in Figure 28. We also observe that the main peak is still represented by the monomer, with a steep harmonic decrease of intensity starting from the dimer: already the heptamer presents a very low intensity, with the signal coming from the octamer being non-observable.

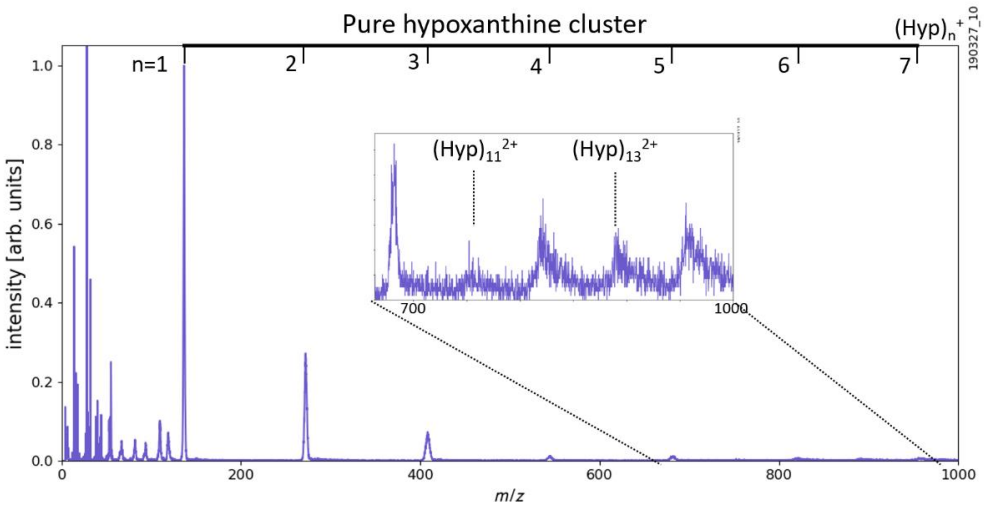

FIGURE 28: PURE HYPOXANTHINE CLUSTER MASS SPECTRUM, PERFORMED WITH AN O^{6+} PROJECTILE AT 90 KEV, AND DISPLAYING THE CLUSTER FORMATION.

5.3.2.2 HYDRATED CLUSTER FORMATION

In the hydrated hypoxanthine cluster extended mass spectrum, we can observe clusters up to 7 molecules, but up to 5 with good resolution (see Figure 29). Moreover, we can observe doubly charged clusters from 11 molecules. For the monomer, dimer, and trimer we can see each water molecule being added, up to 6 molecules. Observing the clusters formed by more than three hypoxanthine molecules, we are not able to observe distinctly the addition of the water molecules, if any attached to the cluster. While the submerged Nafion® tube and cluster source parameters are comparable to the ones used at the DESIRS beamline in the previous section, these observations are in strong contrast with the photoabsorption case (Figure 23). In particular, only up to 2 water molecules were found to be attached to the monomer after photoionization at 9.5 eV. Therefore, as suggested in the case of hydrated adenine cluster[9], the cluster distribution observed in the ion-induced dissociation case suggests that fragmentation of large clusters leads to the formation of fully hydrated monomers of hypoxanthine. As it was shown in Figure 23 that up to 7 water molecules can be attached to large hypoxanthine clusters, this means that the whole water network can survive the dissociation of the hydrated clusters. A similar behaviour has been also observed in the case of the photoionization

of hydrated leucine-enkephalin dimers, [leu-enk + 3(H_2O) + H]$^+$, where the yield of fully hydrated monomer was found to be 8 times higher than its dehydrated counterpart[73].

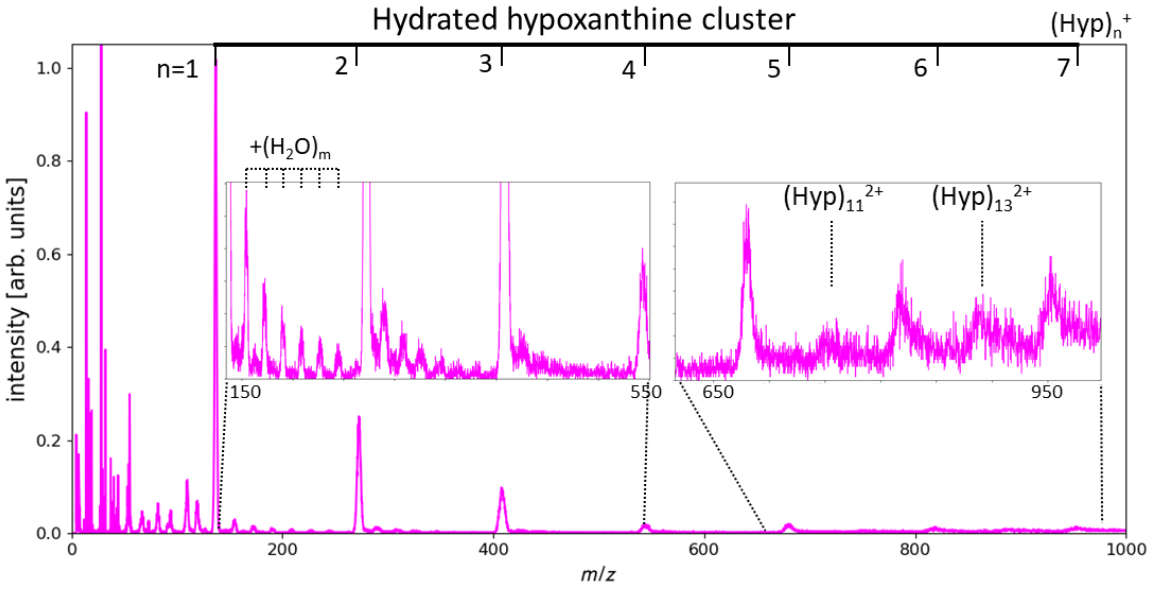

FIGURE 29: HYDRATED HYPOXANTHINE CLUSTER MASS SPECTRUM, PERFORMED WITH AN O^{6+} PROJECTILE AT 90 KEV, AND DISPLAYING THE CLUSTER FORMATION.

5.3.3 DICATION COINCIDENCE MAP (HOW DOES IT BREAK)

The coincidence map for the isolated hypoxanthine shows interesting patterns, with specific breaking points (Figure 30 and Figure 31). In fact, one of the fragments that we encounter most often is the one with m/z = 28, namely, either CO^+ or CH_2N^+. Another quite common fragment that was encountered is the ion CHN^+, with m/z = 27. Lastly, the fragments corresponding to $CHNO^+$ (m/z = 43) and $CHNOH^+$ (m/z = 44) are also among the most common fragments. Another interesting fact about the coincidence map presented here, is that it presents similarities with the one obtained for adenine by Moretto-Capelle[30], employing a 100 keV proton beam, and the one by Alvarado[29] using various projectiles (H+ and H^0, He^+ and He^0, and C^+ and C^0), all at 14 keV. In fact, in both

studies, the authors have identified four main fragmentation pathways, described as follows:

- 135^{2+} -> 28^{+} + 107^{+}
- 135^{2+} -> 43^{+} + 92^{+}
- 135^{2+} -> 28^{+} + 80^{+} + 27^{0}
- 135^{2+} -> 28^{+} + 53^{+} + 54^{0}

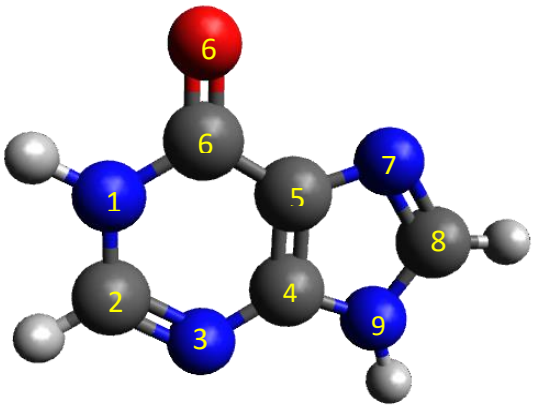

FIGURE 30: HYPOXANTHINE MOLECULE, WITH ITS ATOMS NUMBERED.

This last neutral fragment 54^{0} is obtained after a hydrogen transfer. Applied to hypoxanthine, with a mass being of one unit heavier than adenine, these fragmentation pathways may become:

- 136^{2+} -> 28^{+} + 108^{+}
- 136^{2+} -> 44^{+} + 92^{+}
- 136^{2+} -> 28^{+} + 81^{+} + 27^{0}
- 136^{2+} -> 28^{+} + 53^{+} + 55^{0}

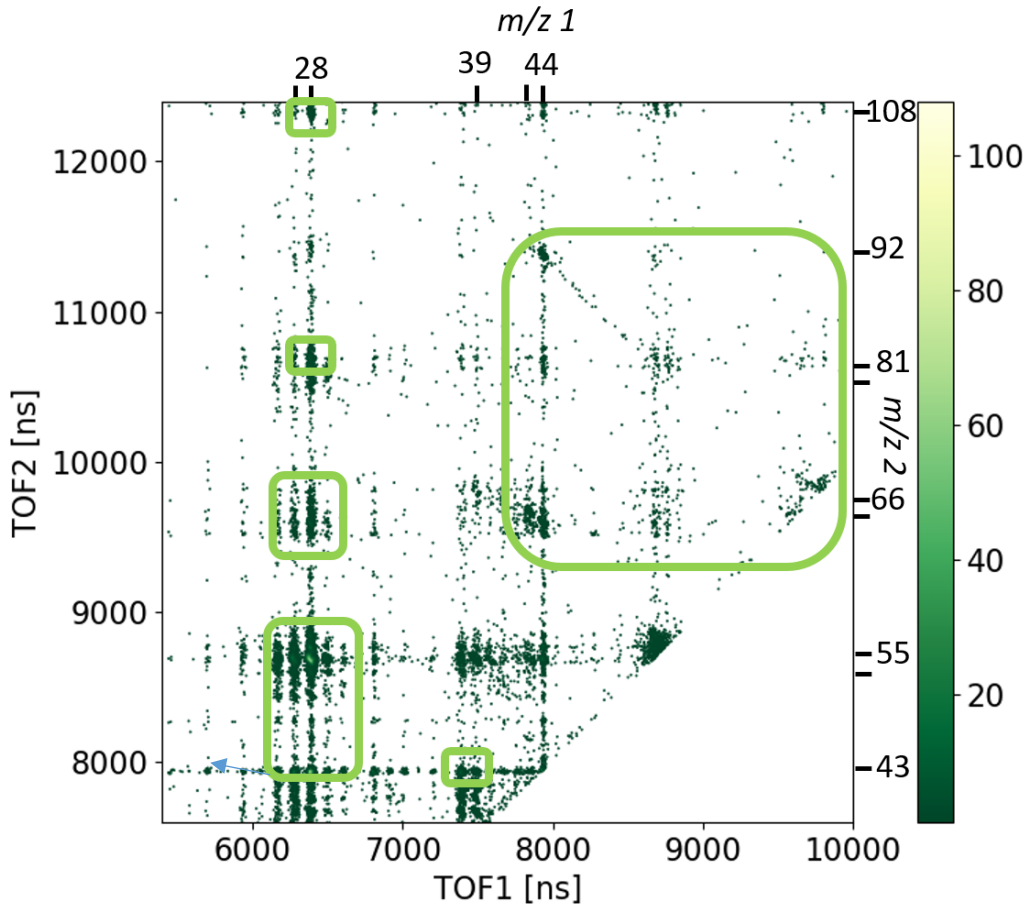

FIGURE 31: COINCIDENCE MAP OF THE FRAGMENTATION OF THE ISOLATED HYPOXANTHINE DICATION FORMED AFTER THE COLLISION WITH O^{6+} PROJECTILE AT 90 KEV. THE COINCIDENCE MAP IS ZOOMED ON THE AREA WHERE THE COINCIDENCE ISLANDS TAKEN INTO CONSIDERATION ARE GROUPED. THE ANALYSED COINCIDENCE ISLANDS ARE CIRCLED IN LIGHT GREEN.

As shown in the following section, these fragmentation pathways are indeed observed for the case of the hypoxanthine dication. The first coincidence islands to be discussed in this work are the ones in common with the adenine dication fragmentation pattern. After considering these islands, and having discussed if the processes involved for the two molecules are comparable, we will then move on to the analysis of a few other relevant coincidence islands.

5.3.3.1.1 COINCIDENCE ISLAND OF THE FRAGMENTS 28^+ AND 108^+

In hypoxanthine, the island obtained from detection in coincidence of the ions of m/z = 28 and m/z = 108 represents the simple separation of two

ions without any neutral loss, thus corresponding to a two-body dissociation of the molecular dication. As a consequence, this coincidence island is expected to be characterized by a slope of -1. However, the statistics of the experimental data reported in Figure 32 is not good enough to confirm the slope of -1. This coincidence island has also the particularity of having a multiple attribution: both fragments CO^+ and $HCHN^+$ have a mass of 28. Unfortunately, with the present data it is not possible to assign this island specifically to one of the fragmentation channels.

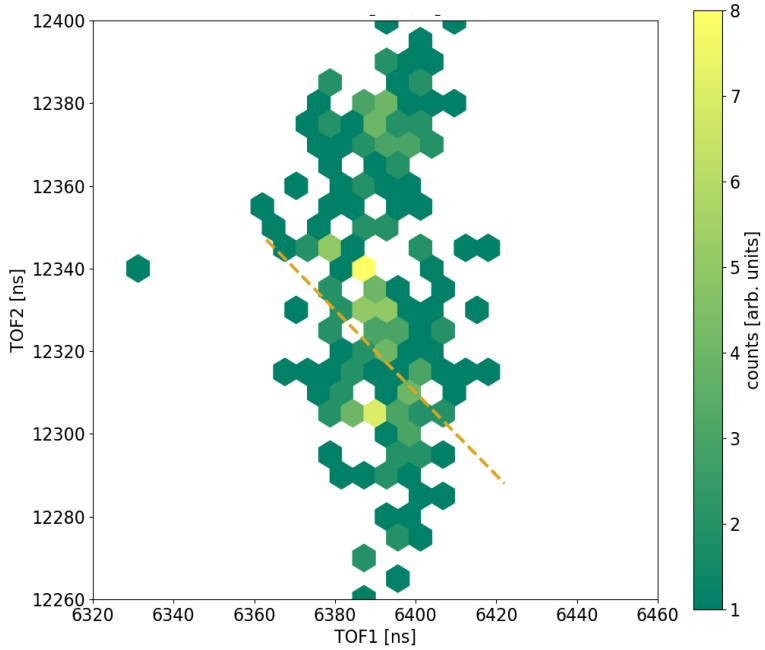

FIGURE 32: COINCIDENCE ISLAND OF THE FRAGMENTS 28^+ AND 108^+ FROM THE ISOLATED HYPOXANTHINE DICATION. IN GOLD THE SLOPE OF -1.

When considering the loss of $HCNH^+$, we also have to take into account that, before the fragmentation takes place, a double hydrogen transfer from either positions 1, 2 to 2, 3 or 8, 9 to 7, 8 can also lead to the formation of the fragments 28^+ and 108^+ (Figure 33). Moreover, the fragmentation pathways considered in Figure 33 take into account only one hypoxanthine tautomer; the one which was considered the most stable by Plekan *et al.*[33].

This fragmentation process can be described as follows:

- 136^{2+} -> 28^{+} + 108^{+}

When comparing this dication fragmentation channel with the analogous one described in the literature for adenine[29,30], we notice that there is a limited number of possible attributions for the $m/z = 28$ fragment. In adenine, according to the literature[30], there are only two eligible solutions for the production of this fragment: one is the HCNH which involves the C atom in position 8 and the N atom in position 9; while the other is the CNH_2 fragment involving the C atom in position 6. Hence, no hydrogen migration was invoked. However, looking at the adenine molecule, one possibility could be a double H-transfer from the positions 8 and 9 to 7 and 8, respectively, in analogy to the double H-transfer presently invoked in case of ion-induced fragmentation of hypoxanthine.

As we can see on Figure 33, the attribution of the different fragments seems a much more challenging task in the case of hypoxanthine, a task that could be managed with the help of theoretical calculations or, partially, with the use of deuterium. As illustrated in Figure 33, five different fragmentation channels may be invoked for the formation of the fragments 28^{+} and 108^{+} from the isolated hypoxanthine dication. Two of these channels imply hydrogen transfers.

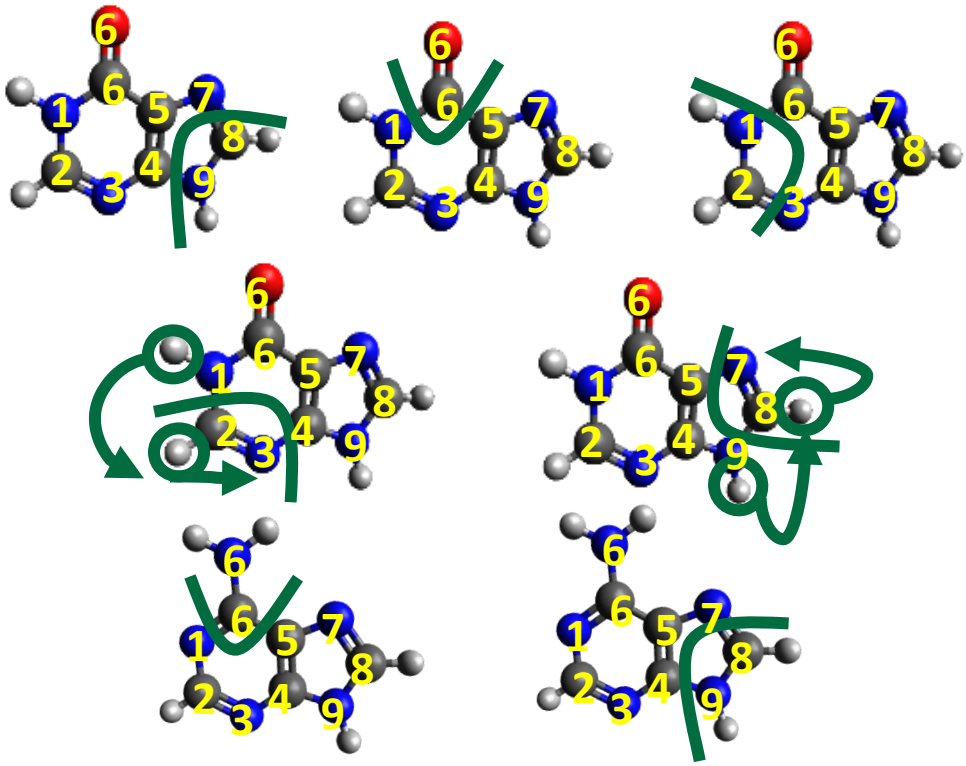

FIGURE 33: TOP: THE POSSIBLE CLEAVAGES PRODUCING THE TWO FRAGMENTS OF m/z = 28+ AND 108+. BOTTOM: THE TWO OPTIONS FOR THE ADENINE m/z = 28+ FRAGMENT AS PROPOSED IN LITERATURE. CLEAVAGES LEADING AN IONIC FRAGMENT ARE DEPICTED WITH THE GREEN LINES. PROTON TRANSFERS ARE INDICATED BY MEANS OF GREEN ARROWS.

5.3.3.1.2 COINCIDENCE ISLAND OF THE FRAGMENTS 28^+, 81^+ AND 27^0

The next coincidence island represents the dissociation of the dication into three fragments, two ions of m/z = 28 and 81 and a neutral fragment loss of mass equal to 27 u. As we can observe from the Figure 34 depicting this coincidence island, the slope of the island is not -1, thus the process does not take place in a single-step process, but rather in two subsequent steps. This fragmentation pathway looks rather different from the one shown for adenine in the work of Moretto-Capelle[30]. In that case, the fragmentation of adenine follows a different pathway: first, the adenine dication separates into two cations of m/z equal to 28 and 108; then, the latter fragment emits the neutral particle of mass equal to 27 u. As illustrated for adenine at the bottom part of Figure 35, the fragments are composed of the C in position

8 and N in position 9 for the fragment with m/z = 28 and the C in position 2 and N in position 3 for the neutral loss.

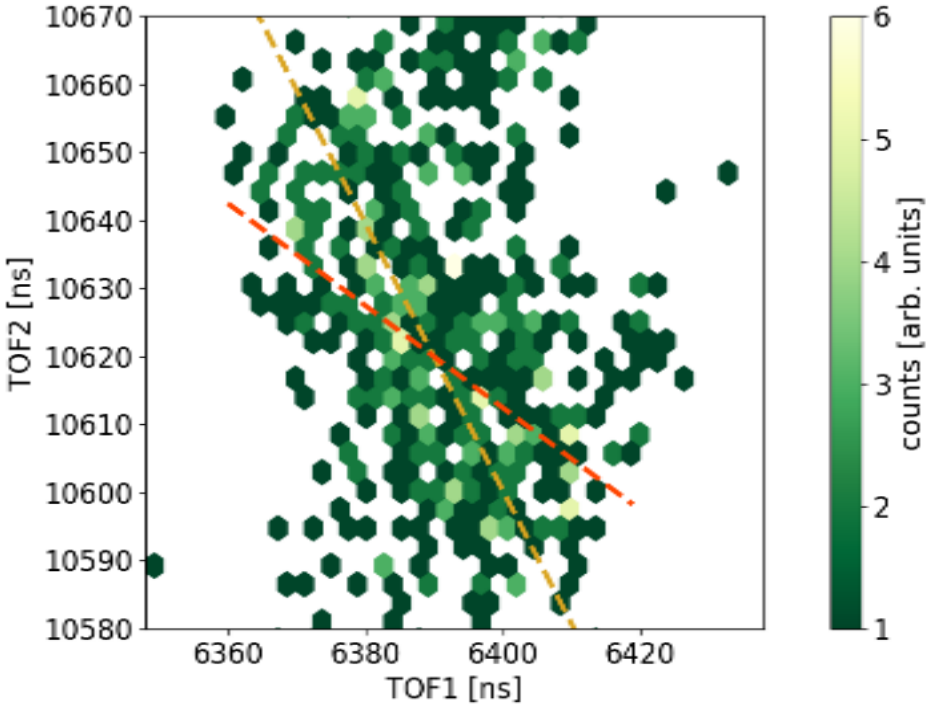

FIGURE 34: COINCIDENCE ISLAND OF THE FRAGMENTS 28^{+}, 81^{+} AND 27^{0} FROM THE ISOLATED HYPOXANTHINE DICATION. ON THE COINCIDENCE ISLAND, THE GOLD AND ORANGE LINES REPRESENT THE CALCULATED SLOPES FOR THE PROCESS OF FIRST LOSS OF THE M/Z = 81 FRAGMENT, IN GOLD, AND THE INITIAL LOSS OF THE FRAGMENT M/Z = 28, IN ORANGE.

By analysing the shape of the coincidence island presently obtained for hypoxanthine (Figure 34), we can assume that the process that predominantly takes place can be described as follows:

- 136^{2+} -> 55^{+} + 81^{+}
  -> 28^{+} + 81^{+} + 27^{0}

According to the formulae given in Chapter 3 (page 29), the expected island slope for this process is:

- Slope = $-55^{+}/28^{+}$ = -1.96.

The other possible process can be described as:

- 136^{2+} -> 28^{+} + 108^{+}
  -> 28^{+} + 81^{+} + 27^{0}

with its slope being:

- Slope = $-81^{+}/108^{+} = -0.75$.

As can be seen on Figure 34, the calculated slope, in gold, describing the first dissociation process, seems to be in good agreement with the general shape of the coincidence island. On the other hand, although the slope describing the second process, in orange, does not follow closely the island shape, the present statistic doesn't allows to discard this latter process totally. As depicted in Figure 35, four different dissociation channels can be invoked for the formation of the fragment ions 28^{+} and 81^{+}, together with the neutral fragment 27^{0}.

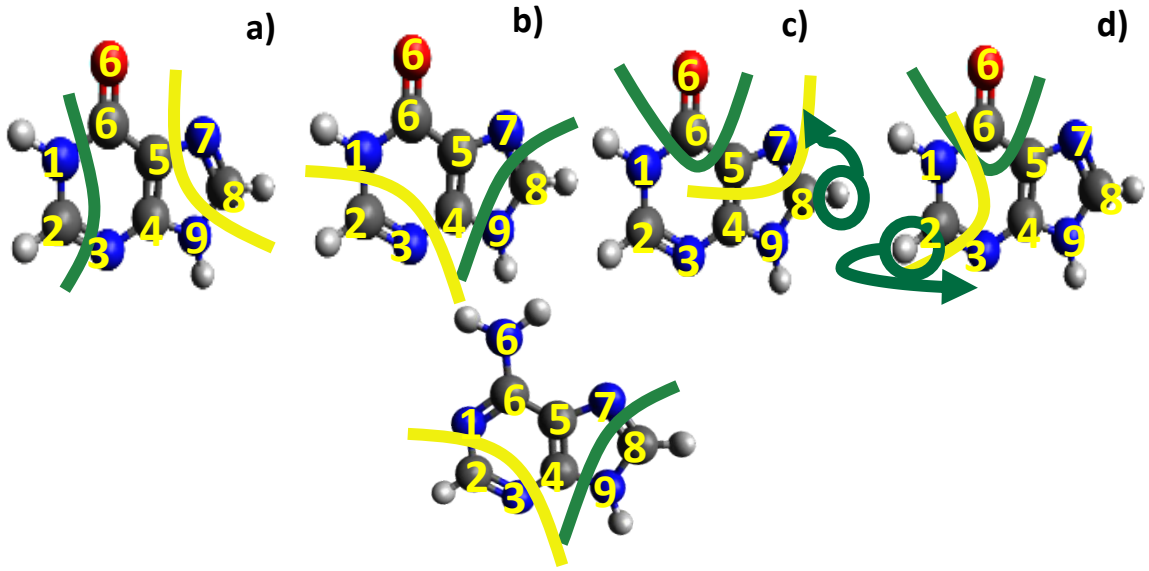

FIGURE 35 : TOP: CLEAVAGE MODELS FOR THE FORMATION OF THE FRAGMENTS OF $M/Z = 28^{+}$ AND 81^{+}, AS WELL AS THE LOSS OF THE NEUTRAL FRAGMENT OF MASS EQUAL TO 27 U. BOTTOM: THE ADENINE FRAGMENTS CORRESPONDING TO THE COINCIDENCE ISLAND OF FRAGMENTS 28^{+}, 80^{+} AND 27^{0}. CLEAVAGES LEADING TO AN IONIC FRAGMENT ARE DEPICTED WITH A GREEN LINE, WHILE CLEAVAGES LEADING TO A NEUTRAL FRAGMENT ARE SHOWN BY MEANS OF A YELLOW LINE. PROTON TRANSFERS ARE INDICATED BY MEANS OF GREEN ARROWS.

The models of Figure 35 show the different breaking sites for the formation of the observed fragments. The two pathways shown in panels a) and b) are similar to the ones proposed by Moretto-Capelle *et al.* for the

fragmentation of the adenine dication[30]. In their model, the slope of the island was smaller than -1 and the first step of the dissociation involved the formation of the fragment $HCHN^+$ (m/z = *28*) and subsequently the separation of the fragment of m/z = 80 from the neutral particle of 27 u. In the present situation, these two fragmentation pathways seem less favourable as they would correspond to the process involving a slope of – 0.75, which does not seem to follow closely the shape of the coincidence island. To determine the actual feasibility of these two pathways shown in panels a) and b) of Figure 35, some theoretical calculations should be performed.

The other two processes (Figure 35 c and d) include a hydrogen transfer and the fragment of m/z = 28 corresponding to CO^+. From comparison with the data from literature[30], it appears that one plausible process could be the one shown in Figure 35, panel c). In the first step of the fragmentation, this process implies the cleavage of two double bonds, which involve the double bonded carbons in positions 4 and 5 and the double bonded N and C atoms in positions 7 and 8. Prior to the second fragmentation step, the nitrogen in position 7 acquires the hydrogen from the carbon in position 8 (via hydrogen transfer), thus leading to the transient fragment $COCNH^+$ of m/z = 55. Then, the second fragmentation step involves the separation of CO^+ from CHN. Even if this process could take place, the energy needed to break simultaneously the two double bonds is quite high. Therefore, theoretical models are required to check if this process could be a favoured one. In the case of the process described by the Figure 35 d), the fragment of mass 55 is composed of the CO, the NH in position 1, and the carbon in position 2, which loses the hydrogen before the fragmentation takes place, through hydrogen transfer. The last step is the separation of the CO^+ and the HNC neutral fragment originating from the positions 1 and 2. Compared to the previous pathway, this last pathway appears as to be the most favourable one from an energetic point of view, since it involves single-bond breakings only. However, this

conclusion is not definitive, since further investigation should be performed.

5.3.3.1.3 COINCIDENCE ISLAND OF THE FRAGMENTS 28^+, 53^+ AND 55^0

This coincidence island represents the fragmentation of the hypoxanthine dication into two ions, of m/z = 28 and 53, and a neutral loss of 55 u. It is characterised by the highest intensity, meaning that this channel of fragmentation is the most favourable one (Figure 36). The process which hypoxanthine undergoes to follow this fragmentation pathway includes a hydrogen transfer, as illustrated on the left side of Figure 36. By observing the coincidence island slope, we find some difficulties in assigning. As seen on Figure 36, we displayed on the coincidence island the expected slopes for the three possible dissociation processes. The process consisting in the separation of the cation of m/z = 53 as a first step can be described as follows:

- 136^{2+} -> $83^+ + 53^+$

  -> $28^+ + 53^+ + 55^0$

The expected slope for this process, marked in gold on the Figure 36, is:

- Slope = $-83^+/28^+ = -2.96$

The second process that can be considered is the loss of the fragment of m/z = 28 as a first step:

- 136^{2+} -> $108^+ + 28^+$

  -> $28^+ + 53^+ + 55^0$

The calculated slope of this process, marked in orange, is:

- Slope = $-53^+/108^+ = -0.49$

Lastly, the process of having as a first step the neutral loss would lead to a slope of -1, as depicted in red in Figure 36.

As we can see, none of these slopes can alone describe the slope of the island. One possible explanation for the discrepancy between the

calculated slopes and the shape of the island could be the fact that the island results from more than one of the fragmentation processes considered here.

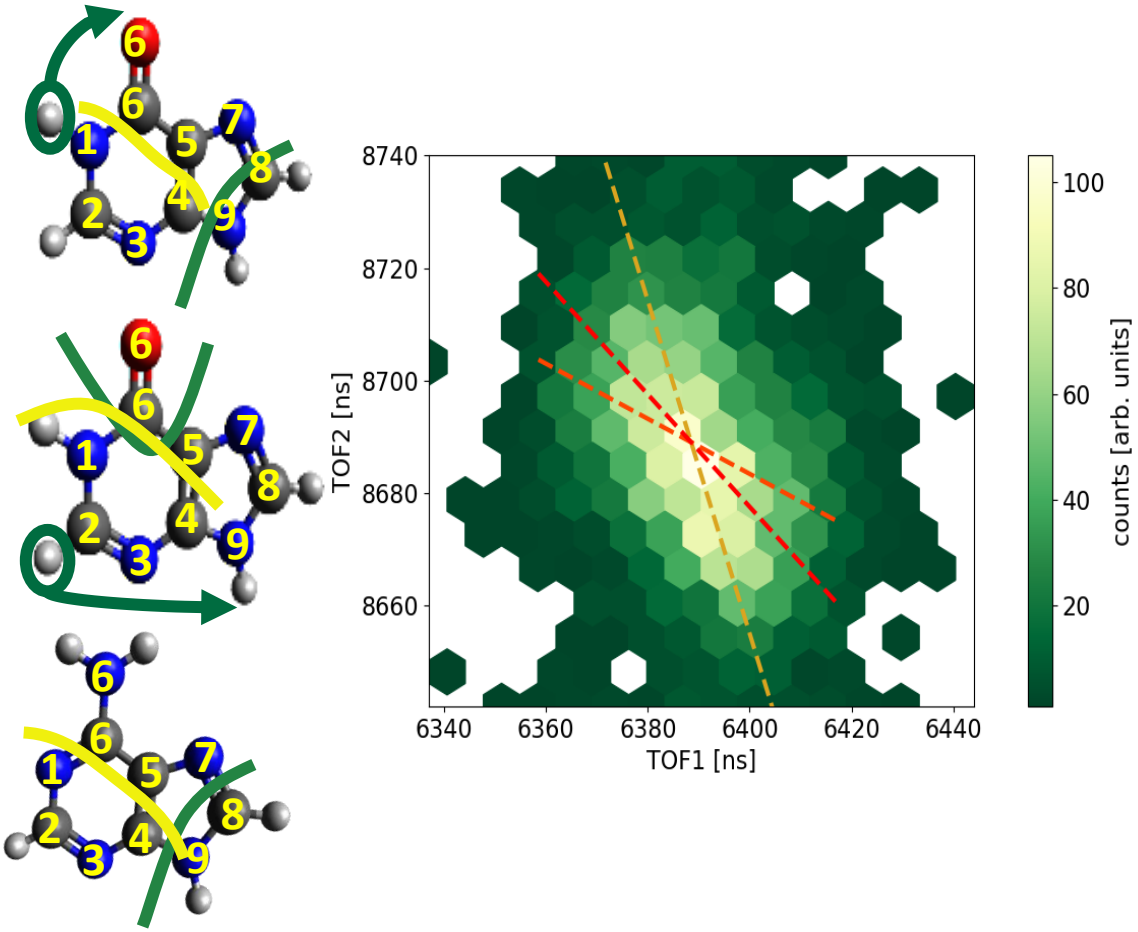

FIGURE 36: COINCIDENCE ISLAND OF THE FRAGMENTS 28^{+}, 53^{+} AND 55^{0} FROM THE ISOLATED HYPOXANTHINE DICATION. ON THE LEFT, THE HYPOXANTHINE MODEL WITH IN GREEN THE LINE OF DELIMITING THE FRAGMENT OF M/Z = 28 AND IN YELLOW THE NEUTRAL LOSS MARKING. ON TOP, THE OPTION FOR OBTAINING THE FRAGMENT $HCHN^{+}$ AFTER THE DISSOCIATION OF THE CATION OF M/Z = 83. IN THE MIDDLE, THE SECOND PATHWAY FOR OBTAINING THE THREE FRAGMENTS: IN YELLOW THE FIRST LOSS OF $C_2N_2H^{+}$ OF M/Z = 55 AND THEN THE SEPARATION OF CO^{+} FROM $C_2HN_2H_2{}^{0}$. ON THE BOTTOM, THE COMPARISON WITH THE CALCULATED RESULTS FROM LITERATURE REGARDING THE ADENINE MOLECULE. ON THE RIGHT THE COINCIDENCE ISLAND WITH IN GOLD THE CALCULATED SLOPE OF -2.96, IN ORANGE THE ONE OF -0.49, WHILE IN RED THE -1 ONE.

5.3.3.1.4 COINCIDENCE ISLAND FOR FRAGMENTS 28^+, 55^+ AND 53^0

This island can be considered as to be analogous to the previous one between the 28^+, 53^+ and 55^0 fragments. The only difference, in this case, is represented by the fact that the neutral loss corresponds to the fragment of 53 u, instead of the one of 55 u.

Given the shape of this coincidence island shown in Figure 37, we must take into account all of the three possible fragmentation pathways. The first one sees as a first step the loss of the neutral fragment. The process can be described as follows, and is represented by the red line (with a slope of -1) in Figure 37:

- 136^{2+} -> 83^{2+} + 53^0

  -> 28^+ + 55^+ + 53^0

The second fragmentation pathway to be considered is the process with the separation of the cation of m/z = 55 as a first step, described by the golden line in the Figure 37:

- 136^{2+} -> 81^+ + 55^+

  -> 28^+ + 55^+ + 53^0

The slope being:

- Slope = $-81^+/28^+ = -2.89$

The last fragmentation pathway, described by the orange line in the figure, originates from the initial loss of the lightest charged fragment (m/z = 28), followed by the separation of the cation of m/z = 108 into the fragments 55^+ and 53^0.

- 136^{2+} -> 108^+ + 28^+

  -> 28^+ + 55^+ + 53^0

The slope being:

- Slope = $-55^+/108^+ = -0.51$

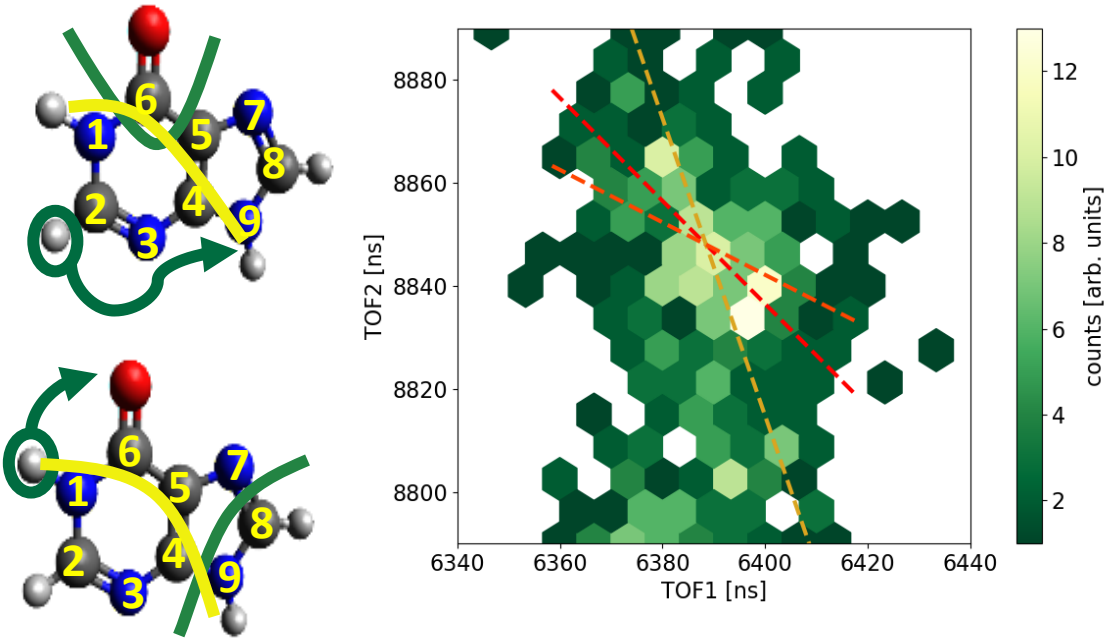

FIGURE 37: COINCIDENCE ISLAND OF THE FRAGMENTS 28^{+}, 55^{+} AND 53^{0} FROM THE ISOLATED HYPOXANTHINE DICATION. ON THE LEFT, THE HYPOXANTHINE MODEL WITH IN GREEN THE LINE OF DELIMITING THE FRAGMENT OF M/Z =28^{+} AND IN YELLOW THE NEUTRAL LOSS MARKING. ON TOP, THE OPTION FOR OBTAINING THE FRAGMENT CO^{+} AFTER THE NEUTRAL. THE BOTTOM MOLECULE MODEL SHOWS IN GREEN THE FRAGMENT OF $HCHN^{+}$ ION AFTER THE NEUTRAL LOSS. ON THE RIGHT WE CAN OBSERVE THE COINCIDENCE ISLAND WITH THE DIFFERENT SLOPE LINES (SEE TEXT).

In order to obtain the charged fragment of m/z = 55 and the neutral one of 53 u, a hydrogen transfer has to take place before any fragmentation has the time to take place. There are two possible hydrogen transfers for obtaining the fragments 28^{+}, 55^{+} and 53^{0}. The first one involves the hydrogen belonging to the nitrogen in position 1 being transferred to the oxygen in position 6. The second one implies that the hydrogen from the carbon in position 2 moves to the nitrogen in position 9. The first transfer, the one involving the hydrogen transfer from the nitrogen to the oxygen, seems the most favourable, given the higher electronegativity of oxygen compared to the one of nitrogen. After the hydrogen transfer, the fragmentation process can evolve by following the three pathways, as described above. When comparing these pathways with the calculations

performed on adenine, we notice an analogy between the first dissociation pathway proposed here and the one described in literature[30].

In this fragmentation process, we witness the loss of the neutral fragment C_2N_2H of 53 u. This fragment is represented by the gold line on both molecular models in the Figure 37, with the loss of one hydrogen going to the dication fragment in the process. Depending on where the hydrogen coming from the neutral fragment is transferred, the dication divides into a fragment of m/z = 28 corresponding to either CO^+ or $CHNH^+$. The counter cation of m/z = 55 would be $C_2H_3N_2^+$ in the first case, or C_2HNO^+ in the second case, as it can be seen in the Figure 37. Once again, the pathways resembling the one underwent by adenine, *i.e.* loss of $CHNH^+$ rather than CO^+, could be the most eligible one.

It is noteworthy saying that this event of having nominally the same fragments with a different charge distribution is found at least once more within the coincidence map. This is particularly the case of the fragments with masses of 39, 53 and 44 u.

5.3.3.1.5 COINCIDENCE ISLAND OF THE FRAGMENTS 44^+ AND 92^+

One of the most interesting island in the coincidence map shown in Figure 38 is represented by the dissociation of the hypoxanthine dication in two cationic fragments of m/z = 44^+ and 92^+. In fact, the peculiarity of this dissociation process is that it presents a delayed fragmentation. This is illustrated by the diagonal track down the [7940, 11380] ns island. Besides from being the analogous of the coincidence island encountered for the adenine molecule in the works from Alvarado[29] and Moretto-Capelle[30], this coincidence island presents a delayed fragmentation that is also observed in the data presented by Moretto-Capelle et al[30]. This kind of coincidence island is observed when the metastable dication undergoes fragmentation while travelling in the Time-of-Flight zone. Figure 39 shows the coincidence island at the beginning of the delayed fragmentation. Since it represents the separation of the hypoxanthine dication into two charged fragments, the slope of the island is expected to be of -1. The fragmentation process is the one described as follows:

136^{2+} -> 44^{+} + 92^{+}

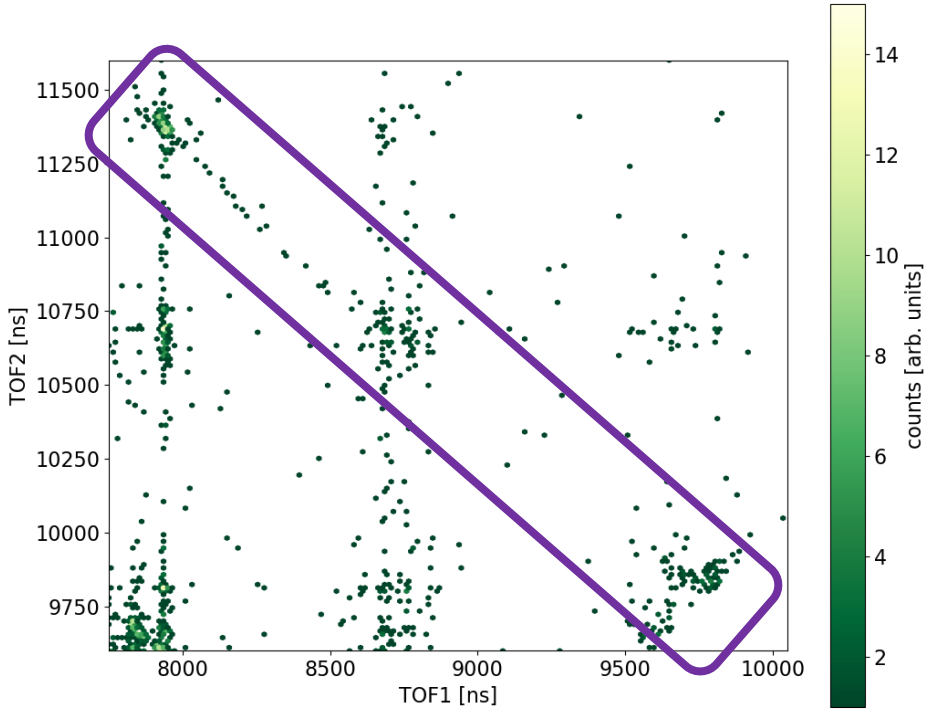

FIGURE 38: DELAYED FRAGMENTATION OF THE ISOLATED HYPOXANTHINE DICATION INTO THE FRAGMENTS OF $M/Z = 44^{+}$ AND 92^{+} HIGHLIGHTED IN PURPLE.

Also in this case, the lightest fragments of $m/z = 44$ is the product of a hydrogen transfer, as it was described in the case of adenine[30]. The difference with the hypoxanthine dication resides in the fact that the production of the fragment $m/z = 44$ requires the participation of the oxygen atom, thus making unlikely the involvement of the imidazole ring, which would require the cleavage of two double bonds.

Having considered these coincidence islands as the analogous of the most significant ones obtained from the dissociation of the adenine dication, we can conclude that the analogies rely most notably on the most favourable breaking points of the molecule. However, when investigating the fragmentation dynamics by analysing the islands presenting a three-body dissociation, it appears that the mechanisms are more complex in case of hypoxanthine, and the followed pathways, even if resulting most probably

in analogous fragments, are not the same, as seen from the shape of the coincidence islands.

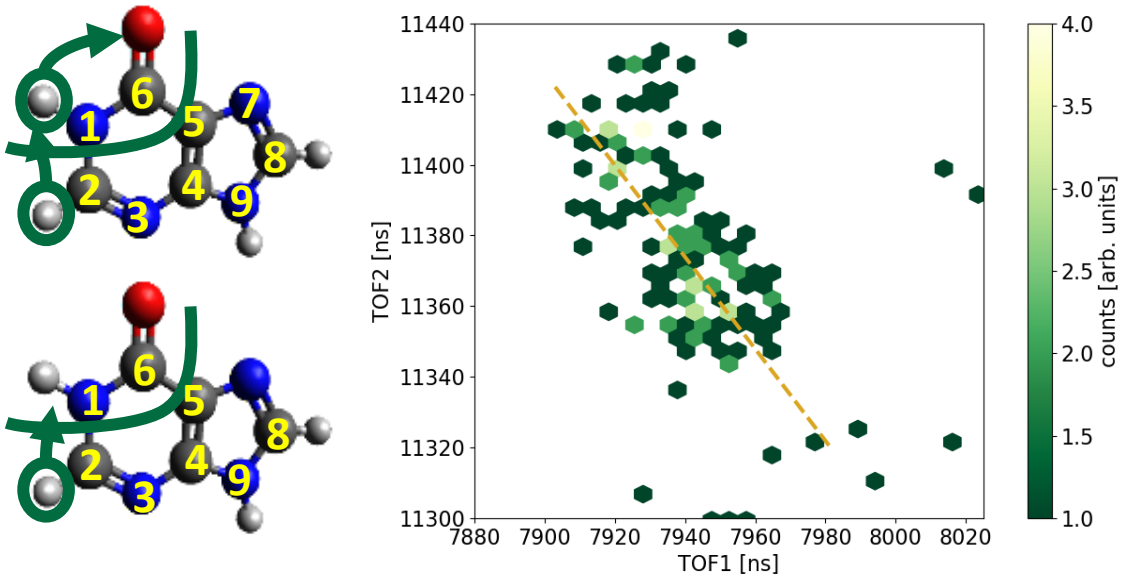

FIGURE 39: ON THE RIGHT, COINCIDENCE ISLAND OF THE FRAGMENTS 44^{+} AND 92^{+} FROM THE ISOLATED HYPOXANTHINE DICATION, ZOOM ON THE ISLAND FORMED AT THE BEGINNING OF THE FRAGMENTATION, WITH THE SLOPE OF -1, IN GOLD. ON THE LEFT, THE MODEL OF THE STRUCTURE OF THE TWO FRAGMENTS INVOLVED, ON THE RIGHT

5.3.3.2 CONCLUSIONS ON THE ION-INDUCED FRAGMENTATION

From the obtained results, we arrive to the following conclusions. From the studies performed thanks to the ion-induced fragmentation, the isolated hypoxanthine presents a behaviour that closely resembles the ones of the two most common DNA and RNA forming purines, adenine and guanine, in terms of the molecule's most common breaking points upon ionising radiation. Interestingly, there appears a high level of hydrogen transfer among the atoms forming the molecule, phenomenon that is even more evident when analysing the dication coincidence map. This suggests that in order to obtain the most stable ionic fragments, the hydrogen moves accordingly. Moreover, always observing the coincidence map, we can identify the most favourable breaking points. The first one is represented by the fragments CO^{+} and $HCNH^{+}$ of m/z = 28, being found six times as

ion, and once as a neutral loss, in the most representative coincidence islands that we have described here. In fact, the m/z = 28 fragment is found in the most intense island, which comprises also the fragments 53^{+} and 55^{0}. Another fragment commonly found is the one of m/z = 44, which corresponds to the $HNCOH^{+}$ ion and stands as the most striking example of hydrogen transfer for this molecule. Another interesting aspect of this coincidence map is the fact that the most intense coincidence island represents the breaking of the C=C bond common to the imidazole and pyrimidine rings. This phenomenon of the breaking of the aromatic bonds that occurs in other coincidence islands, as it was seen before, is remarkable since the double bond between C4 and C5 is supposed to give the molecule its stability but it is actually the one which is broken in the most representative fragmentation pathway. In order to shed some light on the subject, comparison can be made with the results obtained by Sadr-Arani *et al.*[23] for the adenine molecule, for which DFT calculations were performed to procure a theoretical model that could describe what phenomena were taking place. As it was presented in the article, when ionised, the double bonds of the adenine molecule appeared to weaken, while the single one strengthened, leading to an easier access to the scission of the double bonds. Given the similarities of adenine and hypoxanthine, this could be presented as a plausible explanation of the many fragmentation channels in the coincidence map that, at first glance seem "unlikely" due to the fact that they include the breaking of the aromatic bonds. However, theoretical studies especially designed for these experiments should be performed in order to gain insight, but it is a first step towards a better understanding of the mechanisms taking place during these events that have just been described in the present work.

When moving the attention towards the mass spectra obtained from the pure and hydrated clusters of hypoxanthine, thanks to the fragmentation portion of the spectra, which had been compared to that of the isolated molecule mass spectrum, we can observe some new features that can be attributed to protonation processes taking place from a cluster fragmentation.

To complement our study on the stability of hypoxanthine upon irradiation, in the next section we present a comparative study of the changes in the chemical properties of the hypoxanthine molecule when it is surrounded by other molecules compared to the case when it is isolated. For that study, the experimental method is based on X-ray photoelectron spectrometry (XPS).

5.4 CHEMICAL PROPERTIES OF HYPOXANTHINE AS A FUNCTION OF ITS MOLECULAR ENVIRONMENT

5.4.1 XPS ACQUISITION PARAMETERS

The XPS spectra for the C 1s, N 1s and O 1s signals from pure clusters were acquired using the CELENO cluster source at different oven temperatures. (It is recalled that these signals result from the X-ray-induced ejection of 1s electrons from C, N and O atoms.) A first set of data was collected at 481 K, while a second set was recorded at 487 K. The oven temperature was varied in order to appreciate if any significant difference was observable in the electron spectra as the size of the molecular clusters was increased. Indeed, as discussed earlier, the cluster size distribution is moved towards bigger clusters as the oven temperature increases, as more molecules are expulsed. The He gas flow was kept at 180 mL/min during the whole experiment, with a pressure of 18 mbar for the pure clusters, and 18.5 mbar for the hydrated ones, since water molecules were in the gas flow. The data concerning the hydrated species were collected at 490 K.

The C 1s spectra were collected at a photon energy of 370 eV, the N 1s ones at 480 eV, and the O 1s ones at 610 eV. This means that the present XPS spectra were measured at about 70 eV above the *K*-shell ionization thresholds of the different atomic species. All of the obtained spectra for the C 1s, N 1s, and O 1s signals have been calibrated in binding energy as follows. For the C 1s signal, the calibration in energy was performed by injecting CO_2 into the analysing chamber and by referring to the corresponding C 1s peak at 297.7 eV, according to the work of Myrseth *et al.*[74]. The signal for N 1s was calibrated thanks to the injection of N_2 into

the chamber, and by using the peak located at 409.9 eV as a reference, as in the work of Plekan *et al.*[33]. For the O 1s signal, the reference was obtained from the H_2O background in the analysing chamber, by considering the corresponding O 1s peak at 539.79 eV[75]. The resolution of the C 1s signal, taking into account both photon energy bandwidth and the analyser resolution, was about 0.6 eV, while the N 1s one was of 0.9 eV, and the O 1s one of 0.9 eV. On one hand, organic compounds forming non covalent bonds, such as hypoxanthine clusters, present a heterogeneous environment, and thus, are more prone to signal broadening[76]. Moreover, some imperfections on the experimental setup might also contribute to signal broadening[76]. Hence, since the sources of peak broadening are mostly due to experimental conditions and sample nature, all the spectra presented next were treated with Gaussian fitting instead of Gaussian-Lorentzian fitting.

5.4.2 COMPARISON OF THE XPS RESULTS FOR THE ISOLATED MOLECULE AND FOR PURE AND HYDRATED CLUSTERS

The hypoxanthine molecule is characterised by an imidazole ring conjugated to a pyrimidine one, with an oxygen attached in position 6 (Figure 40). This structure guarantees the molecule a certain level of stability. From this molecular structure, one can predict four different potential signals from carbon, two from nitrogen, and one from oxygen. The different C 1s signals are related to the following carbon atoms:

(i) the carbon in position 5 which is the one with the larger number of carbon atoms surrounding it, with the bonds C-C=C and C-N,
(ii) the C2 and C8 atoms in the bonds HN-CH=N,
(iii) the C4 atom involved in the bonds C=C and HN-C-N,
(iv) the carbon bound to the oxygen.

For the nitrogen, the two groups are related to the imine N atoms in positions 3 and 7 and to the amine N atoms in positions 1 and 9.
The only oxygen is the one in position 6.

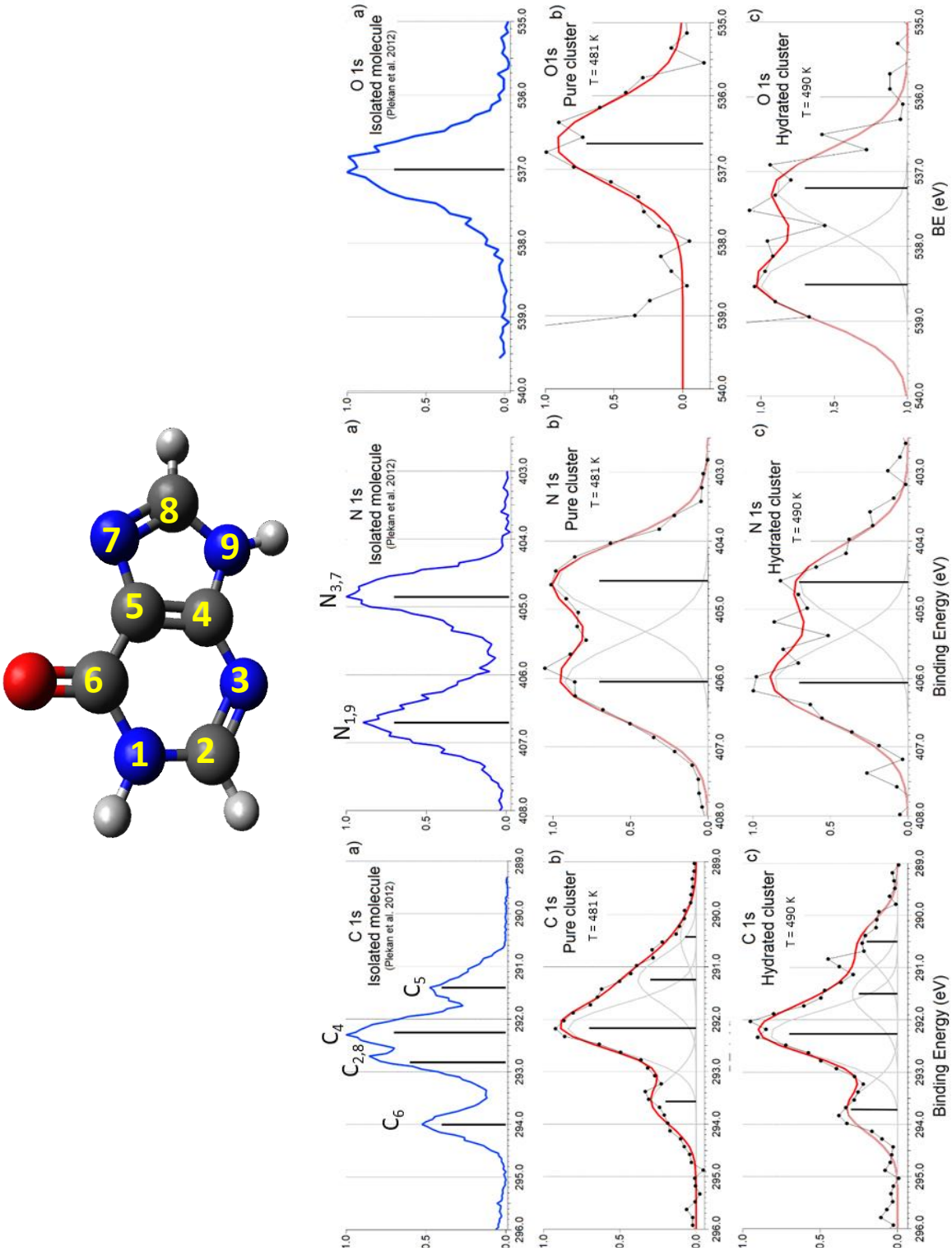

FIGURE 40: COMPARISON OF ALL OF THE XPS SIGNALS ACQUIRED AS A FUNCTION OF THE BINDING ENERGY OF THE 1S ELECTRONS. FROM LEFT TO RIGHT: THE C 1S, THE N1S SIGNAL, AND THE O 1S SIGNAL. FOR ALL OF THE THREE SIGNALS, THE PANEL A) REPRESENTS THE ISOLATED HYPOXANTHINE SPECTRUM RETRIEVED FROM THE LITERATURE (PLEKAN ET AL. 2012). THE PANELS B) AND C) SHOW THE PURE AND THE HYDRATED CLUSTERS SIGNALS RESPECTIVELY. THE CLUSTER SPECTRA HAVE BEEN DECONVOLVED TO APPRECIATE THE SINGLE COMPONENT CONTRIBUTION IN DIFFERENT ENVIRONMENTS.

The comparison of the carbon, nitrogen and oxygen photoelectron spectra of the isolated hypoxanthine (Plekan *et al.*[33]) and of its clusters (pure and hydrated) is presented in Figure 40 and the details concerning each peak are listed in Table 1. Even though the number of C 1s and N 1s peaks present in each XPS spectrum is unchanged between the isolated hypoxanthine and the clusters, the relative intensity of the peaks, their width, and the corresponding binding energies undergo significant changes. As it was described for the uracil clusters[8,50], these last three effects caused by the change in the molecule aggregation state, can be explained as follows. By belonging to quite large clusters, the atoms may be involved in both covalent bonds to form molecules and non-covalent interactions with other molecules surrounding them in the cluster[8,50], thus making the XPS spectra dependent on the atomic and molecular environment.

Going into more detail, when analysing the C 1s spectrum of the pure clusters (Figure 40, left, panel b), the broadening and merging of its components appear prominent. A contribution to the observed broadening may stem from the fact that the cluster sample involved a variety of cluster sizes. The peak corresponding to the carbon in position 5 appears as the less intense because it is not involved in any of the non-covalent interactions[33] that form both the pure and hydrated clusters. Its peak is centred at 290.43 eV in case of pure clusters, i.e. 1 eV below the one present in the isolated molecule. Similarly, the intensity decrease of the peak corresponding to the carbon in position 4 is also due to the fact that this carbon atom is not involved directly in any weak interaction. For the pure clusters, this peak is centred at 291.25 eV, again 1 eV below the one for the isolated molecule. Concerning the dominant peak related to the carbons in positions 2 and 8, its predominance is likely to be due to both the fact that it is the only peak that is associated to two carbon atoms and the fact that each of these C atoms is bound to a hydrogen atom, which is involved in non-covalent interactions. The corresponding peak is at 292.17 eV in case of pure clusters, i.e. 0.65 eV below the energy of the

peak observed for the isolated molecule. Lastly, the carbon in position 6 is still located at higher energy compared to the other peaks, because of its bond to the oxygen atom, which is greatly involved in the weak interactions taking place in the cluster. Its peak is at 293.57 eV, 0.43 eV lower than the one for the isolated molecule.

TABLE 1: COMPARISON OF THE SIGNAL PEAK POSITIONS AND RELATIVE AREAS BETWEEN THE PURE AND HYDRATED HYPOXANTHINE CLUSTERS.

C 1s				**N 1s**			
		Peak (eV)	**Area (%)**			**Peak (eV)**	**Area (%)**
C5	Isolated[33]	291.40	//	**N3,7**	Isolated[33]	404.85	//
	Pure	290.43 (±0.28)	6 (±0.02)		Pure	404.58 (± 0.02)	51.27 (± 0.03)
	Hyd	290.51 (±0.06)	14 (±0.04)		Hyd	404.63 (± 0.07)	44.83 (± 0.08)
C4	Isolated[33]	292.25	//	**N1,9**	Isolated[33]	406.70	//
	Pure	291.25 (±0.07)	24 (±0.03)		Pure	406.04 (± 0.02)	48.73 (± 0.03)
	Hyd	291.51 (±0.17)	18 (±0.34)		Hyd	406.06 (± 0.06)	55.17 (± 0.08)
C2,8	Isolated[33]	292.82	//				
	Pure	292.17 (±0.02)	52 (±0.03)	**O 1s**			
	Hyd	292.27 (±0.23)	49 (±0.35)			**Peak (eV)**	**Area (%)**
C6	Isolated[33]	294.00	//		Isolated[33]	537.00	//
	Pure	293.57 (±0.03)	18 (±0.02)		Pure	536.65 (± 0.04)	100 (± 0.08)
	Hyd	293.72 (±0.06)	19 (±0.03)		Hyd	537.22 (± 0.21)	100 (± 0.43)

In the case of the N 1s spectrum of the pure cluster (Figure 40, centre, panel b); we observe the two shoulders of the N 1s signal with very similar intensities. For the pure clusters, the peak at 404.58 eV can be attributed to the imine groups ($N_{3,7}$); it is 0.27 eV below the signal of the isolated molecule. The peak at 406.04 eV can be assigned to the amine groups ($N_{1,9}$) and it is 0.63 eV below the isolated hypoxanthine peak.

The O 1s spectrum presents only one component, since there is only one atom present in the molecule (Figure 40, left, panel b). Its peak is at 536.65 eV, 0.35 eV below the one of the isolated hypoxanthine. Similarly, to what has been observed for the other two signals, this peak is broadened and shifted towards lower binding energies in the cluster compared to the isolated molecule.

It should be noted that the truncated signal rising on the left side of the cluster O 1s spectra (Figure 40) is due to the O 1s signal originating from the oxygen atom of isolated water molecules. According to Sankari *et al.*[75], this signal is centred at 539.79 eV (Figure 41). (As aforementioned, this water signal was actually used for the calibration of the present O 1s spectra). When producing clusters, there was always some humidity in the sample, even during experiments dedicated to pure hypoxanthine clusters. This is the reason why a high-intensity signal due to isolated water molecules was observed not only in case of hydrated clusters, but also in case of pure clusters (Figure 41).

When observing the spectra obtained for the hydrated cluster, we observe some further changes in the spectral features, as it can be seen in the bottom panels of Figure 40. Starting with the C 1s signal (left bottom), we can clearly see that the peak related to the carbon in position 6, which is oxygen-bonded, has shifted to 293.72 eV; nearly 0.2 eV higher than the signal coming from the pure clusters. This signal has grown in intensity compared to the dominant peak (see Table 1). This phenomenon is caused by the increased involvement of the oxygen atom in the formation of an H-

bond network with both hypoxanthine and water molecules. Going to the peak relative to the carbons in positions 2 and 8, we observe that the peak has shifted by 0.1 eV to higher binding energies (compared to pure clusters), at 292.27 eV, while its relative intensity has decreased, as it can be seen in the Table 1. Concerning the signal of the carbon in position 4 observed for hydrated clusters, its peak has shifted of 0.26 eV to higher binding energies, going to 291.51 eV, and its relative intensity has decreased (Table 1). The signal due to the carbon in position 5 has an increased relative intensity, becoming almost as intense as the signal due to the carbon in position 4. Compared to pure clusters, this C5 signal presents the least significant shift in binding energy, a shift of 0.08 eV, placing its peak at 290.51 eV in case of hydrated clusters. This is due to the fact that this carbon is the one to be the least affected by its surrounding and by the formation of H-bonds, since it has all of its valence electrons occupied in covalent bonds. The N 1s signal does not present significant variations in the binding energy shifts: the position of the peak relative to the imines has increased of 0.05 eV, going from 404.58 to 404.63 eV, while the amine peak goes from 406.04 to 406.06 eV. This latter variation falls within the uncertainty of the measurement (see Table 1), making this variation insignificant. What seems to be more significant in this spectrum is the variation of the relative intensities. If in the pure cluster, the two components were of about equal intensity; in the hydrated cluster, the signal of the amine groups represents about 55 % of the total N 1s signal. This is likely to be caused by the stronger involvement of the amine groups in the formation of the new H-bonds with water molecules. The most significant variation is observed for the oxygen signal. This signal has shifted from 536.65 to 537.22 eV, and presents a new feature at 538.51 eV, corresponding to the signal of the new pure water clusters formed during the process[8,50]. As for the other signals presenting important variation, the shift in the binding energy of the O 1s electron can be attributed to the involvement of the O atom in the formation of the hydration network of the cluster.

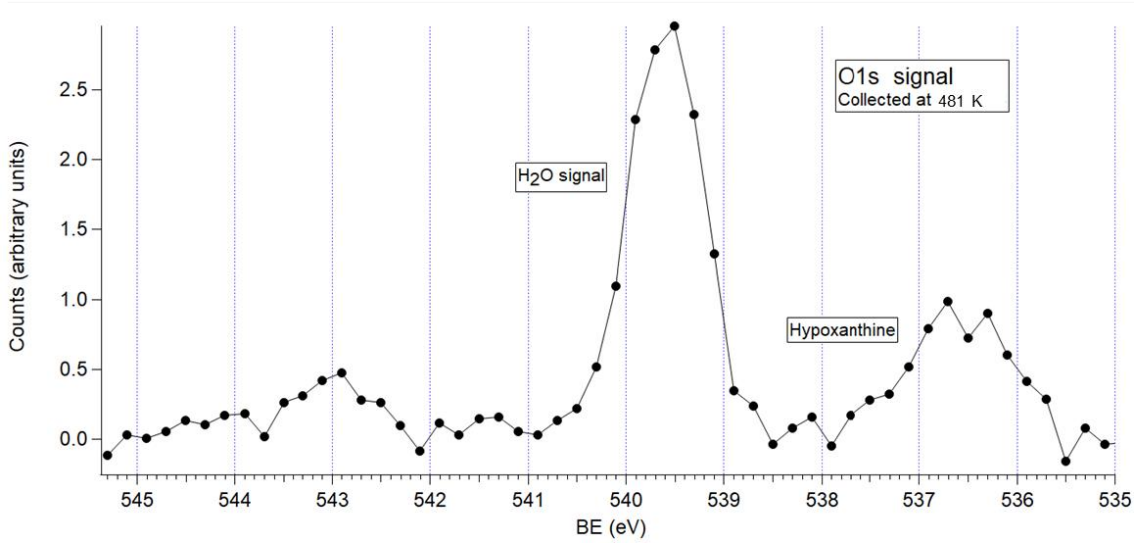

FIGURE 41: XPS O 1S SPECTRUM ACQUIRED FOR PURE HYPOXANTHINE CLUSTERS AS A FUNCTION OF THE BINDING ENERGY OF THE 1S ELECTRONS.

To summarize, we note that the cluster formation does indeed affect the spectral features of the hypoxanthine molecule, both in *K*-shell binding energy and relative intensities, according to the involvement of its constituting atoms in the intermolecular interaction.

In an attempt to investigate the cluster-size dependence of the XPS spectra collected during the PLEIADES experiment, we varied the oven temperature from 481 K to 487 K, with the aim of varying the cluster size distribution. The obtained results are reported in Figure 42, and Table 2. First, we observe no significant variation in the position of the peak components, neither for the carbon spectra nor for the nitrogen spectra, when comparing the data acquired at the oven temperature of 481 K with the ones at 487 K. Second, when considering the relative areas of each peak of the carbon signal, we observe that the one relative to the carbon in position 5 does not change significantly between the two temperatures. The areas of the other peaks present more pronounced variation: at 487 K, the peak due to the carbon in position 4 has 2.2 % less percentage area compared to the one obtained at 481 K, and the signal relative to C2 and C8 at 487 K has 1.5 % less percentage area. Finally, at 487 K, the signal relative to the carbon bound to the oxygen atom has 3.3 % more percentage

area compared to the one at 481 K. Considering the areas of the nitrogen components, we cannot appreciate any significant variation.

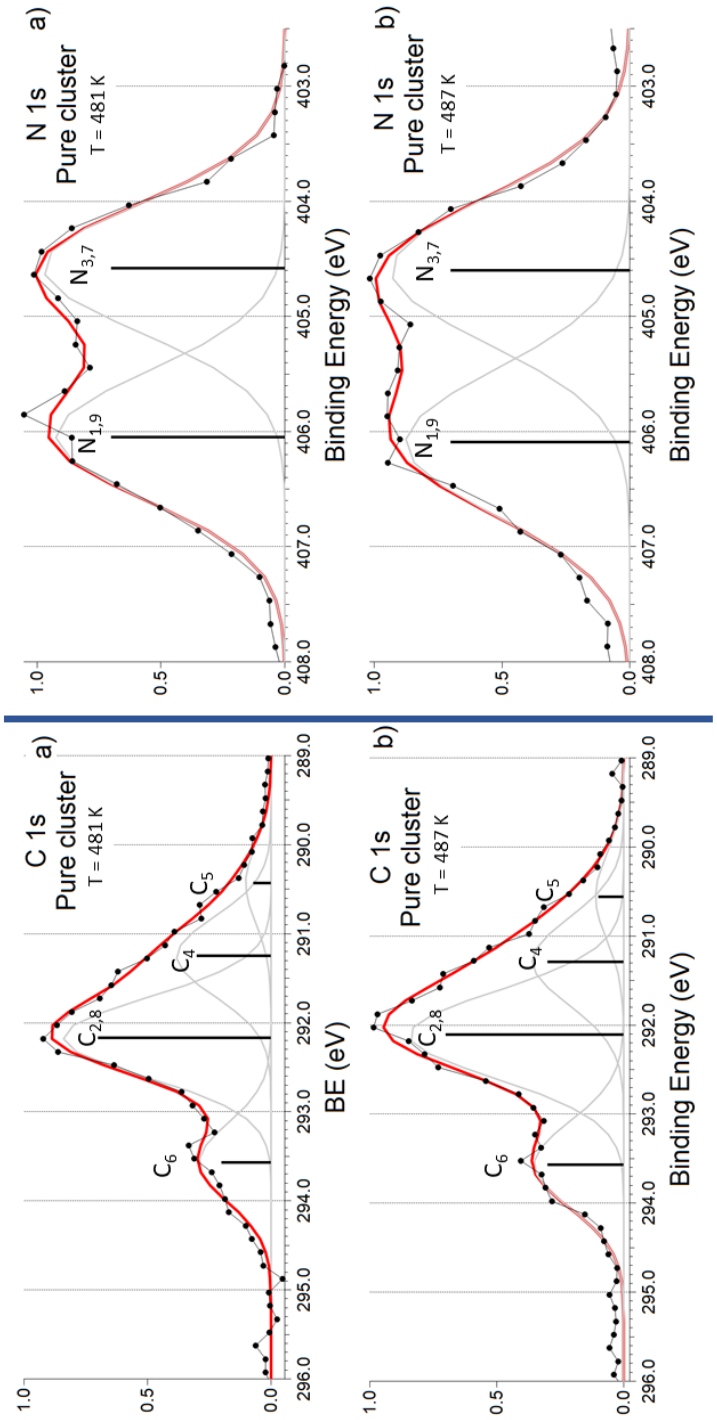

FIGURE 42: COMPARISON OF THE EFFECTS DUE TO THE OVEN TEMPERATURE ON THE PURE HYPOXANTHINE CLUSTERS. ON THE LEFT THE C1S SIGNALS, PANEL A) THE DATA COLLECTED AT 481 K AND IN PANEL B) AT 487 K. ON THE RIGHT THE XPS SPECTRA FOR THE N 1S SIGNAL, PANEL A) AT 481 K, AND PANEL B) AT 487 K.

TABLE 2: COMPARISON OF THE C 1S AND N 1S SIGNAL AT DIFFERENT OVEN TEMPERATURES.

C 1s			
		Peak (eV)	**Area (%)**
C5	481 K	290.43 (±0.28)	6 (±0.02)
	487 K	290.58 (±0.31)	6.43 (±0.11)
C4	481 K	291.25 (±0.07)	24 (±0.03)
	487 K	291.29 (±0.19)	21.8 (±0.06)
C2,8	481 K	292.17 (±0.02)	52 (±0.03)
	487 K	292.11 (±0.04)	50.49 (±0.08)
C6	481 K	293.57 (±0.03)	18 (±0.02)
	487 K	293.57 (±0.03)	21.28 (±0.01)
N 1s			
		Peak (eV)	**Area (%)**
N3,7	481 K	404.58 (±0.02)	51.27 (± 0.03)
	487 K	404.60 (±0.02)	51.54 (± 0.04)
N1,9	481 K	406.04 (±0.02)	48.73 (± 0.03)
	487 K	406.09 (±0.02)	48.46 (± 0.04)

As the variations observed in the carbon signal are anyway small, it seems that the variation of the clusters size, obtained by increasing the oven temperature from 481 K to 487 K, does not affect significantly the spectral lines. However, when comparing the characteristics of the data collected at DESIRS and PLEIADES, we should note that all of the temperatures at which the spectra were collected during the PLEIADES experiment were lower than the ones taken at the DESIRS beamline. This means that, during the XPS experiments on the pure clusters, the monomer component was probably still quite strong, compared to what has been observed at higher temperatures. A similar statement can be made for the hydrated clusters. In fact, as the monomer signal is still well present in the mass spectra collected at DESIRS for the pure clusters, and since the XPS data were collected at lower temperature, we can infer that the signals from both the isolated molecule and the pure clusters contribute significantly to the spectral features. Hence, if we were to reiterate the experiments at higher oven temperatures, we might observe more distinctive features that could be more accentuated than the few differences observed with the present data. Unfortunately, the XPS spectra were collected before the characterisation of the CELENO source at DESIRS so that we could not anticipate the cluster size distribution.

5.4.3 Concluding remarks on the properties of hypoxanthine as a function of its molecular environment

The XPS data provided us with interesting insight regarding the changes in the chemical properties of the hypoxanthine molecule when it is surrounded by other molecules compared to the case when it is isolated. For the pure hypoxanthine clusters, we observed some changes, namely the shift of all the XPS spectra towards lower binding energies of the 1s electrons and the broadening of the spectral features. This broadening can be explained by the fact that in large clusters, all the molecules do not have the same molecular environment and thus have different electron binding energies, resulting in an apparent broadening. In addition, the influence

of the hydrogen bonds overall lowers the binding energy of the electrons. This means that the formation of hydrogen bonds puts the core electrons in a less attached state to their nucleus. Further changes of the spectral features of the hypoxanthine XPS signals are observed in the case of the hydrated clusters. In this case, the influence of hydrogen bonds formed with water molecules further modifies certain features of the signal, especially the ones involving more or less directly the oxygen atom. Indeed, in the C 1s hydrated cluster spectrum, the signal due to the C6 atom, which is bound to the oxygen atom, presents an increased relative intensity as well as a slight increase in binding energy (0.15 eV) because the oxygen is actively involved as a hydrogen acceptor from the water molecule. Concerning the N 1s spectrum for the hydrated cluster, the signal coming from N atoms belonging to the amine groups has increased in intensity thanks to their role as hydrogen donors. Lastly, compared to pure clusters, the O 1s signal presented an obvious increase of 0.57 eV in the binding energy in case of hydrated clusters, due to the fact that the oxygen atom behaves as an acceptor in the hydrogen bond formed with a water molecule. Moreover, in contrast to the case of pure clusters, an intensive O 1s signal appears at the energy of 538.51 eV in the case of hydrated clusters. It is important to note that all of these observations are analogous with the findings of Mattioli[8,50] for the uracil hydrated clusters, thus suggesting that a significant contribution to the intensive O 1s signal centred at 538.51 eV may stem from water clusters.

The spectral feature, which in Mattioli *et al.*[8] is attributed to the water-uracil mixed cluster, peaks at 538.2 eV and merges with the spectral feature related to water clusters and centred at about 538.9 eV. In the present XPS spectrum obtained for hypoxanthine-hydrated clusters, similar merging may occur for O 1s signals originating from water clusters and hypoxanthine hydrated clusters. Further work is however needed to make it possible to conclude on this last aspect.

5.5 RESULTS SUMMARY

- In the context of this thesis, the hypoxanthine molecule has been studied under three aggregation gaseous states: isolate molecule, pure cluster, and hydrated cluster.
- We have performed three different experiments on hypoxanthine: VUV mass spectrometry at the DESIRS beamline, and XPS spectroscopy at the PLEIADES beamline, where both pure and hydrated clusters were analysed; while ion-induced fragmentation was investigated by means of the COLIMACON set-up at the ARIBE beamline, both for the isolated molecule and for the clusters.
- The mass spectra obtained from the VUV mass spectroscopy proved, on one hand, to be a good departing test for the coupling of the cluster source CELENO to the DESIRS beamline. The experiment also showed how different cluster source conditions affects the cluster size stability and distribution. In particular, we have observed how the oven temperature can affect the size distribution of the pure molecular clusters; and how the hydration level can be regulated by adjusting the position of the Nafion® tube relative to the water used for the hydration.
- The mass spectra obtained with the ion-induced collisions proved that the isolated molecule presents a very similar fragmentation pattern compared to the adenine one. First of all, the isolated molecule showed a high molecular stability upon ionic impact. Then, two main fragmentation pathways were identified, which are analogous to the adenine ones. In addition, the dication coincidence map presents features similar to the adenine ones. The observation of the pure and hydrated cluster spectra displays some common new features, due to the molecule protonation. However, we observed neither new fragments resulting from the cluster dissociation, nor hydrated fragments originating from the monomer forming bonds with the surrounding water. This last aspect might be due to the low hydration level of the cluster.

- The data obtained from the XPS spectra analysis showed that the pure hypoxanthine clusters present the same main features as the isolated molecule, even if there exist differences caused by the aggregation state. The hydrated clusters, on the other hand, present new features due to the hydrogen bonds with the water molecules. These include an increased signal of the amine groups, a shift towards higher binding energies of the O 1s signal, as well as the appearance of a specific water cluster signal on the O 1s spectrum.

6 CONCLUSIONS AND PERSPECTIVES

6.1 CONCLUSIONS

Being a biologically relevant molecule, involved in several cellular signalling and pathways, hypoxanthine has been studied in the gas phase during this thesis project at a growing system complexity level. This allowed us to obtain a more detailed picture on how the molecule may behave in a more lifelike cellular environment.

6.1.1 MASS SPECTRA OBSERVATIONS

From the data analysis and interpretation, the following conclusions have been drawn. Besides from manifesting a high molecular stability upon its impact with highly charged ions, hypoxanthine behaviour resembles closely the one observed with the other nucleic acid forming purine bases, adenine and guanine. We have observed that the two main fragmentation pathways are common to both adenine and hypoxanthine. These channels involve the loss of the HCN^0 neutral fragment as a common first step. Depending on whether this group is lost on the pyrimidine or imidazole ring, two different processes are set into place. Moreover, the loss of the CO^0 neutral fragment, which closely resembles the process that takes place during the guanine fragmentation, represents a significant fragmentation pathway for hypoxanthine. The coincidence map further confirms the analogy between adenine and hypoxanthine. These results provide support to the idea that generally the purines present a set of common characteristics. First, given the fact that they are all aromatic double rings, each with specific substituents, they present a high molecular stability upon ionisation. This high stability is also the physical justification of having them as the keepers of the genetic information in living cells, although presenting a low, but not equal to zero, degree of mutation upon ionisation. Then, the three purines present a common array of fragmentation points, namely the two HCN groups in position 2-3 and 7-8, and the other one being the separation of the two rings with the double bonded carbons in the position 4-5, though with the specificities of each

molecule. Moreover, this study highlighted that during the formation of the clusters, both adenine and hypoxanthine present the involvement of their ring substituents in the formation of hydrogen bonds. The analysis of the cluster growth emphasizes the importance of the oxygen substituent in position six, helping the stabilisation of the pure clusters, and favouring the hydration of the molecule when producing water-mixed clusters.

6.1.2 SR-XPS OBSERVATIONS

When taking into consideration the data obtained from the SR-XPS experiment, we can conclude that the pure hypoxanthine clusters present the gross same features as the isolated molecule. The remarkable difference between the two different aggregation states consists in the general broadening of the spectral features and their shift towards lower binding energies in case of clusters. These changes could be easily attributed to the aggregation state of the clusters and their size. No significant changes were observed in the spectral features when the temperature was modified during the experiment. The information obtained for the hydrated clusters closely resembles the information already available concerning the pyrimidine uracil. In fact, the modification in the obtained spectra concerns the increase of the intensity and slight shift towards higher *K*-shell binding energy of the amine group in the N 1s spectrum, which imply its involvement in the formation of new hydrogen bonds, to be attributed with the water oxygen. As it was predictable, the other new feature for hydrated clusters involves the O 1s spectrum, which presents a significant shift towards higher binding energy for the hypoxanthine oxygen atom and a new peak attributed to the formation of water clusters. The increase of this binding energy is a clear indication of the involvement of this oxygen atom in the formation of the hydrated clusters.

6.2 PERSPECTIVES

6.2.1 FURTHER PROJECTS ON HYPOXANTHINE

In order to better understand the underlying fragmentation process, it would be necessary to actually determine the stability asymmetry between the two HCN groups coming from either the imidazole or the pyrimidine ring. In fact, previous DFT calculation had been performed on the adenine molecule. The implementation of the same theoretical calculation process could be a useful step towards a further hypoxanthine characterisation. It could accentuate the similarities and differences with the nucleobase-forming adenine and guanine, and provide a better explanation of the observed fragmentation pathways, both in the mass spectrum and the coincidence one. Another, but not mutually exclusive, option could be to perform once again the ion-induced fragmentation, this time employing a hypoxanthine molecule presenting a hydrogen isotope in one of the two HCN groups. This could experimentally determine the origin of that fragment, thus confirming which one of the two aromatic ring is the most stable one.

6.2.2 NEW MIXED CLUSTERS

Considering the cluster growth studies, a further step could be represented by the formation and analysis of mixed clusters. For example, some interesting samples could be represented by the dimers hypoxanthine-cytosine and hypoxanthine-uracil, which are the couples present on the last codon-anticodon pairs during the RNA translation. Moreover, a detailed comparison of their stability upon irradiation with the one of the canonical pairs, namely adenine-uracil and guanine-cytosine could be interesting. Moving even further, in a parallel manner to what has been performed during this work; the study of these dimers in an aqueous phase could provide an even more complex sample environment interaction, which could offer us a better idea of what could happen in a real cellular environment when it interacts with ionising radiations of various kinds. The studies of the hypoxanthine-pyrimidine could also present themselves

as interesting subject studies for SR-XPS spectrometry. This procedure would provide further information regarding the parallelisms and differences occurring between the canonical and this non-canonical base pair. This could provide a basis for further experiments involving the use of RNA strands presenting one, or more, hypoxanthine molecules and observing how those strands fold, and how they react to ionising radiation.

7 SYNTHÈSE EN FRANÇAIS (30 PAGES)

7.1 CONTEXTE ET MOTIVATION

7.1.1 INTRODUCTION

La caractérisation des biomolécules est essentielle pour mieux comprendre leurs propriétés et en particulier, leur activité biologique. L'étude de la molécule isolée, en phase gazeuse, peut fournir une connaissance précise de ses propriétés chimiques et physiques intrinsèques. Cependant, lorsqu'on cherche à savoir comment les biomolécules interagissent avec leur environnement, l'étude de la molécule isolée n'est pas suffisante[1]. En effet, dans la nature, un solvant, généralement de l'eau, englobe les biomolécules, formant des liaisons hydrogène avec elles et modifiant ainsi leurs propriétés[2,3]. De plus, dans une cellule vivante, les biomolécules interagissent entre elles, modifiant ainsi leurs caractéristiques lors de leur interaction via des liaisons dites faibles (liaisons hydrogène, interactions de van der Waals).

Pour obtenir un système d'étude présentant les deux caractéristiques citées – un environnement solvaté et un groupe de molécules en forme d'agrégat, au sein duquel les molécules peuvent former des liaisons non covalentes – il existe deux principales méthodes. Ces méthodes consistent essentiellement en des techniques d'ionisation douce (telles que les sources d'ionisation électrospray[6]) pour les plus grosses molécules, et en des fours connectés à un système d'hydratation pour les plus petites[7]. En contrôlant l'environnement moléculaire, il est possible de réaliser l'étude dans une représentation simplifiée des conditions *in vivo*, tout en présentant les caractéristiques de base du milieu biologique.

Dans ce contexte, de nombreuses études ont été réalisées pour caractériser diverses catégories de biomolécules en phase gazeuse. Par exemple, de nombreuses études ont été consacrées à la caractérisation de petites

molécules telles que l'uracile[8], l'adénine et la glycine[9], pour ne citer que ces molécules.

Dans ce travail, nous prenons la molécule d'hypoxanthine (Figure 43) comme modèle de biomolécule. L'hypoxanthine est un dérivé de la purine, tout comme de nombreuses autres molécules bien connues, allant de l'adénine et de la guanine à la caféine et à la théobromine. Cette molécule joue divers rôles dans plusieurs processus biologiques[4]. Par rapport à l'adénine, elle se caractérise par la présence d'un seul substituant en position six (voir Figure 43). Étant donné qu'il s'agit de l'un des dérivés de la purine les moins étudiés, et compte tenu de sa polyvalence, nous visons à réaliser une étude systématique des caractéristiques de cette molécule. Plus précisément, l'objectif de ce travail est de comprendre si son mode de fragmentation ressemble d'une manière ou d'une autre à celui des purines formant l'ADN et l'ARN, d'examiner si cette molécule peut former des agrégats purs, d'avoir un aperçu des atomes impliqués dans leur formation, et de savoir si ces agrégats peuvent être solvatés, et comment ils le peuvent. En ce qui concerne la chimie moléculaire, l'objectif est de comprendre comment une complexité croissante de l'environnement moléculaire affecte les propriétés de chaque atome formant la molécule d'hypoxanthine.

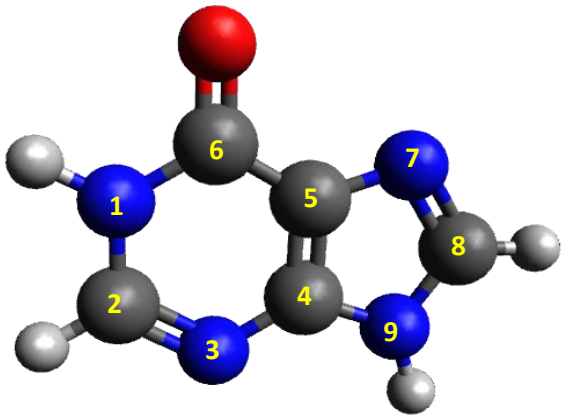

FIGURE 43: LA MOLÉCULE D'HYPOXANTHINE.

Pour obtenir ce type d'information, la technique la plus adaptée (et aussi celle employée dans ce travail) est basée sur la spectrométrie de masse.

Tout d'abord, cette technique permet d'obtenir des informations sur la stabilité de la biomolécule en analysant la formation d'éventuels agrégats, purs et hydratés. Le fait de disposer d'une complexité croissante de l'échantillon étudié permet de mieux comprendre comment chaque modification de l'environnement moléculaire peut effectivement changer les caractéristiques de la molécule étudiée. Deuxièmement, lorsqu'elle est couplée à des méthodes d'excitation telles que l'impact d'ions ou l'absorption de photons, la spectrométrie de masse peut être utilisée pour analyser les voies de fragmentation, nous fournissant ainsi des informations sur les différents processus d'interaction, tels que la capture d'électrons ou d'éjection d'atomes avec les ions, ou l'excitation résonante et l'ionisation avec les photons. D'autre part, si nous voulons obtenir des informations sur l'état chimique de la molécule, sur la façon dont la solvatation et la présence d'autres molécules liées par des liaisons hydrogène l'affectent, nous devons étudier l'état des électrons de cœur. Pour ce faire, la spectrométrie photoélectronique à rayons X est la technique la plus appropriée. En interprétant la variation des caractéristiques spectrales, nous pouvons observer comment l'environnement affecte les propriétés chimiques de notre échantillon.

7.1.2 DÉRIVÉS DE LA PURINE ET HYPOXANTHINE

Les purines partagent une structure de base constituée d'un cycle pyrimidine conjugué à un cycle imidazole. La présence de doubles liaisons multiples confère à la molécule une certaine stabilité thermique (par exemple, l'hypoxanthine présente un pic de décomposition thermique à 412 °C, l'adénine à 355 °C et la guanine à 512 °C[12]). Il peut y avoir une variété de substituants dans différentes positions sur les deux cycles, donnant aux molécules finales des propriétés différentes[13]. Même si la purine elle-même n'existe pas dans la nature, les dérivés de la purine jouent des rôles clés et divers dans plusieurs processus biologiques. Ils constituent le composant azoté de l'ADN et des différentes formes d'ARN, et sont donc fondamentaux pour la préservation, la transcription et la transmission de l'information génétique.

Structurellement, l'hypoxanthine est un dérivé de la purine, comme l'adénine et la guanine, de formule $C_5H_4N_4O$ et de masse molaire de 136,1115 g/mol. Cette molécule présente un substituant en position 6, qui est un atome d'oxygène. Sous cet aspect, elle est similaire à la guanine, qui présente en plus un groupe amine en position 2. Comme l'adénine, elle ne présente qu'un seul substituant dans la même position. Ainsi, compte tenu de ses caractéristiques, avec la présence d'un seul substituant en sixième position comme dans l'adénine, et le fait que ce substituant soit un atome d'oxygène comme pour la guanine, la molécule d'hypoxanthine présente des caractéristiques hybrides entre l'adénine et la guanine.

7.1.3 ÉTAT DE L'ART

Étant donné les rôles variés et essentiels joués par les dérivés de la purine, ils ont été largement étudiés dans divers domaines scientifiques allant des neurosciences, des études métaboliques, de la biochimie aux recherches en physique moléculaire. En particulier, l'étude en phase gazeuse de cette catégorie de molécules par des techniques spectrométriques et spectroscopiques permet d'explorer les propriétés intrinsèques tout en augmentant la complexité de l'environnement moléculaire de manière contrôlée. Comprendre ce qui arrive à ces molécules lors de l'interaction avec des photons ou des ions hautement chargés dans un environnement de plus en plus complexe est susceptible de donner accès aux événements se produisant lorsque la matière biologique est exposée à des radiations ionisantes[22]. Du fait que l'hypoxanthine présente des caractéristiques similaires aux deux purines formatrices d'ADN, l'étude de cette molécule en phase gazeuse constitue un domaine de recherche d'actualité.

Rappelons brièvement deux études réalisées précédemment par Dawley *et al.*[31], ainsi que celle de Feyer *et al.* [32]. Dans les premiers travaux, le spectre de photodissociation a été obtenu à 70 eV[31]. De leur côté, Feyer *et al.* ont enregistré des spectres de masse aux énergies correspondant aux niveaux de valence de l'hypoxanthine. Les deux études ont présenté des caractéristiques communes, comme par exemple le pic de l'ion parent de masse-sur-charge m/z = 136 (m étant le nombre de nucléons et z le degré

d'ionisation), l'ion fragment $C_4H_4N_4^+$ de m/z = 108 après la perte de HCNH, le fragment complémentaire $HCNH^+$ de m/z = 28, et les fragments de m/z = 54 et 53 représentant respectivement $C_2H_2N_2^+$ (ou le fragment C_2NO^+) et $C_2HN_2^+$.

En ce qui concerne les spectres de photoémission de la molécule, nous pouvons mentionner les travaux réalisés par Feyer *et al.*[32] pour les spectres de photoémission (PES), et ceux de Plekan *et al.*[33] pour les spectres de photoélectrons X (XPS). Les résultats de ces travaux sont discutés plus en profondeur dans le chapitre dédié aux résultats de ce travail (Chap. 5).

7.1.4 OBJECTIF DE LA PRÉSENTE ÉTUDE

Comme nous l'avons vu, l'hypoxanthine peut être utile pour étudier les propriétés similaires à la guanine dans une phase gazeuse, tout en restant une molécule intéressante en soi et que l'on retrouve dans différents environnements. Pour ces raisons, on s'attend à ce que l'obtention d'informations supplémentaires sur le comportement de cette molécule dans des environnements de plus en plus complexes, à savoir dans des agrégats purs et dans des agrégats hydratés, soit utile pour une compréhension plus complète des effets des dommages causés par les radiations dans la matière vivante. Dans ce contexte, nous cherchons à répondre aux questions les plus urgentes suivantes :

- Que se passe-t-il lorsque les agrégats d'hypoxanthine interagissent avec des ions multichargés ou des photons ?
- Existe-t-il une différence entre la fragmentation de l'agrégat pur et celle de l'agrégat hydraté, en utilisant des photons ou des ions ?

7.1.5 INTRODUCTION AUX MÉTHODES EXPÉRIMENTALES ADOPTÉES

7.1.5.1 SPECTROMÉTRIE DE MASSE COUPLÉE À L'IMPACT D'IONS

Une part importante des expériences menées dans ce travail a été réalisée au moyen de la collision de l'hypoxanthine, dans différents états d'agrégation, avec des ions multichargés. Lors de l'interaction, en fonction

de la vitesse relative entre l'ion projectile et les électrons cibles impliqués dans l'interaction, l'un des trois processus suivants peut survenir : l'excitation, la capture d'électrons ou l'ionisation.

L'installation avec laquelle nous avons réalisé les expériences au moyen des ions multichargés délivre des ions de faible énergie (< 20 keV/nucléon). Ainsi, le processus dominant est la capture électronique. Il faut néanmoins mentionner que les phénomènes d'ionisation et d'excitation ont également lieu, bien que moins probables.

Après la collision, la molécule cible devient chargée et excitée. Deux issues sont prévisibles. Soit la molécule stabilise et évite la dissociation en dissipant l'énergie interne dans ses modes vibrationnels et rotationnels, produisant ainsi une molécule ionisée intacte ; soit la molécule se dissocie en fragments neutres et/ou chargés en raison de l'excès d'énergie interne et/ou de la répulsion coulombienne entre les charges.

Dans ce travail, l'étude de la fragmentation des ions moléculaires doublement chargés est réalisée grâce à la spectrométrie de masse en coïncidence. Avec cette technique, il est possible de collecter simultanément tous les produits chargés obtenus par la dissociation d'un dication spécifique. Cette méthode facilite également la reconstruction des mécanismes de dissociation qui ont donné naissance aux fragments chargés. Le principe de l'acquisition d'un spectre de masse en coïncidence consiste en l'enregistrement de deux particules chargées provenant d'une même molécule. Visuellement, la corrélation entre deux fragments provenant d'une même molécule est représentée par un îlot de coïncidence sur la carte dite de coïncidence, mettant en relation les temps de vol (TOF) des deux fragments chargés (TOF1 et TOF2), mettant ainsi en relation le fragment le plus lourd et le fragment le plus léger provenant de la même molécule. Les îlots de coïncidence peuvent fournir des informations sur la nature des différentes voies de fragmentation et, de manière assez intéressante, la forme de chaque îlot donne des informations sur le processus spécifique impliqué dans la production des fragments détectés (voir Chapitres 3 et 5).

7.1.5.2 SPECTROMÉTRIE DE MASSE COUPLÉE À L'IONISATION PAR PHOTONS

Une autre méthode d'excitation utilisée dans ce travail est la photoionisation VUV, avec une énergie de photons de 9,5 eV. L'avantage d'utiliser des photons pour réaliser la spectrométrie de masse réside dans le fait que l'énergie déposée sur la molécule cible peut être contrôlée et mesurée avec précision[40,41]. Comme dans le cas du projectile ionique, la molécule ionisée peut se dissocier de telle sorte que les produits chargés peuvent être analysés par spectrométrie de masse.

Dans ce travail, seuls les spectres de masse à une énergie de photon donnée, au-dessus du seuil d'ionisation, ont été considérés.

7.1.5.3 SPECTROMETRIE PHOTOÉLECTRONIQUE INDUITE PAR RAYONS X

Le principe de la spectrométrie photoélectronique X (XPS) consiste à focaliser des rayons X sur l'échantillon, afin d'éjecter des électrons de cœur des atomes. En analysant le nombre et l'énergie des électrons émis, il est possible d'obtenir des informations sur la composition de l'échantillon, sur son état chimique, son environnement moléculaire et sa structure électronique[40].

Une caractéristique importante à laquelle les spectres XPS donnent accès est le « déplacement chimique ». Bien que les électrons directement impliqués dans la formation des liaisons covalentes soient ceux de valence, les électrons de cœur sont aussi affectés par une variation de l'environnement chimique, en subissant une variation d'énergie de liaison, variation qui est définie comme étant le déplacement chimique[42]. Par exemple, si l'on considère l'atome de carbone, son énergie de liaison en couche K est comprise entre 285 et 300 eV, selon son environnement chimique : lorsqu'il est lié à l'oxygène pour former du CO_2, cette énergie vaut 298 eV, alors que lorsqu'il est impliqué dans la molécule de méthane, CH_4, elle est de 290,7 eV. L'explication réside dans le fait que, lorsque l'atome est lié à des éléments présentant une électronégativité plus élevée, la valeur de l'énergie de liaison des électrons augmente, puisque la charge d'écrantage de l'atome est diminuée par rapport à sa forme libre. Lorsque l'atome est lié à des éléments moins électronégatifs, l'écrantage devient

plus fort et l'énergie de liaison diminue. Le déplacement chimique fournit des informations importantes sur l'état électronique du système étudié. De plus, le déplacement chimique est souvent associé à la nature des interactions de l'atome considéré avec son environnement atomique et moléculaire, selon que cet atome subit principalement des interactions non covalentes (liaisons hydrogène et interactions de Van der Waals) ou plutôt des interactions covalentes[42].

Pour enregistrer l'énergie cinétique des électrons éjectés, nous avons utilisé l'analyseur électrostatique hémisphérique installé sur la ligne de faisceau PLEIADES (Figure 44). Ce système a une structure compacte et correspond au système d'analyse XPS le plus couramment utilisé[40].

Après avoir traversé l'analyseur, les électrons sont détectés au moyen d'un multiplicateur d'électrons. Les principaux multiplicateurs sont le channeltron et les détecteurs à micro-canaux (MCP). Le montage utilisé emploie un détecteur MCP.

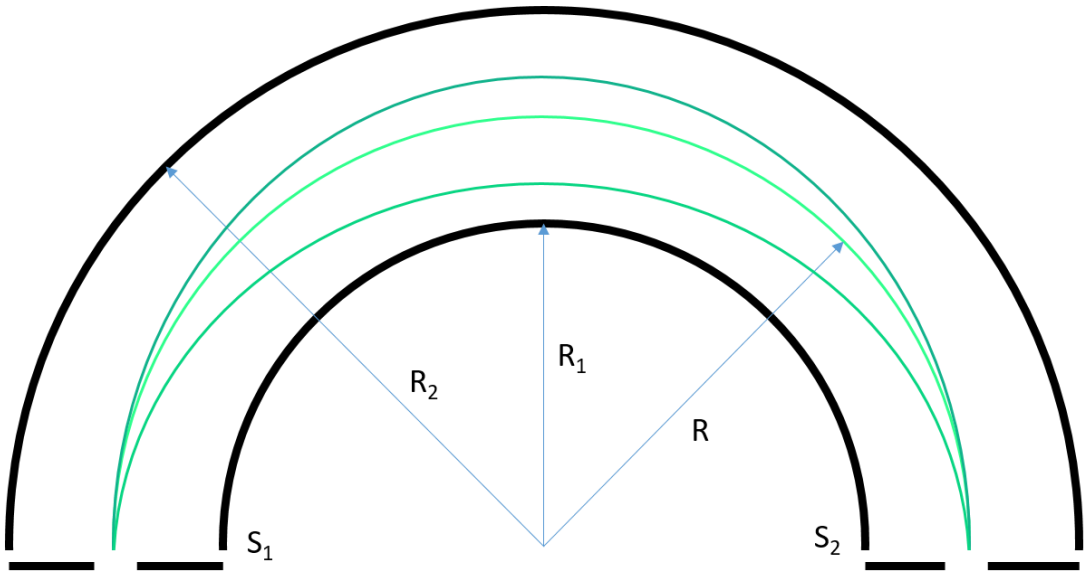

FIGURE 44: REPRÉSENTATION SCHÉMATIQUE D'UN ANALYSEUR HÉMISPHÉRIQUE. S1 ET S2 SONT RESPECTIVEMENT LES FENTES D'ENTRÉE ET DE SORTIE DE L'ANALYSEUR. LES TRAJECTOIRES DESSINÉES N'ONT QU'UN BUT ILLUSTRATIF.

7.1.6 COMPLÉMENTARITÉ DES DIFFÉRENTES APPROCHES EXPÉRIMENTALES

Les méthodes employées, à savoir la spectrométrie de masse, couplée à la fragmentation induite par les ions ou à la photoabsorption VUV, et la spectroscopie de photoélectrons X, fournissent chacune un éventail différent d'informations qui, ensemble, peuvent contribuer à une description plus complète des propriétés d'un agrégat moléculaire d'hypoxanthine. Grâce à la spectrométrie de masse, nous pouvons obtenir des informations telles que les liaisons les plus faibles en analysant la fragmentation de la molécule isolée, ou encore les atomes impliqués dans la formation des liaisons hydrogène en observant la fragmentation des agrégats purs et hydratés. Ainsi, avec la spectrométrie de masse, nous pouvons obtenir des informations sur la structure géométrique et la stabilité de la molécule. Avec la spectrométrie XPS, les informations obtenues résident dans la caractérisation de chaque élément composant la molécule, en particulier leur structure électronique en fonction de leur environnement atomique et moléculaire. En mettant en relation les différentes informations obtenues par ces différentes approches expérimentales, nous pouvons obtenir une image assez complète de la façon dont la complexité croissante de l'environnement chimique affecte la stabilité moléculaire de l'hypoxanthine, c'est-à-dire sa capacité à résister aux rayonnements ionisants. Ce type d'information peut être utile lorsqu'on examine comment les fragments moléculaires agissent dans un environnement biologique normal, et si l'environnement aqueux peut contribuer à atténuer la production d'espèces réactives.

7.2 DISPOSITIFS EXPÉRIMENTAUX

Au cours de ce projet, les expériences ont eu lieu sur deux installations différentes : auprès de l'installation COLIMACON de la plateforme ARIBE sur le site du GANIL à Caen ; et auprès de deux lignes de lumière, PLEIADES et DESIRS, du synchrotron SOLEIL à Gif-sur-Yvette. Ces deux installations utilisent des moyens d'investigation très différents : alors qu'à

ARIBE, le faisceau est composé d'ions, à SOLEIL il s'agit d'un faisceau de photons.

7.2.1 SOURCES DES ESPÈCES CIBLES

Au cours de cette thèse, nous avons utilisé deux types de sources de faisceaux moléculaires : l'une pour la production d'un faisceau de molécules neutres isolées, et l'autre pour la production d'agrégats de molécules neutres. La source de molécules isolées n'a été utilisée que sur le dispositif COLIMACON, tandis que la source d'agrégats a été utilisée aussi bien pour des expériences menées sur le dispositif COLIMACON auprès de la ligne de faisceau ARIBE du GANIL que pour celles effectuées sur les lignes de lumière DESIRS et PLEIADES au synchrotron SOLEIL.

La source de molécules isolées consiste en un four constitué de la superposition de deux cylindres creux en molybdène (voir Figure 45). Le premier est un réservoir d'un diamètre intérieur de l'ordre du centimètre. Préalablement à l'expérience, il est rempli de la poudre d'hypoxanthine. Le second cylindre consiste en une cavité de quelques millimètres de diamètre, et constitue le canal par lequel les molécules isolées sont éjectées. Un fil chauffant thermocoax, capable de produire efficacement une chaleur homogène, entoure ces deux éléments du four. Dans le cas de l'hypoxanthine, la température à atteindre est de l'ordre de 190 °C. Une fois que la poudre vaporisée sort du four, elle produit un jet conique divergent. Afin d'obtenir un faisceau moléculaire plus collimaté, le jet passe à travers un diaphragme de 0,53 cm de diamètre, placé 7 cm après le four, et 10 cm avant la zone d'interaction. On obtient ainsi une densité cible de 10^8-10^9 molécules/cm^3.

Le principe qui sous-tend la conception d'une source d'agrégation basée sur l'éjection de l'échantillon sous forme gazeuse par chauffage du creuset est similaire à celui utilisé pour la production du faisceau de molécules isolées. Ici, l'utilisation d'un gaz tampon est nécessaire pour favoriser le processus d'agrégation. La Figure 46 décrit schématiquement la source d'agrégats CELENO utilisée lors des expériences menées au synchrotron

SOLEIL. Le processus exploité dans ce type de source d'agrégats est l'attachement d'une nouvelle molécule au monomère grâce à la collision entre les deux molécules[43,52]. Le gaz tampon, tel que l'hélium ou l'argon, absorbe l'excès d'énergie produit par la formation des liaisons intermoléculaires non covalentes (ce qui donne à l'ensemble du processus le nom de collisions à trois corps).

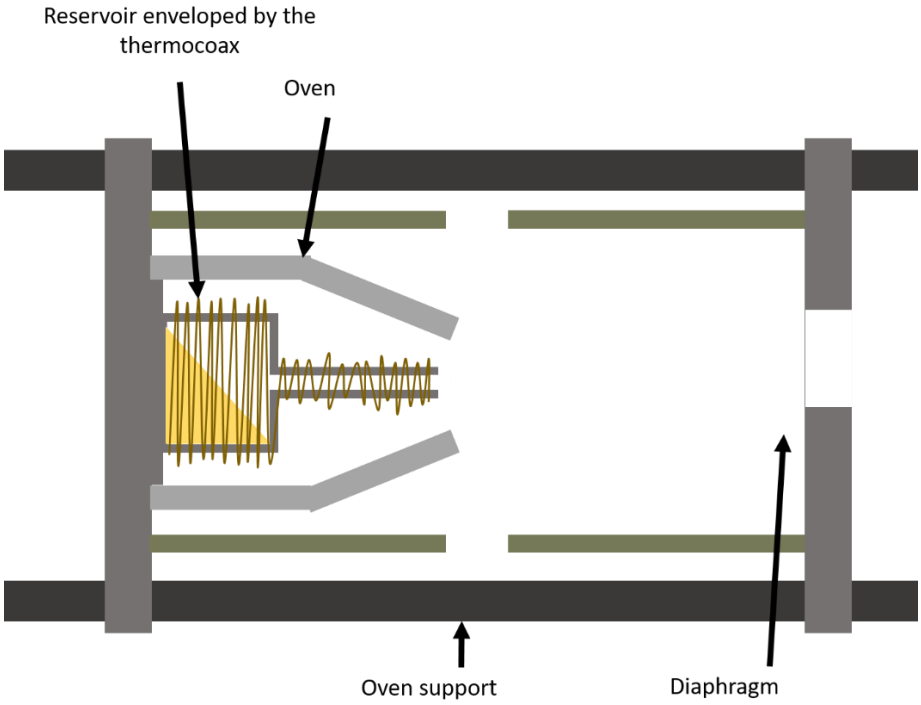

FIGURE 45: REPRÉSENTATION SCHÉMATIQUE DE LA SOURCE DE MOLÉCULES ISOLÉES. ON PEUT OBSERVER LE RÉSERVOIR ENTOURÉ PAR LE THERMOCOAX, PLACÉ DANS LE FOUR. CELUI-CI EST ENSUITE PLACÉ DANS LE SUPPORT POUR ÊTRE MONTÉ SUR LE DISPOSITIF COLIMACON.

Afin de maintenir les agrégats formés et d'éviter leur dissociation, la température à laquelle l'agrégation a lieu doit être suffisamment basse, en la maintenant aux alentours de -185 °C. Pour atteindre cette température, la formation de l'agrégat a lieu dans une partie dédiée, appelée canal de condensation, constituée d'un conduit à double paroi dans lequel circule de l'azote liquide (LN2), réfrigérant ainsi le système. Les collisions du gaz tampon avec les parois froides du canal permettent aux agrégats formés d'atteindre un équilibre thermique à la sortie de la source.

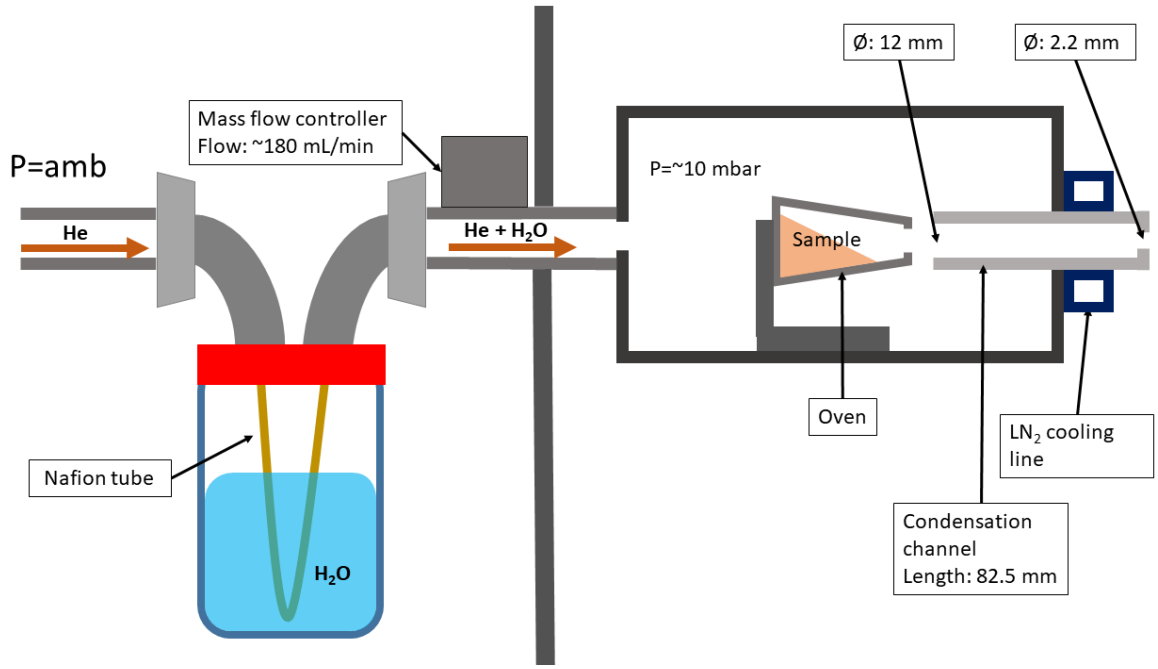

FIGURE 46: REPRÉSENTATION SCHÉMATIQUE DE LA SOURCE D'AGRÉGATS GAZEUX CELENO, ÉQUIPÉE POUR PRODUIRE DES AGRÉGATS HYDRATÉS. LA CHAMBRE DE LA SOURCE D'AGRÉGATS A UN DIAMÈTRE DE 140 MM ET UNE HAUTEUR DE 90 MM.

La conception des sources d'agrégats utilisées dans ce travail est basée sur celle de Bergen[53], qui est une adaptation de celle conçue par Bréchignac[54] (Figure 46). La source utilisée est composée d'une chambre en acier inoxydable présentant un diamètre de 140 mm pour une hauteur de 90 mm et d'un plateau mobile qui permet de positionner le four au centre. La chambre est maintenue sous vide. Elle présente deux ouvertures sur ses côtés opposés : l'une pour laisser le passage de la ligne de gaz tampon et l'autre pour accueillir le canal de condensation qui laisse sortir les molécules et les agrégats dans la chambre d'interaction. Le débit du gaz tampon, de l'hélium dans le cas de nos expériences, était généralement maintenu à 150-200 mL/min. La pression d'hélium à l'intérieur de la chambre source est maintenue à environ 10 mbar. Le four, dans lequel la poudre d'hypoxanthine est disposée consiste en un cylindre en acier inoxydable d'une capacité de 3 cm^3, entouré d'un fil résistif chauffant. La température du four est enregistrée et contrôlée par un thermocouple placé contre sa paroi du fond. Afin de contrôler la croissance des agrégats, nous

pouvons régler plusieurs paramètres de la source d'agrégats, allant du four jusqu'au canal de condensation[44]. Le premier paramètre qui peut être ajusté est la température du four, régulée par le courant passant à travers l'élément chauffant l'entourant. En augmentant la température, la pression de vapeur de l'échantillon augmente également, ce qui augmente le flux de molécules éjectées du creuset. Le deuxième paramètre qui peut être régulé concerne les propriétés du gaz tampon. L'élément utilisé comme gaz tampon et sa pression affectent la croissance des agrégats. Notamment, la pression contrôle le nombre de collisions dans le canal de condensation.

L'hélium a été choisi comme gaz porteur dans nos expériences. En utilisant ce gaz, nous avons pu obtenir des agrégats contenant de l'ordre de quelques dizaines de molécules. Des agrégats plus gros n'étaient pas d'un intérêt primordial dans le présent travail, puisque le but de l'expérience était de vérifier si la production d'agrégats purs et hydratés était réalisable ou non. Comme mentionné, la croissance des agrégats a été contrôlée grâce à la variation de deux paramètres : la température du four et le débit du gaz tampon.

La production des agrégats hydratés a été réalisée selon la procédure conçue par Kocisek *et al.*[55]. Cette méthode repose sur l'hydratation du gaz tampon avant son entrée dans la source d'agrégats. Pour ce faire, on laisse passer la conduite de gaz porteur à travers une coupelle fermée remplie d'eau ultra pure (MilliQ). En traversant un canal poreux perméable à l'eau (Nafion®), le flux gazeux est capable d'absorber des molécules d'eau. En modifiant la surface du tube en contact avec l'eau, nous avons pu obtenir différents niveaux d'hydratation lors de la production des agrégats.

7.2.2 DISPOSITIFS POUR LES EXPÉRIENCES AVEC LES IONS

En ce qui concerne les expériences avec les ions multichargés, le premier dispositif à décrire est le système COLIMACON ("COLlision entre des Ions et des Molécules ou des Agrégats COmplexes Neutres"). Ce dispositif est

installé au niveau de la plateforme ARIBE ("Accélérateur pour la Recherche sur les Ions de Basse Énergie") de l'installation GANIL ("Grand Accélérateur National d'Ions Lourds"). Comme le montrent les acronymes, ce dispositif est dédié à l'interaction entre des ions multichargés de faible énergie (< 20 keV/nucléon) et des molécules neutres (ou des agrégats moléculaires) en phase gazeuse.

La plateforme ARIBE comporte une source d'ions à résonance cyclotronique électronique (ECR), qui produit des ions multichargés A^{q+} de faible énergie (5-20 keV par unité de charge)[56].

Le dispositif COLIMACON consiste en un spectromètre à temps de vol (TOF) à faisceaux croisés dans lequel le faisceau moléculaire, produit comme décrit dans les paragraphes précédents, croise le faisceau d'ions projectiles, comme le montre la Figure 47. Lors de l'interaction, les produits de fragmentation sont analysés en fonction de leur rapport masse/charge m/z, soit sous forme de spectre de masse simple, soit en coïncidence, afin de comprendre le phénomène conduisant à la formation des fragments observés.

Le spectromètre de masse est composé de trois parties : une zone d'extraction où se produit l'interaction susmentionnée, la zone de vol libre et la zone de détection :
La zone d'extraction est celle où a lieu la collision entre la cible et le faisceau projectile. Ici, les produits chargés nouvellement formés sont extraits par champ électrique vers la zone de temps de vol. Cette zone est divisée en deux parties, selon le principe de Wiley-McLaren, afin de focaliser dans le temps les fragments chargés dans le plan de la zone de détection, augmentant ainsi la résolution massique du spectromètre[58]. La zone de détection est celle où les produits chargés arrivent après avoir traversé le tube à temps de vol et où ils sont traités par un détecteur de type Daly[53,59,60].

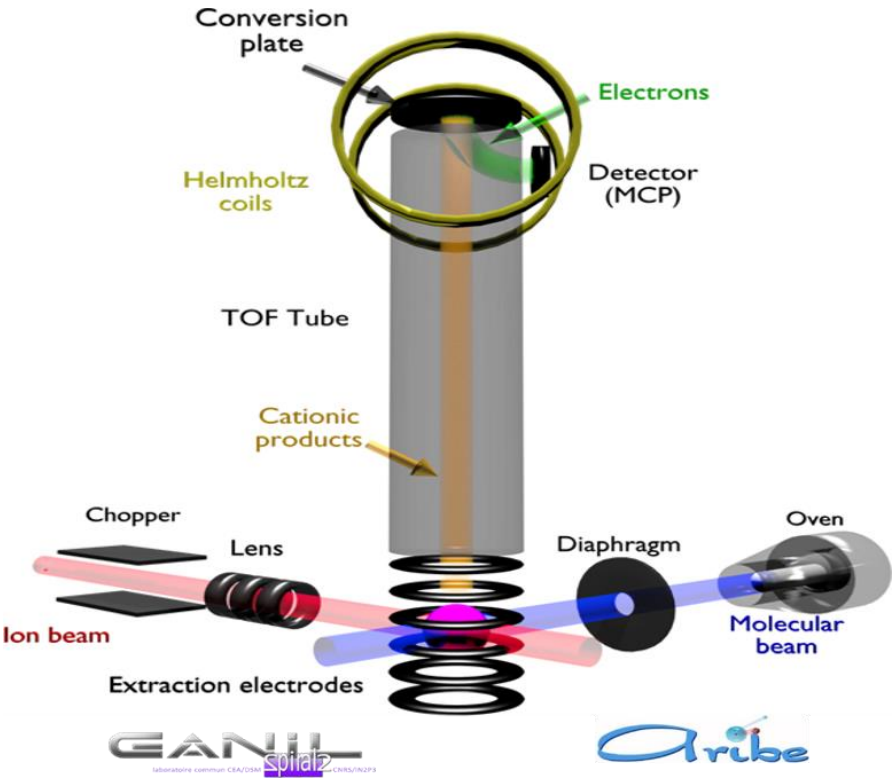

FIGURE 47: REPRÉSENTATION SCHÉMATIQUE DU DISPOSITIF COLIMACON.

7.2.3 DISPOSITIFS POUR LES EXPÉRIENCES AVEC LES PHOTONS

Le synchrotron SOLEIL est l'installation au sein de laquelle se sont déroulées nos expériences utilisant des photons. SOLEIL ("Source Optimisée de Lumière d'Énergie Intermédiaire du LURE") appartient à la troisième génération de synchrotrons avec une énergie de 2,75 GeV, ce qui permet de couvrir la gamme d'énergie allant de l'infrarouge aux rayons X durs[61,62]. Il comporte 29 lignes de faisceaux, chacune axée sur des gammes d'énergie spécifiques, et donc dédiée à des dispositifs expérimentaux, des types d'échantillons et des états d'agrégation spécifiques.

Les expériences XPS réalisées dans le cadre de ce travail ont eu lieu sur la ligne de lumière PLEIADES de SOLEIL, qui est dédiée à l'étude de la matière diluée, à savoir des échantillons gazeux en utilisant des photons dans la gamme des rayons X mous. La ligne de lumière PLEIADES couvre la gamme d'énergie entre 10 et 1000 eV[63,64]. Afin de mesurer les spectres

photoélectroniques induits par les rayons X, nous avons utilisé la station finale de l'analyseur d'énergie électronique hémisphérique VG Scienta R4000 couplée à la chambre de la source polyvalente (MPSC)[63]. La source d'agrégats CELENO a été installée à l'intérieur de la MPSC (Figure 48). La pression dans la MPSC est maintenue à quelques 10^{-5} mbar. La pression de travail dans la chambre d'interaction est généralement comprise entre 10^{-6} mbar et 10^{-5} mbar, avec une pression résiduelle de 10^{-8} mbar.

L'analyseur Scienta est un spectromètre disponible dans le commerce, conçu spécifiquement pour la mesure de l'énergie des photoélectrons. La gamme d'énergie garantie pour les expériences XPS est comprise entre 5 et 1500 eV.

Ici, le détecteur consiste en deux galettes à microcanaux (MCP) qui permettent d'obtenir jusqu'à 10^6 électrons secondaires par électron détecté. Les deux MCPs sont placées juste devant un écran fluorescent au phosphore qui est placé devant une caméra CCD. Ainsi, lorsque les électrons frappent l'écran, ils produisent un flash lumineux, qui est enregistré par la caméra. Ainsi, en fonction de la position des spots sur l'image, on peut extrapoler des informations concernant les distributions énergétique et angulaire des photoélectrons.

La ligne de lumière DESIRS fournit un rayonnement VUV intense de polarisation linéaire ou circulaire entièrement contrôlable dans la gamme d'énergie de photons comprise entre 4 et 40 eV[65]. Ce monochromateur est équipé de différents réseaux, qui assurent un réglage fin de l'énergie du faisceau et de la résolution en énergie. Dans le cadre de cette thèse, nous avons choisi une résolution modérée d'environ~ 10 meV pour une énergie photonique de 10 eV. Ce réglage assure un flux assez élevé, de l'ordre de quelques 10^{12} photons.sec^{-1}. La source de clusters CELENO décrite au paragraphe précédent a été couplée à la « chambre à faisceau moléculaire permanente » SAPHIRS[66] équipée du spectromètre DELICIOUS 3[67] (Figure 49) à double imagerie de coïncidence photoélectron/photoion (i2PEPICO), installé en permanence sur la branche A de la ligne de faisceau. Le spectromètre DELICIOUS 3 permet la détection en coïncidence des photoions et des photoélectrons produits lors de chaque événement de

photoionisation. Les photoélectrons sont détectés par un spectromètre VMI (velocity map imaging), permettant la détermination de leur énergie cinétique et de leurs distributions angulaires, après inversion d'Abel des images enregistrées.

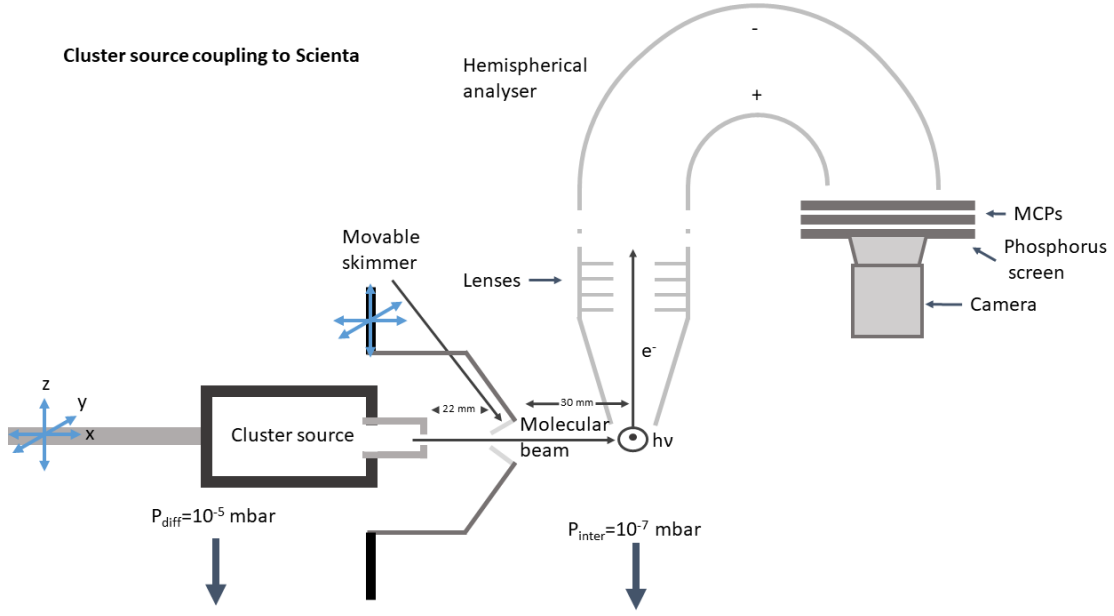

FIGURE 48: REPRÉSENTATION SCHÉMATIQUE DU COUPLAGE DE LA SOURCE D'AGRÉGATS CELENO AU SPECTROMÈTRE SCIENTA DANS PLEIADES.

Comme le montre la Figure 49, le côté ionique du spectromètre consiste en un spectromètre de masse à temps de vol de type Wiley-McLaren modifié. Les photoions sont extraits perpendiculairement à la direction du faisceau moléculaire. Une électrode déflectrice dans le tube de vol d'ions permet de s'assurer que les ions lourds ayant une grande impulsion initiale dans la direction du faisceau moléculaire atteignent également le détecteur sensible en position (PSD) de 40 mm de diamètre et équipé de MCP. Dans le spectromètre DELICIOUS 3, les ions sont accélérés à ~ 3800 V.

Comme mentionné, la source d'agrégats CELENO a été placée dans la chambre SAPHIRS. Le faible vide présent dans la chambre de la source n'entraîne qu'une faible augmentation de pression dans l'étage de pompage différentiel (10^{-6} mbar), et une augmentation de pression négligeable dans la chambre du spectromètre (environ 10^{-8} mbar).

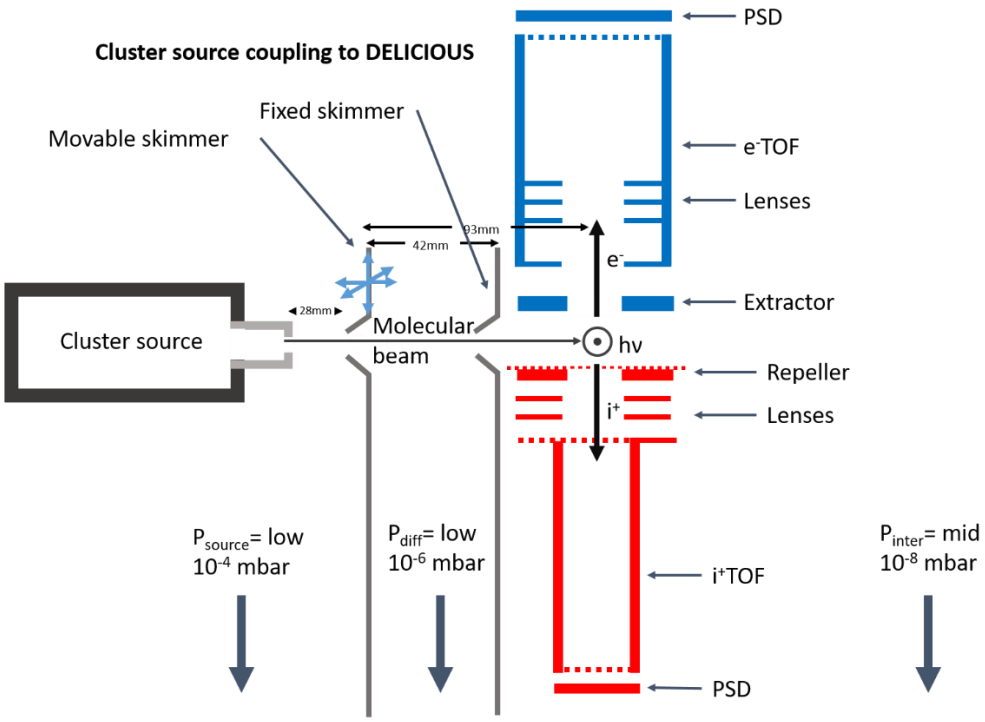

FIGURE 49: REPRÉSENTATION SCHÉMATIQUE DE LA SOURCE D'AGRÉGATS CELENO COUPLÉE AU SPECTROMÈTRE DELICIOUS 3 DE LA LIGNE DE FAISCEAU DESIRS.

7.3 RÉSULTATS ET DISCUSSION

Comme expliqué précédemment, le but de ce travail est d'étudier les effets de l'hydratation sur la stabilité de la molécule d'hypoxanthine lors de l'irradiation. L'approche employée ici consiste à faire varier le nombre de molécules d'eau attachées aux molécules d'hypoxanthine et à étudier la variation résultante de leurs propriétés physico-chimiques. Dans le cas de la spectrométrie de masse induite par les ions, nous avons réalisé des expériences en commençant par la molécule isolée, puis par des agrégats purs, et enfin hydratés, afin d'observer si la formation de liaisons non covalentes peut affecter la stabilité du système moléculaire après irradiation. Par contre, lors de nos expériences XPS, les caractéristiques de la molécule isolée n'ont pas été étudiées puisque les données obtenues par Plekan *et al.*[33] étaient déjà disponibles. Nos expériences XPS n'ont donc impliqué que des agrégats purs et hydratés.

7.3.1 CARACTÉRISATION DES SOURCES D'AGRÉGATS

L'expérience réalisée sur la ligne de lumière DESIRS nous a permis de caractériser la source d'agrégats CELENO et nous a fourni des informations concernant le réglage fin de la source d'agrégats pour la production d'agrégats de diverses caractéristiques[77]. Les paramètres contrôlant la distribution de taille des agrégats sont le flux du gaz tampon d'hélium (He_{flow}) et la pression associée (He_p) à l'intérieur du canal de condensation de la source d'agrégats, ainsi que la pression de vapeur de l'hypoxanthine qui est contrôlée par la température du four (T_{oven}), et la température du canal de condensation (T_{cc})[44]. Pendant les expériences, nous avons maintenu la température T_{cc} constante à la température de LN_2, tout en ajustant les paramètres He_{flow} et T_{oven}. Dans le cadre de ce travail, seules les données concernant la variation de la température du four sont présentées. Ce choix a été fait pour assurer une certaine cohérence au niveau des paramètres entre les données obtenues pour les agrégats purs et les agrégats hydratés. En effet, les deux séries de données présentées dans ce travail ont été collectées à la même énergie de photon (9.5 eV) et avec le même débit He_{flow} (180 mL/min). L'énergie des photons a été choisie égale à 9,5 eV car, selon la littérature, l'énergie d'ionisation du monomère d'hypoxanthine est de 8,85 eV[32], bien en dessous de 9,5 eV.

La discussion sur les variations de la distribution de la taille des agrégats en fonction de la température du four est basée uniquement sur les données recueillies pour des agrégats purs d'hypoxanthine (Figure 50).

Les spectres de masse VUV enregistrés à l'énergie photonique de 9,5 eV pour la croissance des agrégats purs sont présentés dans la Figure 50 pour différentes conditions de source d'agrégats. La distribution générale de la taille des agrégats suit une tendance log-normale et son maximum et sa largeur dépendent des paramètres de la source d'agrégats. Les agrégats observés correspondent principalement aux espèces cationiques $(Hyp)_n^+$. Cependant, la faible contribution isotopique due au ^{13}C dans les plus gros agrégats ne peut expliquer la forte intensité des pics de $(Hyp_n+1)^+$ observée dans les spectres de masse, à partir du dimère. Cela suggère que des

agrégats protonés sont également présents. Les agrégats protonés sont des produits de la dissociation partielle d'agrégats plus gros, suite à la photoionisation. En effet, l'observation d'espèces protonées est généralement associée à la dissociation des agrégats. Néanmoins, comme le signal de protonation est plutôt faible pour une énergie de photon égale à 9.5 eV et que la distribution de taille observée suit une tendance log-normale, nous supposons que la fragmentation des agrégats est en grande partie limitée, et donc, que la distribution de taille observée reflète assez bien la distribution de tailles initiale dans les présentes conditions d'ionisation. Toutefois, il convient de noter que l'efficacité de détection des plus gros agrégats est quelque peu réduite en raison de la dépendance en masse de l'efficacité du détecteur à microcanaux dans cette gamme de masse (voir détails expérimentaux). Par conséquent, la distribution de tailles réelle est légèrement décalée vers les plus grandes tailles.

Pour le spectre de la Figure 50 a), les paramètres de la source étaient 491 K pour la température du four et 180 mL/min pour le débit du gaz tampon. La distribution log-normale présente un maximum correspondant au pentamère (m/z = 680), et la taille maximale observée pour les agrégats correspond à n ~ 11 molécules. Les signaux associés à la molécule d'hypoxanthine et à son dimère sont plutôt intenses dans ces conditions de source. Leurs intensités relatives diminuent lorsque l'on augmente la température du four de 491 K à 498 K (Figure 50 b) et à 505 K (Figure 50 c). Le monomère n'est pas visible dans le spectre de masse enregistré à cette dernière température. Dans les spectres recueillis à 491 K et 498 K, le signal du dimère correspond à un pic intense (le plus intense à 491 K), ce qui signifie que le dimère peut être considéré comme très stable, représentant ainsi un nombre dit « magique » (n = 2). Dans la Figure 50 c), où la température du four a été augmentée à 505 K, nous remarquons clairement un nouveau déplacement de la distribution de taille des agrégats vers des m/z plus élevés. La distribution log-normale a maintenant un maximum plat entre l'hexamère (m/z = 816) et le décamère

(m/z = 1360) et présente des intensités relatives plus élevées pour les plus grandes tailles d'agrégats, jusqu'à m/z ~ 3000.

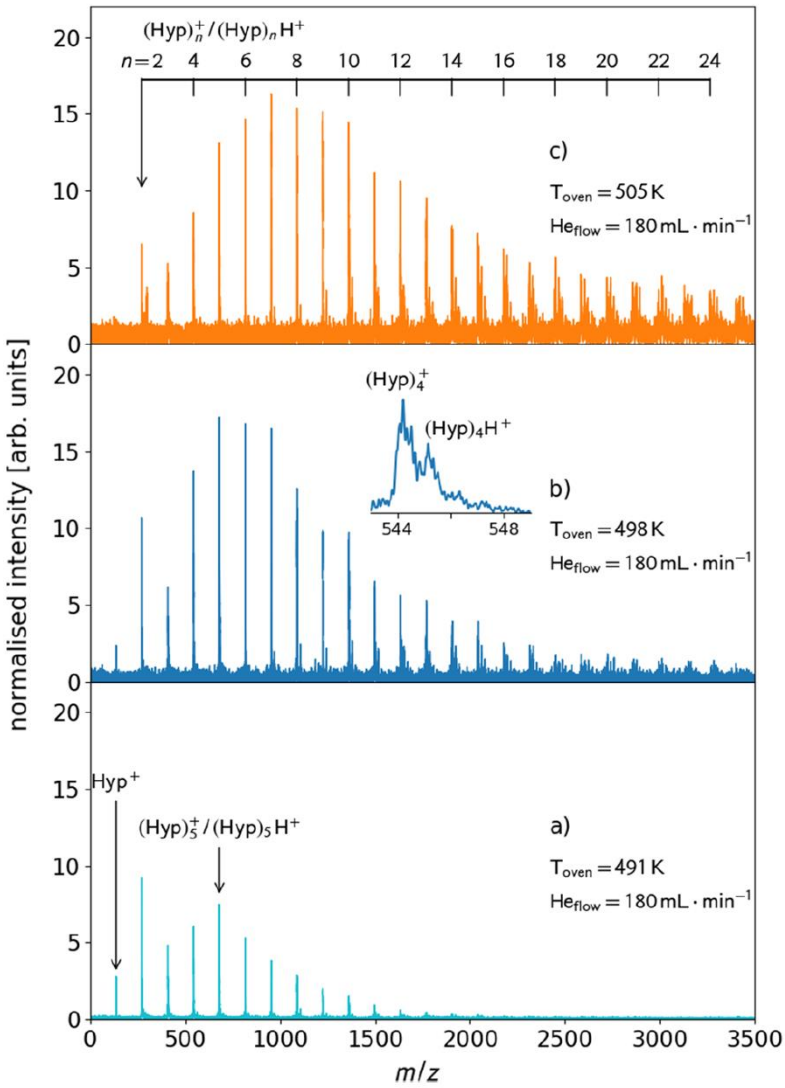

FIGURE 50: COMPARAISON DES SPECTRES DE MASSE DES AGRÉGATS D'HYPOXANTHINE À DIFFÉRENTES TEMPÉRATURES DE FOUR, SUITE À LA PHOTOIONISATION À 9,5 EV. DANS LE PANEL A) LA TEMPÉRATURE EST LA PLUS BASSE, À 491 K ; DANS LE PANEL B) ELLE EST DE 498 K ; ET DANS LE C) ELLE EST DE 505 K. TOUS LES SPECTRES ONT ÉTÉ ACQUIS AVEC LE MÊME FLUX DE GAZ D'HÉLIUM. (FIGURE EXTRAITE DE L'ARTICLE CITÉ EN RÉF. 77).

Nous examinons maintenant comment utiliser la source d'agrégats CELENO pour réguler le niveau d'hydratation des agrégats d'hypoxanthine hydratés. Comme déjà mentionné, la production d'agrégats hydratés repose sur l'utilisation d'une membrane Nafion®. La régulation du niveau

d'hydratation des agrégats est possible grâce à la variation de la surface du tube Nafion® en contact avec l'eau liquide. La Figure 51 montre deux spectres de masse enregistrés avec différents niveaux d'humidification du gaz tampon. Pour observer comment le niveau d'humidification affecte la formation et la distribution de taille des agrégats, nous avons fixé l'énergie des photons à 9,5 eV (la même que celle utilisée pour collecter les données avec les agrégats purs à différentes températures de four).

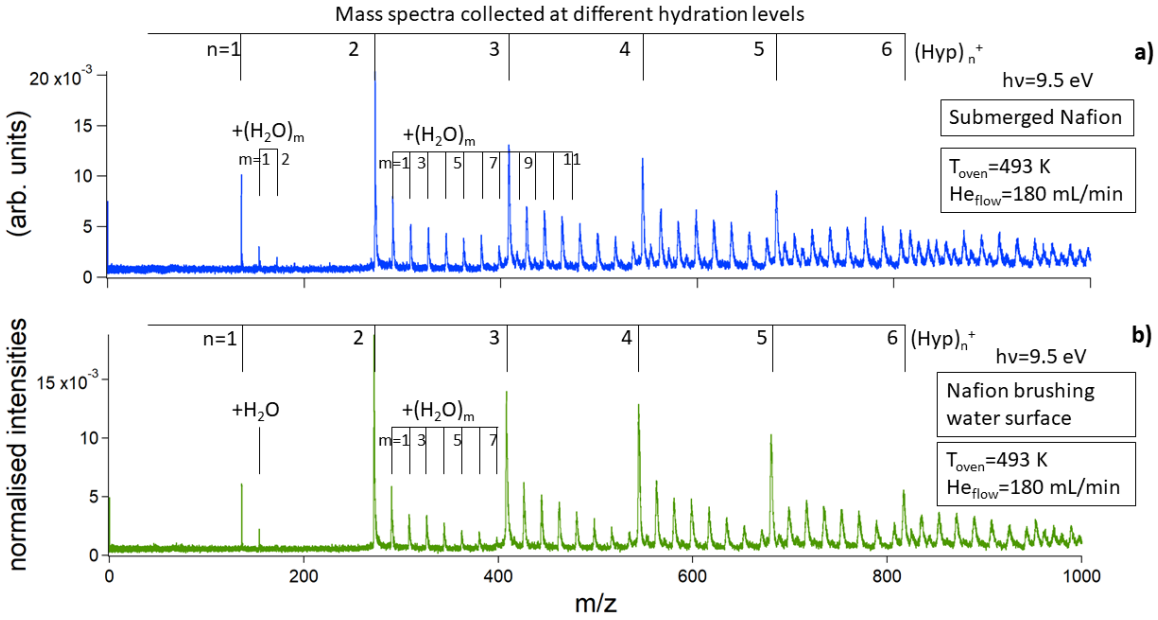

FIGURE 51: COMPARAISON DU NIVEAU D'HYDRATATION RÉGULÉ PAR LA SURFACE DU NAFION® EN CONTACT AVEC L'EAU. DANS LE PANEL A) LE NAFION® EST IMMERGÉ, ET DANS LE PANEL B) IL NE FAIT QU'EFFLEURER LA SURFACE DE L'EAU.

Comme le montre la Figure 51, jusqu'à deux molécules d'eau peuvent être attachées au monomère si le tube Nafion® est plongé dans l'eau (spectre supérieur). En partant du dimère (m/z = 272), nous observons clairement que le niveau d'hydratation va jusqu'à neuf molécules d'eau ajoutées. Par contre, si le tube Nafion® touche juste la surface de l'eau (spectre inférieur), une seule molécule d'eau peut être ajoutée au monomère et le niveau d'hydratation est moindre pour toutes les tailles d'agrégats.

Après avoir considéré ces deux ensembles de données collectées à DESIRS, nous pouvons conclure que la source d'agrégats CELENO peut être finement ajustée pour produire différentes distributions d'agrégats, grâce

à la variation de quelques paramètres, à savoir la température du four, le flux d'hélium et la surface du tube Nafion® en contact avec l'eau.

7.3.2 STABILITÉ DE LA MOLÉCULE D'HYPOXANTHINE ET DE SES AGRÉGATS SUITE À L'IMPACT D'IONS

Les premières données à être analysées sont celles provenant des expériences de dissociation induite par les ions réalisées sur COLIMACON. Cette analyse nous permet de comprendre la stabilité moléculaire lors de l'irradiation par des ions O^{6+} à 90 keV. La charge multiple de l'ion oxygène garantit la production d'espèces ionisées multiples à partir de la cible, tandis que l'énergie choisie est la mieux adaptée pour observer, comme phénomène principal, la capture électronique.

7.3.2.1 DISSOCIATION DE LA MOLÉCULE D'HYPOXANTHINE ISOLÉE

Le spectre de masse de l'hypoxanthine isolée présente plusieurs caractéristiques intéressantes (Figure 52). Tout d'abord, on remarquer une forte stabilité moléculaire car le pic prédominant à m/z = 136 correspond au cation d'hypoxanthine intacte Hyp^+. La deuxième caractéristique concerne les principales voies de fragmentation moléculaire. L'hypoxanthine peut se fragmenter de deux manières consécutives majeures. Dans la première, nous pouvons reconnaître une perte initiale de CHN, donnant le fragment $(Hyp\text{-}CHN)^+$ de m/z = 109, qui évolue ensuite en $(Hyp\text{-}C_2H_3N_2)^+$ de m/z = 81 et en $(Hyp\text{-}C_3H_4N_3)^+$ de m/z = 54. Ce comportement séquentiel de perte de CHN est similaire au cas de l'adénine dans des conditions comparables[9]. L'autre voie de fragmentation est caractérisée par une perte initiale de CO, avec un pic à m/z = 108 représentant le fragment $(Hyp\text{-}CO)^+$. Cette fragmentation progresse ensuite avec une perte de CHN, $(Hyp\text{-}C_2HNO)^+$, à m/z = 81, point partagé avec l'autre voie principale, et se termine par deux pics : un à m/z = 54 représentant $(Hyp\text{-}\ C_3H_2N_2O)^+$, et le second à m/z = 53 correspondant à $(Hyp\text{-}C_3H_3N_2O)^+$. Ce dernier processus, impliquant la perte d'oxygène, est analogue à celui que subissent les molécules de guanine lors de leur fragmentation[23].

Enfin, nous avons pu observer un pic correspondant à l'hypoxanthine doublement ionisée intacte à $m/z = 68$. Ces résultats nous ont encouragés à explorer la carte des coïncidences pour la fragmentation du dication d'hypoxanthine. Ces résultats sont discutés en détail dans le chapitre 5.

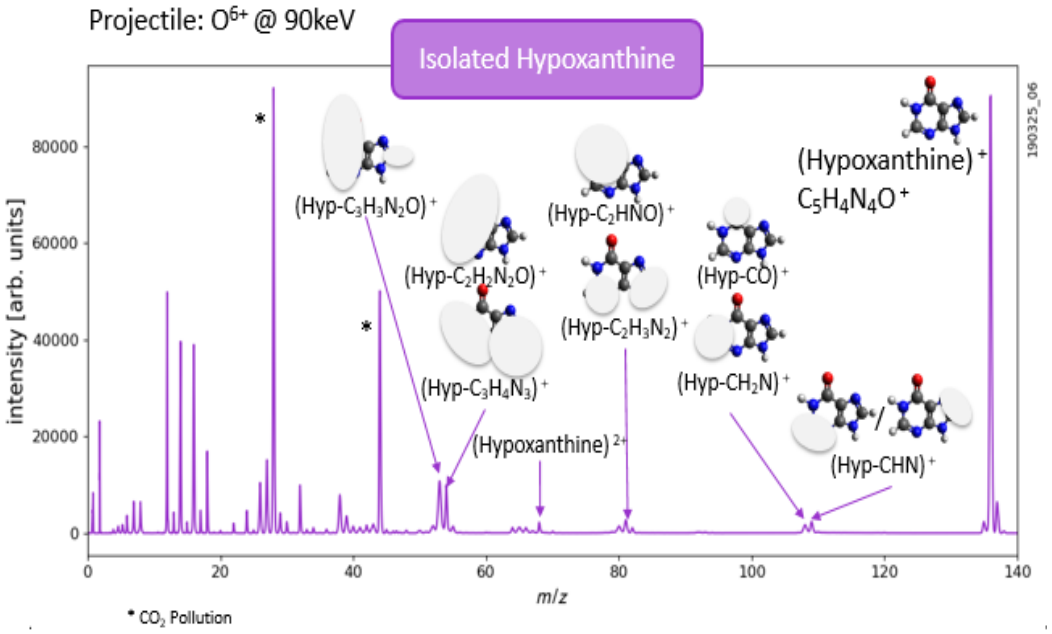

FIGURE 52: SPECTRE DE MASSE OBTENU POUR L'HYPOXANTHINE ISOLÉE APRÈS COLLISION AVEC UN PROJECTILE O^{6+} À 90 KEV.

7.3.2.2 DISSOCIATION DES AGRÉGATS PURS ET HYDRATÉS D'HYPOXANTHINE

Après l'acquisition des spectres de masse de la molécule isolée, nous avons procédé à la réalisation des expériences sur les agrégats purs et hydratés. La formation des agrégats purs a été obtenue à 516 K pour la température du four, et avec un débit d'He égal à 160 mL/min. Pour les agrégats d'hypoxanthine hydratés, le four a été réglé à 508 K, avec un flux d'He de 180 mL/min, le tube de Nafion® étant immergé dans l'eau. À partir des spectres de fragmentation des agrégats d'hypoxanthine purs et hydratés, représentés respectivement sur les Figure 53 b) et c), nous avons obtenu des informations sur la façon dont les liaisons H peuvent influencer la fragmentation moléculaire. Ces deux spectres présentent les mêmes nouvelles caractéristiques par rapport à la molécule isolée. Ces spectres

comprennent des fragments provenant de la dissociation de la molécule protonée. Le premier nouveau fragment rencontré est de m/z = 119, résultant de la perte de H_2O, appelé $[Hyp]H^+$-H_2O et correspondant à la formule $C_5H_3N_4^+$. Cette voie de fragmentation particulière a déjà été observée pour d'autres nucléobases, comme l'uracile[71]. Le fragment suivant à m/z = 109 indique la perte de CO de la molécule d'hypoxanthine protonée et correspond à l'ion moléculaire $[C_4H_4N_4 + H]^+$. Un fragment suivant est trouvé à m/z = 94 et est décrit par la formule $C_4H_2N_2O^+$. Il est suivi par $C_4H_3N_3^+$ à m/z = 93, et par $C_3H_2N_2O^+$ (ou $C_3H_4N_3^+$) à m/z = 82 avec son fragment complémentaire $[C_2H_2N_2 + H]^+$ (ou C_2HNO^+) à m/z = 55. L'identification de ces fragments comme étant issus de l'hypoxanthine protonée est en accord avec les données extraites de la Japanese Mass Bank[72].

Enfin, dans le spectre de fragmentation des molécules hydratées, nous n'observons pas de fragment hydraté. Ceci suggère que le niveau d'hydratation durant cette expérience était faible.

7.3.3 PROPRIÉTÉS CHIMIQUES DE L'HYPOXANTHINE EN FONCTION DE SON ENVIRONNEMENT MOLÉCULAIRE

7.3.3.1 PARAMÈTRES D'ACQUISION POUR LA SPECTROMÉTRIE XPS

Les spectres XPS pour les signaux C 1s, N 1s et O 1s des agrégats purs ont été acquis en utilisant la source d'agrégats CELENO à différentes températures de four. De premières données ont été collectées à 481 K, pour lesquelles le signal O 1s a également été collecté, tandis qu'une seconde série de données a été enregistrée à 487 K. La température du four a été modifiée afin de voir si une différence significative était observable dans les spectres électroniques lorsque la taille des agrégats moléculaires était augmentée. Le flux de gaz He a été maintenu à 180 mL/min pendant toute l'expérience, avec une pression de 18 mbar pour les agrégats purs, et 18.5 mbar pour les agrégats hydratés (puisque des molécules d'eau se trouvaient dans le flux de gaz). Les données concernant les espèces hydratées ont été collectées à 490 K.

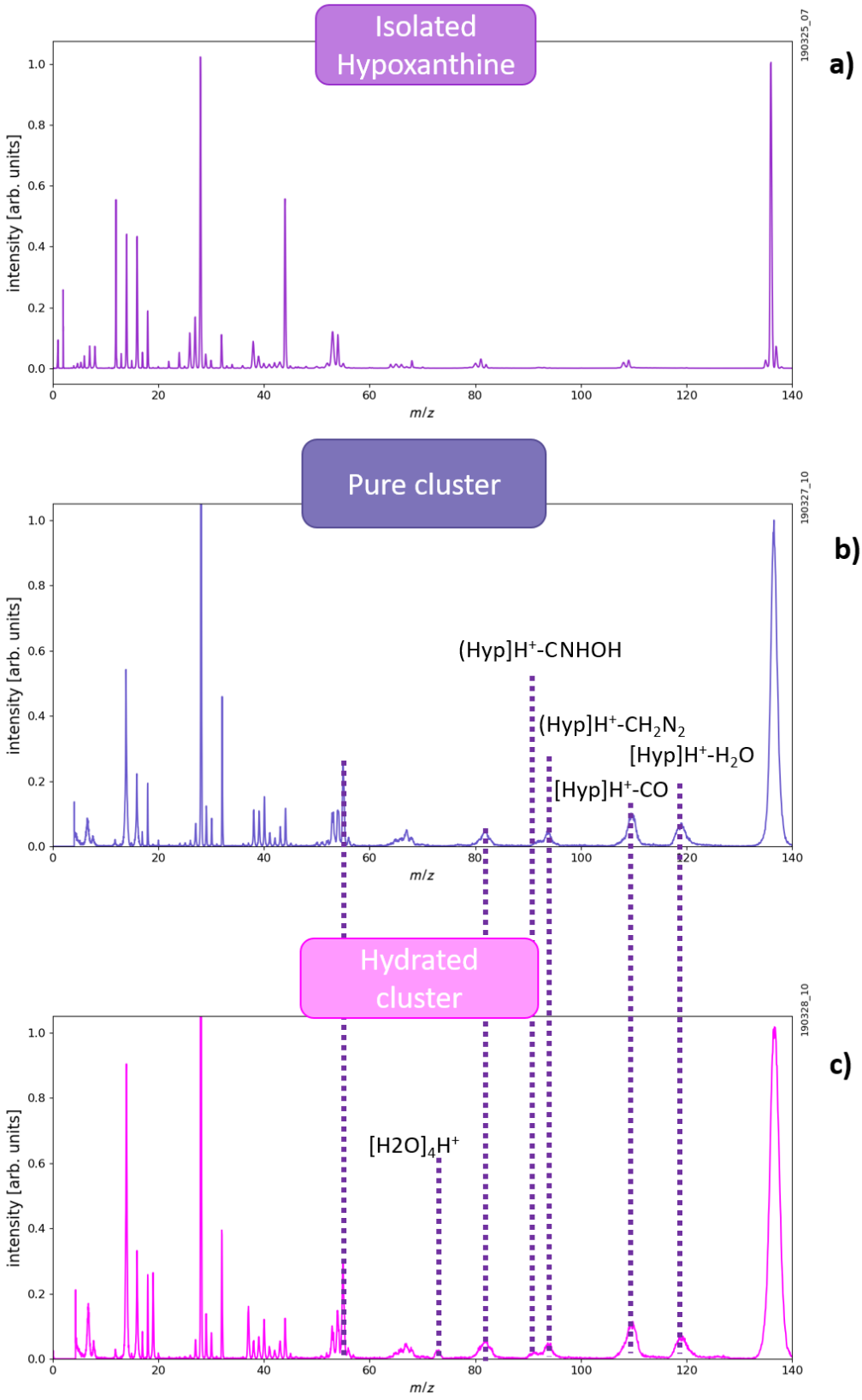

FIGURE 53: COMPARAISON DES SPECTRES DE FRAGMENTATION DE A) LA MOLÉCULE D'HYPOXANTHINE ISOLÉE, B) LES AGRÉGATS D'HYPOXANTHINE PURE, ET C) LES AGRÉGATS D'HYPOXANTHINE HYDRATÉS LORS DE LA COLLISION AVEC UN PROJECTILE O^{6+} À 90 KEV.

Les spectres de C 1s ont été collectés à une énergie de photon de 370 eV, ceux de N 1s à 480 eV, et ceux de O 1s à 610 eV. Cela signifie que les spectres XPS présentés ont été mesurés à environ 70 eV au-dessus des seuils d'ionisation de la couche K des différentes espèces atomiques.

7.3.3.2 COMPARAISON DES RÉSULTATS XPS POUR LA MOLÉCULE ISOLÉE ET POUR LES AGRÉGATS PURS ET HYDRATÉS

La molécule d'hypoxanthine est caractérisée par un cycle imidazole conjugué à un cycle pyrimidine, avec un oxygène attaché en position 6 (Figure 54). À partir de la structure de la molécule, on peut prédire quatre signaux XPS différents provenant du carbone, deux de l'azote et un de l'oxygène. Les différents signaux C 1s sont liés aux atomes de carbone suivants :

- le carbone en position 5, qui est celui qui est entouré du plus grand nombre d'atomes de carbone, avec les liaisons C-C=C et C-N,
- les atomes C2 et C8 impliqués dans les liaisons HN-CH=N,
- l'atome C4 impliqué dans les liaisons C=C et HN-C-N,
- le carbone lié à l'oxygène.

Pour l'azote, les deux signaux N 1s sont liés aux atomes N de l'imine en positions 3 et 7 et aux atomes N de l'amine en positions 1 et 9.
Pour l'oxygène, un seul signal O 1s est attendu pour la molécule isolé et pour les agrégats purs puisqu'un seul atome d'oxygène est présent (en position 6).

La comparaison des spectres photoélectroniques du carbone, de l'azote et de l'oxygène de l'hypoxanthine isolée (Plekan *et al.*[33]) et de ses agrégats (purs et hydratés) est présentée dans la Figure 54. Même si le nombre de pics C 1s et N 1s présents dans chaque spectre XPS est inchangé entre l'hypoxanthine isolée et les agrégats, l'intensité relative de ces pics, leur largeur et les énergies de liaison correspondantes subissent des changements significatifs. Par conséquent, les données XPS nous fournissent des informations intéressantes sur les changements des propriétés chimiques de la molécule d'hypoxanthine lorsqu'elle est entourée d'autres molécules par rapport au cas où elle est isolée.

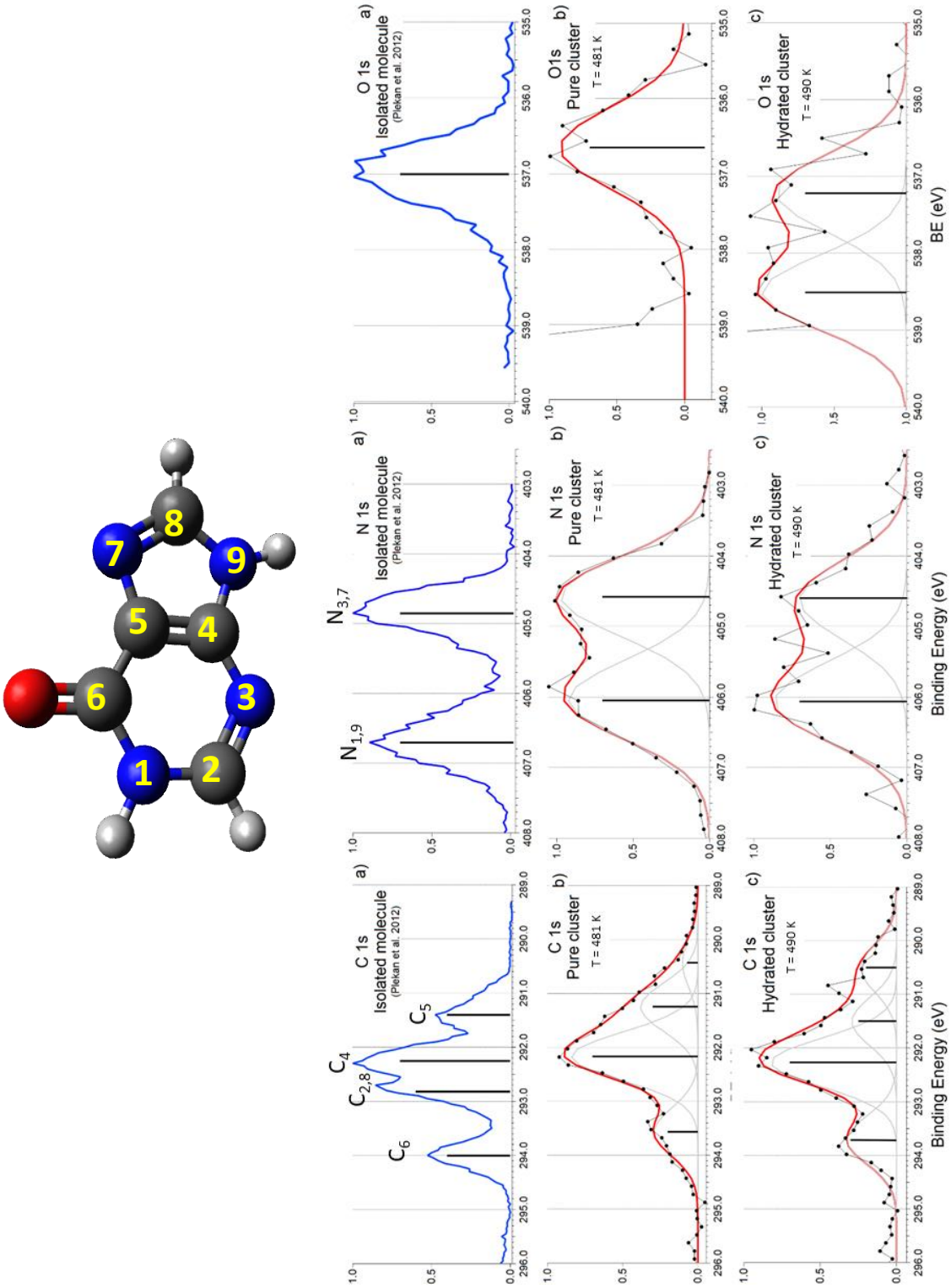

FIGURE 54: COMPARAISON DE TOUS LES SIGNAUX XPS ACQUIS EN FONCTION DE L'ÉNERGIE DE LIAISON DES ÉLECTRONS 1S. DE GAUCHE À DROITE : LE SIGNAL C 1S, LE SIGNAL N1S ET LE SIGNAL O 1S. POUR CHACUN DES TROIS SIGNAUX, LE PANEL A) REPRÉSENTE LE SPECTRE DE L'HYPOXANTHINE ISOLÉE EXTRAIT DE LA LITTÉRATURE (PLEKAN ET AL. 2012). LES PANELS B) ET C) MONTRENT LES SIGNAUX DES AGRÉGATS PURS ET HYDRATÉS, RESPECTIVEMENT. LES SPECTRES DES AGRÉGATS ONT ÉTÉ DÉCONVOLUÉS POUR APPRÉCIER LA CONTRIBUTION DE LA COMPOSANTE UNIQUE DANS DIFFÉRENTS ENVIRONNEMENTS.

Pour les agrégats d'hypoxanthine pure, nous observons quelques changements par rapport au cas de la molécule isolée, à savoir le déplacement de tous les spectres XPS vers des énergies de liaison plus faibles des électrons 1s et l'élargissement des structures spectrales. Cet élargissement peut être expliqué par le fait que dans les gros agrégats, toutes les molécules n'ont pas le même environnement moléculaire et ont donc des énergies de liaison électronique différentes, ce qui entraîne un élargissement apparent. En outre, l'influence des liaisons hydrogène diminue globalement l'énergie de liaison des électrons. Cela signifie que la formation de liaisons hydrogène place les électrons de cœur dans un état moins lié. D'autres changements au niveau des structures spectrales des signaux XPS de l'hypoxanthine sont observés dans le cas des agrégats hydratés. Dans ce cas, l'influence des liaisons hydrogène formées avec les molécules d'eau modifie davantage certaines caractéristiques du signal, notamment celles impliquant plus ou moins directement l'atome d'oxygène.

7.4 CONCLUSIONS

En plus de manifester une grande stabilité moléculaire lors de son impact avec des ions hautement chargés, l'hypoxanthine présente un comportement qui ressemble beaucoup à celui observé avec l'adénine et la guanine. Nous avons observé que les deux principales voies de fragmentation sont communes à l'adénine et à l'hypoxanthine. Ces voies impliquent la perte du fragment neutre HCN^0 comme première étape commune. Selon que ce groupe est perdu par le cycle pyrimidine ou par le cycle imidazole, deux processus différents surviennent. De plus, la perte du fragment neutre CO^0, qui ressemble beaucoup au processus qui a lieu lors de la fragmentation de la guanine, représente une voie de fragmentation importante pour l'hypoxanthine. Ces résultats soutiennent l'idée que les purines présentent généralement un ensemble de caractéristiques communes. Premièrement, étant donné qu'elles comportent toutes des cycles aromatiques, elles présentent une grande stabilité moléculaire lors de l'ionisation. Cette grande stabilité est

également la justification physique du fait qu'elles constituent les vecteurs de l'information génétique dans les cellules vivantes. Ensuite, ces trois purines présentent un ensemble commun de sites de fragmentation, à savoir les deux groupes HCN en position 2-3 et 7-8, l'autre étant la séparation des deux cycles au niveau des carbones doublement liés en position 4-5. De plus, cette étude a mis en évidence que pendant la formation des agrégats, l'adénine et l'hypoxanthine requièrent toutes les deux l'implication de leurs substituants cycliques dans la formation de liaisons hydrogène. L'analyse de la croissance des agrégats souligne l'importance du substituant oxygène en position 6, qui aide à la stabilisation des agrégats purs et favorise l'hydratation de la molécule lors de la production d'agrégats hydratés.

En prenant en considération les données obtenues lors de l'expérience XPS, nous pouvons conclure que les agrégats d'hypoxanthine pure présentent des caractéristiques similaires à celles de la molécule isolée. La différence remarquable entre les deux états d'agrégation consiste en l'élargissement général des structures spectrales, et leur déplacement vers des énergies de liaison plus faibles. Ces changements peuvent être facilement attribués à l'état d'agrégation des agrégats et à leur taille. Les informations obtenues pour les agrégats hydratés ressemblent beaucoup aux informations déjà disponibles concernant l'uracile. En fait, la modification des spectres obtenus réside dans l'augmentation de l'intensité et le léger décalage vers une énergie de liaison plus élevée de la couche *K* du groupe amine dans le spectre N 1s, ce qui indique son implication dans la formation de nouvelles liaisons hydrogène, à attribuer à l'oxygène de l'eau. L'autre nouvelle caractéristique, comme il était prévisible, concerne le spectre O 1s, qui présente un déplacement significatif vers une énergie de liaison plus élevée pour l'atome d'oxygène de l'hypoxanthine et un nouveau pic attribué à la formation d'agrégats d'eau. L'augmentation de cette énergie de liaison est une indication claire de l'implication de cet atome d'oxygène dans la formation des agrégats hydratés.

8 BIBLIOGRAPHY

(1) Gohlke, S.; Illenberger, E. Probing Biomolecules: Gas Phase Experiments and Biological Relevance. *Europhysics News* **2002**, *33* (6), 207–209. https://doi.org/10.1051/epn:2002607.

(2) Dopfer, O.; Fujii, M. Probing Solvation Dynamics around Aromatic and Biological Molecules at the Single-Molecular Level. *Chem. Rev.* **2016**, *116* (9), 5432–5463. https://doi.org/10.1021/acs.chemrev.5b00610.

(3) *Solvation Effects on Molecules and Biomolecules: Computational Methods and Applications*; Canuto, S., Ed.; Challenges and advances in computational chemistry and physics; Springer: Dordrecht, 2008.

(4) Nelson, D. L.; Cox, M. M. *Lehninger_Principles_of_Biochemistry_()Pdf*, 6th_edition.; Macmillan Higher Education.

(5) Rawn, J. D. *Biochimica*; Medicina; McGraw-Hill, 1990.

(6) Fenn, J. B.; Mann, M.; Meng, C. K.; Wong, S. F.; Whitehouse, C. M. Electrospray Ionization for Mass Spectrometry of Large Biomolecules. *Science* **1989**, *246* (4926), 64–71. https://doi.org/10.1126/science.2675315.

(7) Lifshitz, C.; Laskin, J. *Principles of Mass Spectrometry Applied to Biomolecules*; John Wiley & Sons, 2006.

(8) Mattioli, G.; Avaldi, L.; Bolognesi, P.; Bozek, J. D.; Castrovilli, M. C.; Chiarinelli, J.; Domaracka, A.; Indrajith, S.; Maclot, S.; Milosavljević, A. R.; Nicolafrancesco, C.; Rousseau, P. Water–Biomolecule Clusters Studied by Photoemission Spectroscopy and Multilevel Atomistic Simulations: Hydration or Solvation? *Phys. Chem. Chem. Phys.* **2021**, 10.1039.D1CP02031E. https://doi.org/10.1039/D1CP02031E.

(9) Domaracka, A.; Capron, M.; Maclot, S.; Chesnel, J.-Y.; Méry, A.; Poully, J.-C.; Rangama, J.; Adoui, L.; Rousseau, P.; Huber, B. A. Ion Interaction with Biomolecular Systems and the Effect of the Environment. *J. Phys.: Conf. Ser.* **2012**, *373*, 012005. https://doi.org/10.1088/1742-6596/373/1/012005.

(10) *Radiation Induced Molecular Phenomena in Nucleic Acids: A Comprehensive Theoretical and Experimental Analysis*; Shukla, M., Leszczynski, J., Eds.; Challenges and advances in computational chemistry and physics; Springer: Dordrecht ; London, 2008.

(11) Orecchia, R.; Fossati, P.; Rossi, S. The National Center for Oncological Hadron Therapy: Status of the Project and Future Clinical Use of the Facility. *Tumori* **2009**, *95* (2), 169–176. https://doi.org/10.1177/030089160909500207.

(12) Wang, X.-J.; You, J.-Z. Study on the Molecular Structure and Thermal Stability of Purine Nucleoside Analogues.

(13) Ege, S. *La chimica organica essenziale*; Idelson-Gnocchi, 2008.

(14) Solinas, M.; Ferré, S.; You, Z.-B.; Karcz-Kubicha, M.; Popoli, P.; Goldberg, S. R. Caffeine Induces Dopamine and Glutamate Release in the Shell of the Nucleus Accumbens. *J. Neurosci.* **2002**, *22* (15), 6321–6324. https://doi.org/10.1523/JNEUROSCI.22-15-06321.2002.

(15) Basheer, R.; Strecker, R. E.; Thakkar, M. M.; McCarley, R. W. Adenosine and Sleep–Wake Regulation. *Progress in Neurobiology* **2004**, *73* (6), 379–396. https://doi.org/10.1016/j.pneurobio.2004.06.004.

(16) Lee, C.-Y. I.; Delaney, J. C.; Kartalou, M.; Lingaraju, G. M.; Maor-Shoshani, A.; Essigmann, J. M.; Samson, L. D. *Recognition and Processing of a New Repertoire of DNA Substrates by Human 3-Methyladenine DNA Glycosylase (AAG)†*. ACS Publications. https://pubs.acs.org/doi/pdf/10.1021/bi8018898 (accessed 2021-07-19). https://doi.org/10.1021/bi8018898.

(17) Brovarets, O. O.; Hovorun, D. M. Can Tautomerization of the A·T Watson–Crick Base Pair via Double Proton Transfer Provoke Point Mutations during DNA Replication? A

Comprehensive QM and QTAIM Analysis. *Journal of Biomolecular Structure and Dynamics* **2014**, *32* (1), 127–154. https://doi.org/10.1080/07391102.2012.755795.
(18) *Blue Book*. https://iupac.qmul.ac.uk/BlueBook/PDF/ (accessed 2022-05-23).
(19) Yarom, M.; Tang, X. W.; Wu, E.; Carlson, R. G.; Velde, D. V.; Lee, X.-H.; Wu, J.-Y. Identification of Inosine as an Endogenous Modulator for the Benzodiazepine Binding Site of the GABAA Receptors. *J Biomed Sci* **1998**, *5* (4), 274–280. https://doi.org/10.1007/BF02255859.
(20) Liu, F.; You, S.-W.; Yao, L.-P.; Liu, H.-L.; Jiao, X.-Y.; Shi, M.; Zhao, Q.-B.; Ju, G. Secondary Degeneration Reduced by Inosine after Spinal Cord Injury in Rats. *Spinal Cord* **2006**, *44* (7), 421–426.
(21) Chen, P.; Goldberg, D. E.; Kolb, B.; Lanser, M.; Benowitz, L. I. Inosine Induces Axonal Rewiring and Improves Behavioral Outcome after Stroke. *Proceedings of the National Academy of Sciences* **2002**, *99* (13), 9031–9036. https://doi.org/10.1073/pnas.132076299.
(22) Jochims, H.-W.; Schwell, M.; Baumgärtel, H.; Leach, S. Photoion Mass Spectrometry of Adenine, Thymine and Uracil in the 6–22eV Photon Energy Range. *Chemical Physics* **2005**, *314* (1–3), 263–282. https://doi.org/10.1016/j.chemphys.2005.03.008.
(23) Sadr-Arani, L.; Mignon, P.; Chermette, H.; Abdoul-Carime, H.; Farizon, B.; Farizon, M. Fragmentation Mechanisms of Cytosine, Adenine and Guanine Ionized Bases. *Phys. Chem. Chem. Phys.* **2015**, *17* (17), 11813–11826. https://doi.org/10.1039/C5CP00104H.
(24) Schlathölter, T.; Alvarado, F.; Bari, S.; Lecointre, A.; Hoekstra, R.; Bernigaud, V.; Manil, B.; Rangama, J.; Huber, B. Ion-Induced Biomolecular Radiation Damage: From Isolated Nucleobases to Nucleobase Clusters. *ChemPhysChem* **2006**, *7* (11), 2339–2345. https://doi.org/10.1002/cphc.200600361.
(25) Mons, M.; Dimicoli, I.; Piuzzi, F.; Tardivel, B.; Elhanine, M. Tautomerism of the DNA Base Guanine and Its Methylated Derivatives as Studied by Gas-Phase Infrared and Ultraviolet Spectroscopy. *J. Phys. Chem. A* **2002**, *106* (20), 5088–5094. https://doi.org/10.1021/jp0139742.
(26) Plekan, O.; Feyer, V.; Richter, R.; Coreno, M.; de Simone, M.; Prince, K. C.; Trofimov, A. B.; Gromov, E. V.; Zaytseva, I. L.; Schirmer, J. A Theoretical and Experimental Study of the near Edge X-Ray Absorption Fine Structure (NEXAFS) and X-Ray Photoelectron Spectra (XPS) of Nucleobases: Thymine and Adenine. *Chemical Physics* **2008**, *347* (1–3), 360–375. https://doi.org/10.1016/j.chemphys.2007.09.021.
(27) Furukawa, M.; Yamada, T.; Katano, S.; Kawai, M.; Ogasawara, H.; Nilsson, A. Geometrical Characterization of Adenine and Guanine on Cu(110) by NEXAFS, XPS, and DFT Calculation. *Surface Science* **2007**, *601* (23), 5433–5440. https://doi.org/10.1016/j.susc.2007.09.009.
(28) Barc, B.; Ryszka, M.; Poully, J.-C.; Jabbour Al Maalouf, E.; el Otell, Z.; Tabet, J.; Parajuli, R.; van der Burgt, P. J. M.; Limão-Vieira, P.; Cahillane, P.; Dampc, M.; Mason, N. J.; Eden, S. Multi-Photon and Electron Impact Ionisation Studies of Reactivity in Adenine–Water Clusters. *International Journal of Mass Spectrometry* **2014**, *365–366*, 194–199. https://doi.org/10.1016/j.ijms.2014.01.007.
(29) Alvarado, F.; Bari, S.; Hoekstra, R.; Schlathölter, T. Interactions of Neutral and Singly Charged KeV Atomic Particles with Gas-Phase Adenine Molecules. *J. Chem. Phys.* **2007**, *127* (3), 034301. https://doi.org/10.1063/1.2751502.
(30) Moretto-Capelle, P.; Le Padellec, A.; Brière, G.; Massou, S.; Franceries, F. Energetics and Metastability of the Adenine Dication Observed in Proton-Adenine Collisions. *J. Chem. Phys.* **2007**, *127* (23), 234311. https://doi.org/10.1063/1.2827476.
(31) Dawley, M. M.; Tanzer, K.; Cantrell, W. A.; Plattner, P.; Brinkmann, N. R.; Scheier, P.; Denifl, S.; Ptasińska, S. Electron Ionization of the Nucleobases Adenine and Hypoxanthine near the Threshold: A Combined Experimental and Theoretical Study. *Phys. Chem. Chem. Phys.* **2014**, *16* (45), 25039–25053. https://doi.org/10.1039/C4CP03452J.

(32) Feyer, V.; Plekan, O.; Richter, R.; Coreno, M.; Prince, K. C. Photoion Mass Spectroscopy and Valence Photoionization of Hypoxanthine, Xanthine and Caffeine. *Chemical Physics* **2009**, *358* (1), 33–38. https://doi.org/10.1016/j.chemphys.2008.12.014.
(33) Plekan, O.; Feyer, V.; Richter, R.; Moise, A.; Coreno, M.; Prince, K. C.; Zaytseva, I. L.; Moskovskaya, T. E.; Soshnikov, D. Yu.; Trofimov, A. B. X-Ray Spectroscopy of Heterocyclic Biochemicals: Xanthine, Hypoxanthine, and Caffeine. *J. Phys. Chem. A* **2012**, *116* (23), 5653–5664. https://doi.org/10.1021/jp300459p.
(34) Morgan, R. P. Practical Mass Spectrometry — A Contemporary Introduction. *International Journal of Mass Spectrometry and Ion Physics* **1981**, *37* (3), 383. https://doi.org/10.1016/0020-7381(81)80059-9.
(35) Wang, Y. D.; Lin, C. D.; Toshima, N.; Chen, Z. Ionization and Charge Transfer in Collisions of Highly Charged Ions with Helium at Low Velocity. *Phys. Rev. A* **1995**, *52* (4), 2852–2858. https://doi.org/10.1103/PhysRevA.52.2852.
(36) Vernhet, D.; Rozet, J. P.; Wohrer, K.; Adoui, L.; Stéphan, C.; Cassimi, A.; Ramillon, J. M. Excitation in Swift Heavy Ion-Atom Collisions. *Nuclear Instruments and Methods in Physics Research Section B: Beam Interactions with Materials and Atoms* **1996**, *107* (1), 71–78. https://doi.org/10.1016/0168-583X(95)00807-1.
(37) Padovani, M.; Galli, D.; Glassgold, A. E. Cosmic-Ray Ionization of Molecular Clouds. *A&A* **2009**, *501* (2), 619–631. https://doi.org/10.1051/0004-6361/200911794.
(38) Eland, J. H. D. DYNAMICS OF FRAGMENTATION REACTIONS FROM PEAK SHAPES IN MULTIPARTICLE COINCIDENCE EXPERIMENTS. 5.
(39) Charnley, S. Photoionization. In *Encyclopedia of Astrobiology*; Gargaud, M., Amils, R., Quintanilla, J. C., Cleaves, H. J. (Jim), Irvine, W. M., Pinti, D. L., Viso, M., Eds.; Springer: Berlin, Heidelberg, 2011; pp 1244–1244. https://doi.org/10.1007/978-3-642-11274-4_1199.
(40) Collectif. *Encyclopedia of Spectroscopy and Spectrometry Ed. 3*; Elsevier Science, 2016.
(41) Yamashita, M. Mass Spectrometry. In *Encyclopedia of Astrobiology*; Gargaud, M., Amils, R., Quintanilla, J. C., Cleaves, H. J. (Jim), Irvine, W. M., Pinti, D. L., Viso, M., Eds.; Springer: Berlin, Heidelberg, 2011; pp 1002–1004. https://doi.org/10.1007/978-3-642-11274-4_1030.
(42) Mariani, C.; Stefani, G. Photoemission Spectroscopy: Fundamental Aspects. In *Synchrotron Radiation: Basics, Methods and Applications*; Mobilio, S., Boscherini, F., Meneghini, C., Eds.; Springer: Berlin, Heidelberg, 2015; pp 275–317. https://doi.org/10.1007/978-3-642-55315-8_9.
(43) Milani, P.; Iannotta, S. *Cluster Beam Synthesis of Nanostructured Materials*; Springer series in cluster physics; Springer: Berlin Heidelberg New York Barcelona Budapest Hong Kong London Milan Paris Singapore Tokyo, 1999.
(44) Zimmermann, U.; Malinowski, N.; Näher, U.; Frank, S.; Martin, T. P. Producing and Detecting Very Large Clusters. *Z Phys D - Atoms, Molecules and Clusters* **1994**, *31* (1), 85–93. https://doi.org/10.1007/BF01426583.
(45) Hansen, K. Stability of Clusters of Fullerenes. 4.
(46) Manil, B.; Maunoury, L.; Huber, B. A.; Jensen, J.; Schmidt, H. T.; Zettergren, H.; Cederquist, H.; Tomita, S.; Hvelplund, P. Highly Charged Clusters of Fullerenes: Charge Mobility and Appearance Sizes. *Phys. Rev. Lett.* **2003**, *91* (21), 215504. https://doi.org/10.1103/PhysRevLett.91.215504.
(47) Schmidt, M.; Masson, A.; Bréchignac, C. Coronene Cluster Experiments: Stability and Thermodynamics. *International Journal of Mass Spectrometry* **2006**, *252* (2), 173–179. https://doi.org/10.1016/j.ijms.2005.10.015.
(48) Zamith, S.; Labastie, P.; L'Hermite, J.-M. Fragmentation Cross Sections of Protonated Water Clusters. *J. Chem. Phys.* **2012**, *136* (21), 214301. https://doi.org/10.1063/1.4722886.

(49) Maisonny, R.; Capron, M.; Maclot, S.; Poully, J. C.; Domaracka, A.; Méry, A.; Adoui, L.; Rousseau, P.; Huber, B. A. Ion Interactions with Pure and Mixed Water Clusters. *J. Phys.: Conf. Ser.* **2013**, *438*, 012007. https://doi.org/10.1088/1742-6596/438/1/012007.
(50) Mattioli, G.; Avaldi, L.; Bolognesi, P.; Bozek, J. D.; Castrovilli, M. C.; Chiarinelli, J.; Domaracka, A.; Indrajith, S.; Maclot, S.; Milosavljević, A. R.; Nicolafrancesco, C.; Nicolas, C.; Rousseau, P. Unravelling Molecular Interactions in Uracil Clusters by XPS Measurements Assisted by Ab Initio and Tight-Binding Simulations. *Sci Rep* **2020**, *10* (1), 13081. https://doi.org/10.1038/s41598-020-69947-3.
(51) Markush, P.; Bolognesi, P.; Cartoni, A.; Rousseau, P.; Maclot, S.; Delaunay, R.; Domaracka, A.; Kocisek, J.; Castrovilli, M. C.; Huber, B. A.; Avaldi, L. The Role of the Environment in the Ion Induced Fragmentation of Uracil. *Phys. Chem. Chem. Phys.* **2016**, *18* (25), 16721–16729. https://doi.org/10.1039/C6CP01940D.
(52) *Clusters of Atoms and Molecules*; Haberland, H., Ed.; Goldanskii, V. I., Schäfer, F. P., Toennies, J. P., Lotsch, H. K. V., Series Eds.; Springer Series in Chemical Physics; Springer Berlin Heidelberg: Berlin, Heidelberg, 1994; Vol. 52. https://doi.org/10.1007/978-3-642-84329-7.
(53) Bergen, T.; Biquard, X.; Brenac, A.; Chandezon, F.; Huber, B. A.; Jalabert, D.; Lebius, H.; Maurel, M.; Monnand, E.; Opitz, J.; Pesnelle, A.; Pras, B.; Ristori, C.; Rocco, J. C. Multiply Charged Cluster Ion Crossed-Beam Apparatus: Multi-Ionization of Clusters by Ion Impact. *Review of Scientific Instruments* **1999**, *70* (8), 3244–3253. https://doi.org/10.1063/1.1149900.
(54) Bréchignac, C.; Cahuzac, P.; Carlier, F.; de Frutos, M.; Masson, A.; Roux, J. P. Generation of Rare Earth Metal Clusters by Means of the Gas-Aggregation Technique. 3.
(55) Kočišek, J.; Pysanenko, A.; Fárník, M.; Fedor, J. Microhydration Prevents Fragmentation of Uracil and Thymine by Low-Energy Electrons. *J. Phys. Chem. Lett.* **2016**, *7* (17), 3401–3405. https://doi.org/10.1021/acs.jpclett.6b01601.
(56) Toivanen, V ; Barue, C ; Feierstein, C ; Jardin, P ; Lemagnen, F ; Maunoury, L ; Noury, F ; Rousseau, P ; PROCEEDINGS OF THE 17TH INTERNATIONAL CONFERENCE ON ION SOURCES **2018**, *2011*, 040008. https://doi.org/10.1063/1.5053282
(57) Maunoury, L.; Leroy, R.; Been, T.; Gaubert, G.; Guillaume, L.; Leclerc, D.; Lepoutre, A.; Mouton, V.; Pacquet, J. Y.; Ramillon, J. M.; Vicquelin, R.; The GANIL Ion Production Group. LIMBE: A New Facility for Low Energy Beams. *Review of Scientific Instruments* **2002**, *73* (2), 561–563. https://doi.org/10.1063/1.1430032.
(58) Wiley, W. C.; McLaren, I. H. Time-of-Flight Mass Spectrometer with Improved Resolution. *Review of Scientific Instruments* **1955**, *26* (12), 1150–1157. https://doi.org/10.1063/1.1715212.
(59) Daly, N. R. Scintillation Type Mass Spectrometer Ion Detector. *Review of Scientific Instruments* **1960**, *31* (3), 264–267. https://doi.org/10.1063/1.1716953.
(60) Chandezon, F.; Huber, B.; Ristori, C. A New-regime Wiley–McLaren Time-of-flight Mass Spectrometer. *Review of Scientific Instruments* **1994**, *65* (11), 3344–3353. https://doi.org/10.1063/1.1144571.
(61) Dumas, P.; Polack, F.; Lagarde, B.; Chubar, O.; Giorgetta, J. L.; Lefrançois, S. Synchrotron Infrared Microscopy at the French Synchrotron Facility SOLEIL. *Infrared Physics & Technology* **2006**, *49* (1), 152–160. https://doi.org/10.1016/j.infrared.2006.01.030.
(62) *Centre de rayonnement synchrotron français*. https://www.synchrotron-soleil.fr/fr (accessed 2021-10-05).
(63) Lindblad, A.; Söderström, J.; Nicolas, C.; Robert, E.; Miron, C. A Multi Purpose Source Chamber at the PLEIADES Beamline at SOLEIL for Spectroscopic Studies of Isolated Species: Cold Molecules, Clusters, and Nanoparticles. *Rev. Sci. Instrum.* **2013**, 12.
(64) *PLÉIADES | French national synchrotron facility*. https://www.synchrotron-soleil.fr/en/beamlines/pleiades (accessed 2021-09-08).

(65) Nahon, L.; de Oliveira, N.; Garcia, G. A.; Gil, J.-F.; Pilette, B.; Marcouillé, O.; Lagarde, B.; Polack, F. DESIRS: A State-of-the-Art VUV Beamline Featuring High Resolution and Variable Polarization for Spectroscopy and Dichroism at SOLEIL. *J Synchrotron Rad* **2012**, *19* (4), 508–520. https://doi.org/10.1107/S0909049512010588.
(66) Tang, X.; Garcia, G. A.; Gil, J.-F.; Nahon, L. Vacuum Upgrade and Enhanced Performances of the Double Imaging Electron/Ion Coincidence End-Station at the Vacuum Ultraviolet Beamline DESIRS. *Review of Scientific Instruments* **2015**, *86* (12), 123108. https://doi.org/10.1063/1.4937624.
(67) Garcia, G. A.; Cunha de Miranda, B. K.; Tia, M.; Daly, S.; Nahon, L. DELICIOUS III: A Multipurpose Double Imaging Particle Coincidence Spectrometer for Gas Phase Vacuum Ultraviolet Photodynamics Studies. *Review of Scientific Instruments* **2013**, *84* (5), 053112. https://doi.org/10.1063/1.4807751.
(68) Fraser, G. W. The Ion Detection Efficiency of Microchannel Plates (MCPs). *International Journal of Mass Spectrometry* **2002**, *215* (1), 13–30. https://doi.org/10.1016/S1387-3806(01)00553-X.
(69) Jongma, R. T.; Huang, Y.; Shi, S.; Wodtke, A. M. Rapid Evaporative Cooling Suppresses Fragmentation in Mass Spectrometry: Synthesis of "Unprotonated" Water Cluster Ions. *J. Phys. Chem. A* **1998**, *102* (45), 8847–8854. https://doi.org/10.1021/jp983366v.
(70) Gartmann, T. E.; Hartweg, S.; Ban, L.; Chasovskikh, E.; Yoder, B. L.; Signorell, R. Electron Scattering in Large Water Clusters from Photoelectron Imaging with High Harmonic Radiation. *Phys. Chem. Chem. Phys.* **2018**, *20* (24), 16364–16371. https://doi.org/10.1039/C8CP02148A.
(71) Molina, E. R.; Ortiz, D.; Salpin, J.-Y.; Spezia, R. Elucidating Collision Induced Dissociation Products and Reaction Mechanisms of Protonated Uracil by Coupling Chemical Dynamics Simulations with Tandem Mass Spectrometry Experiments. *Journal of Mass Spectrometry* **2015**, *50* (12), 1340–1351. https://doi.org/10.1002/jms.3704.
(72) MassBank Record: PS025203 6-Oxopurine, Sarcine, HX, Sarkine, Hypoxanthine Enol, 6-Hydroxypurine, Sarkin, Hypoxanthine; LC-ESI-QQ; MS2. *Japanese Mass Bank*.
(73) Milosavljević, A. R.; Cerovski, V. Z.; Canon, F.; Nahon, L.; Giuliani, A. Nanosolvation-Induced Stabilization of a Protonated Peptide Dimer Isolated in the Gas Phase. *Angewandte Chemie International Edition* **2013**, *52* (28), 7286–7290. https://doi.org/10.1002/anie.201301667.
(74) Myrseth, V.; Bozek, J. D.; Kukk, E.; Sæthre, L. J.; Thomas, T. D. Adiabatic and Vertical Carbon 1s Ionization Energies in Representative Small Molecules. *Journal of Electron Spectroscopy and Related Phenomena* **2002**, *122*, 57–63.
(75) Sankari, R.; Ehara, M.; Nakatsuji, H.; Senba, Y.; Hosokawa, K.; Yoshida, H.; De Fanis, A.; Tamenori, Y.; Aksela, S.; Ueda, K. Vibrationally Resolved O 1s Photoelectron Spectrum of Water. *Chemical Physics Letters* **2003**, *380* (5), 647–653. https://doi.org/10.1016/j.cplett.2003.08.108.
(76) *The Gaussian-Lorentzian Sum, Product, and Convolution (Voigt) functions in the context of peak fitting X-ray photoelectron spectroscopy (XPS) narrow scans | Elsevier Enhanced Reader*. https://reader.elsevier.com/reader/sd/pii/S0169433218308766?token=D6603FC41594F943A93A57135FA027C505E5D99677AF586C6C8CB74F00D85FA8247461972CD35CA6A8F52AB61701AE49&originRegion=eu-west-1&originCreation=20220531111459 (accessed 2022-05-31). https://doi.org/10.1016/j.apsusc.2018.03.190.
(77) Nicolafrancesco, C; Hartweg, S; Gil, JF; Robert, E; Ramillon, JM; Nicolas, C; Indrajith, S; Bozek, J; Nahon, L; Milosavljevic, AR; Rousseau, P; A cluster source for photoelectron spectroscopy in VUV and X-ray ranges. Eur. Phys. J. D **2021**, *75* (4), 117; https://doi.org/10.1140/epjd/s10053-021-00124-5

ANALYSIS OF THE IONS AND ELECTRONS EMITTED BY HYPOXANTHINE IN THE GAS PHASE UPON IRRADIATION: FROM THE ISOLATED MOLECULE TO HYDRATED CLUSTERS

ENGLISH ABSTRACT

This work is part of the studies aimed at understanding how biomolecules interact with their molecular environment and how this environment influences their physical and chemical properties. In this work, the object of study is the hypoxanthine molecule, a purine derivative. This molecule is studied in the gas phase, under three aggregation states: isolated molecule, pure clusters, and hydrated clusters. Molecular fragmentation induced by ion and VUV photon impact is investigated by means of mass spectrometry. K-shell ionization is analyzed by means of X-ray photoelectron spectroscopy. The results provide information on the stability of the hypoxanthine molecule upon irradiation and on how non-covalent bonds can affect its physical and chemical properties.

ANALYSE DES IONS ET DES ÉLECTRONS ÉMIS PAR L'HYPOXANTHINE EN PHASE GAZEUSE APRÈS IRRADIATION : DE LA MOLÉCULE ISOLÉE JUSQU'AUX AGRÉGATS HYDRATÉS

RÉSUMÉ EN FRANÇAIS

Ce travail s'inscrit dans le cadre des études visant à comprendre comment les biomolécules interagissent avec leur environnement moléculaire et comment cet environnement influence leurs propriétés physiques et chimiques. Dans ce travail, l'objet d'étude est la molécule d'hypoxanthine, un dérivé de la purine. Cette molécule est étudiée en phase gazeuse, sous trois états d'agrégation : molécule isolée, agrégats purs et agrégats hydratés. La fragmentation moléculaire induite par impact d'ions et de photons VUV est analysée par spectrométrie de masse. L'ionisation en couche K est analysée par spectrométrie photoélectronique X. Les présents résultats fournissent des informations sur la stabilité de la molécule d'hypoxanthine sous irradiation et sur l'influence de liaisons non covalentes sur ses propriétés physiques et chimiques.

Keywords: hypoxanthine, biomolecules, purines, mass spectrometry, XPS, molecular clusters, hydrated clusters, gas phase, synchrotron, photo-absorption, photoemission, ion impact